INFORMATION TO USERS

This manuscript has been reproduced from the microfilm master. UMI films the text directly from the original or copy submitted. Thus, some thesis and dissertation copies are in typewriter face, while others may be from any type of computer printer.

The quality of this reproduction is dependent upon the quality of the copy submitted. Broken or indistinct print, colored or poor quality illustrations and photographs, print bleedthrough, substandard margins, and improper alignment can adversely affect reproduction.

In the unlikely event that the author did not send UMI a complete manuscript and there are missing pages, these will be noted. Also, if unauthorized copyright material had to be removed, a note will indicate the deletion.

Oversize materials (e.g., maps, drawings, charts) are reproduced by sectioning the original, beginning at the upper left-hand corner and continuing from left to right in equal sections with small overlaps.

Photographs included in the original manuscript have been reproduced xerographically in this copy. Higher quality 6" x 9" black and white photographic prints are available for any photographs or illustrations appearing in this copy for an additional charge. Contact UMI directly to order.

Bell & Howell Information and Learning
300 North Zeeb Road, Ann Arbor, MI 48106-1346 USA
800-521-0600

UMI®

UNIVERSITÉ DE MONTRÉAL

GROWTH, CHARACTERIZATION AND DESIGN OF INP-BASED STRAINED-LAYER MULTIPLE QUANTUM WELLS FOR OPTICAL MODULATOR DEVICES

RAYMOND YEW-FAI YIP

DÉPARTEMENT DE GÉNIE PHYSIQUE

ÉCOLE POLYTECHNIQUE DE MONTRÉAL

THÈSE PRÉSENTÉE EN VUE DE L'OBTENTION

DU DIPLÔME DE PHILOSOPHIAE DOCTOR (PH.D.)

(GÉNIE PHYSIQUE)

SEPTEMBRE 1997

© Raymond Yew-Fai Yip, 1997.

National Library of Canada

Bibliothèque nationale du Canada

Acquisitions and Bibliographic Services

Acquisitions et services bibliographiques

395 Wellington Street
Ottawa ON K1A 0N4
Canada

395, rue Wellington
Ottawa ON K1A 0N4
Canada

Your file Votre référence

Our file Notre référence

The author has granted a non-exclusive licence allowing the National Library of Canada to reproduce, loan, distribute or sell copies of this thesis in microform, paper or electronic formats.

L'auteur a accordé une licence non exclusive permettant à la Bibliothèque nationale du Canada de reproduire, prêter, distribuer ou vendre des copies de cette thèse sous la forme de microfiche/film, de reproduction sur papier ou sur format électronique.

The author retains ownership of the copyright in this thesis. Neither the thesis nor substantial extracts from it may be printed or otherwise reproduced without the author's permission.

L'auteur conserve la propriété du droit d'auteur qui protège cette thèse. Ni la thèse ni des extraits substantiels de celle-ci ne doivent être imprimés ou autrement reproduits sans son autorisation.

0-612-46642-6

Canada

UNIVERSITÉ DE MONTRÉAL

ÉCOLE POLYTECHNIQUE DE MONTRÉAL

Cette thèse intitulée:

GROWTH, CHARACTERIZATION AND DESIGN OF INP-BASED STRAINED-LAYER MULTIPLE QUANTUM WELLS FOR OPTICAL MODULATOR DEVICES

présentée par: YIP, Raymond Yew-Fai

en vue de l'obtention du diplôme de : Philosophiae Doctor

a été soumise au jury d'examen constitué de:

M. ROORDA, Sjoerd, Ph.D., président du jury

M. MASUT, Remo Antonio, Ph.D., directeur de recherche

M. CURRIE, John F., Ph.D., co-directeur de recherche

M. LEONELLI, Richard, Ph.D., membre

M. CHARBONNEAU, Sylvain, Ph.D., membre

ABSTRACT

Optical modulators based on the quantum-confined Stark effect (QCSE) were fabricated from strained InAsP/InP and strain-compensated InAsP/InGaP epitaxial layers grown by metal-organic vapor phase epitaxy. An accurate measurement of the well width, barrier width, state of strain and ternary alloy compositions was performed using a combination of high-resolution x-ray diffraction rocking curves and transmission electron microscopy. The series contained samples with both coherently strained, and partially relaxed multi-layers. Strain relaxation in the InAsP/InP series occurred exclusively via misfit dislocations localized to the outer interfaces of the multiple quantum well stack (MQWS). Strain relaxation in the InAsP/InGaP series occurred primarily via strain-induced growth instabilities, as reported by P. Desjardins *et al.* [J. Appl. Phys. **81**, 3501 (1997)]. The heterojunction band discontinuities were determined by fitting the energy positions of the optical absorption peaks, measured at low and room temperature, with those computed using the Marzin-Bastard band structure model for strained-layer superlattices. Consistent with the results of M. Beaudoin *et al.* [Phys. Rev. B **53,** 1990 (1996)], the conduction band discontinuities were found to be linear in the As composition for the InAsP/InP samples (7.56 ± 0.08 meV per As % in the InAsP layer).

The electric field-dependent redshift of the n = 1 electron-heavy hole transition was measured by a photocurrent method and observed to be significantly enhanced in

structures with lower valence band barrier heights. This led to a more general observation that strategies designed to optimize the performance of the MQWS in QCSE devices can be derived from the fact that the effective mass of the active quantum well material in III-V semiconductors is significantly smaller in the conduction band than that in the valence band. A detailed analysis and discussion of the device physics for the QCSE based upon barrier height and band alignment considerations was conducted. It concluded the following two key principles for designing the band structure of the MQWS.

1. A counterbalance relationship between maximum optical modulation depth and minimum drive field is implicit in the mechanics of the QCSE As a result of this trade-off, it is not possible to optimize one independently of the other.
2. A strong asymmetry in the field response of the conduction and valence band eigenstates is due directly to the asymmetry of the conduction and valence band effective masses. Because of this, the maximum optical modulation depth per unit applied electric field is obtained by designing the multi-quantum well stack with a disproportionately large conduction band offset to match the effective mass asymmetry and balance the field-induced wave function leakage at the conduction band to that at the valence band.

The relative wave function leakage between conduction and valence bands was examined by comparing their respective tunnel currents through the quantum well barriers as a function of electric field and barrier height. When the conduction and valence band effective masses are respectively $0.055m_0$ and $0.5m_0$, we found that a balanced, optimal design requires a conduction band discontinuity 3-9 times larger than the valence band discontinuity. Applying the design principles to high-speed, low drive voltage optical modulators concludes that the overall performance may be improved by using designs that incorporate a combination of balanced band alignments and valence band barriers lower than 60 - 100 meV. Low valence band barriers reduce the drive field required to operate the devices, which can improve the overall performance by permitting a lower drive voltage and/or wider diode junction with larger active volume, lower capacitance, lower propagation losses and improved optical coupling. The systems of strain-compensated InAsP/InGaAsP and nearly lattice-matched InGaAs/InAlGaAs grown on InP(001) are identified as two promising candidates for optimal heterostructures operating in the 1.3-1.55 μm range for optical telecommunications.

A simple model was developed to conduct a brief investigation and review of theoretical and experimental results in the literature on the use of quantum wells to enhance the detailed balance efficiency limit for solar energy conversion. We conclude that practical efficiency enhancements, if they exist, are very small.

CONDENSÉ EN FRANÇAIS

Les progrès accomplis durant les dernières décennies dans le domaine de la science et de la technologie des couches minces semiconductrices ont fortement contribué à promouvoir la révolution actuelle qui se déroule dans le domaine des technologies de l'information et des télécommunications ultra-rapides à longue distance. Les nouveaux développements dans cette branche d'activité sont à suivre de près pour l'influence qu'ils risquent d'exercer sur l'avenir à l'échelle mondiale.

La majorité des activités dans le domaine des semiconducteurs est concentrée sur le silicium, matériau qui combine une fabuleuse manufacturabilité et un faible coût. Mais le silicium est pour l'instant inapproprié pour des applications d'électronique ultra-rapide ou d'optoélectronique. D'autre part, les semi-conducteurs composés III-V possèdent des propriétés intrinsèques (haute mobilité, gap direct, possibilité de faire varier la largeur du gap en changeant la composition de l'alliage, etc.) qui conviennent parfaitement à de telles applications; toutefois, de sérieux problèmes technologiques associés à ces matériaux ralentissent la fabrication et la commercialisation à grande échelle de dispositifs complexes qui les utilisent. Cependant, dans certains secteurs où il n'existe pas de matériaux de remplacement, comme celui des télécommunications par fibre optique, et pour les applications militaires ou spatiales, d'importantes avancées technologiques ont permis la commercialisation de dispositifs à base de matériaux III-V.

Dans ce contexte, je présente une étude sur les principales étapes de conception et de fabrication d'un dispositif basé sur des matériaux III-V. Il s'agit d'un modulateur optique à électro-absorption qui fonctionne sur le principe de l'effet Stark à confinement quantique (ESCQ). Il est constitué d'une région active non intentionnellement dopée, formée par des multi-puits quantiques (MPQ) d'InAsP/InP ou d'InAsP/InGaP, prise en sandwich entre une couche d'InP de type p et une autre de type n (diode p-i-n). Les étapes de fabrication de ce dispositif optoélectronique sont les suivantes:

a) la croissance des multi-couches contraintes par épitaxie en phase vapeur aux organométalliques,
b) la caractérisation structurale et optique de ces multi-couches,
c) la fabrication de photodiodes p-i-n,
d) la caractérisation électrique et électro-optique des photodiodes, et
e) l'analyse des performances des photodiodes en fonction de la structure des couches et l'optimisation des prochains dispositifs à fabriquer via l'ingéniérie des alignements de bandes.

Le spectre d'absorption optique aux abords de la bande interdite d'une structure à MPQ diffère de celui du matériau en volume. De plus, ce spectre peut être modifié considérablement par l'application d'un champ électrique externe. En effet, le potentiel

de confinement d'un puit quantique permet la formation stable, à la température ambiante, de systèmes constitués d'un électron et d'un trou faiblement liés par la force d'attraction coulombienne, appelés excitons. Ces systèmes excitoniques ont un comportement similaire à celui de l'atome d'hydrogène mais avec une énergie de liaison beaucoup plus faible (de l'ordre de 5 à 10 meV). Leur présence ajoute des résonances quasi-atomiques ayant des forces d'oscillateur importantes dans le spectre d'absorption optique du matériau, à des énergies voisines, mais légèrement inférieures à celle du gap du puit quantique. L'application d'un champ électrique dans la direction normale au puit quantique produit simultanément les deux effets suivants:

1. Les niveaux d'énergie du puit dans la bande de conduction (BC) et la bande de valence (BV) se déplacent vers le rouge, avec pour conséquence un déplacement de l'énergie fondamentale de la transition optique vers le rouge;
2. Les états propres dans les deux bandes se polarisent, ce qui a pour conséquence d'élargir et finalement de faire disparaître la résonnance d'absorption (étalement, puis exctinction du pic excitonique).

Toutefois, le potentiel de confinement du puit quantique a tendance à retarder l'extinction de la résonnance et permet d'observer un déplacement appréciable de l'énergie de transition avant que l'élargissement du pic excitonique ne devienne trop important. Ce mécanisme donne la possibilité d'induire d'importants changements dans

l'absorption optique (profondeur de modulation) du matériau à l'aide d'un champ électrique. Il est appelé effet Stark à confinement quantique. Ainsi, lorsqu'on insère des MPQ dans la zone intrinsèque d'une diode p-i-n, celle-ci constitue, une fois polarisée en inverse, un modulateur optique très efficace dont la modulation est facilement controlée par la tension appliquée à ses bornes. En polarisation inverse, la diode se comporte du point de vue électrique comme un simple condensateur dont la capacité dépend des dimensions linéaires. En principe, les dimensions du modulateur peuvent être choisies de telle façon que la limite supérieure de modulation puisse atteindre des fréquences dans la gamme du térahertz. De plus, la fabrication de ces modulateurs est technologiquement compatible avec celle des lasers à semiconducteurs qui émettent dans l'infra-rouge. Ainsi, l'intégration monolithique de modulateurs à ESCQ avec des lasers à semiconducteurs produirait un dispositif dont les performances seraient à l'avant-garde en terme de systèmes ultra-rapides de télécommunication à longue distance.

La partie expérimentale de cette thèse comprend la fabrication et la caractérisation de deux séries de modulateurs optiques basés sur des multi-couches contraintes d'InAsP/InP et d'InAsP/InGaP. La croissance épitaxiale de ces couches présente plusieurs défis technologiques, dont celui du contrôle de la relaxation de la contrainte élastique entre les couches déposées et le substrat. La caractérisation de ces multi-couches a été réalisée à l'aide de plusieurs techniques complémentaires les unes des autres, dont: la diffraction des rayons X à haute résolution, la microscopie

électronique en transmission et les mesures d'absorption optique et de photoluminescence. Ces caractérisations structurales et optiques ont permis de déterminer les épaisseurs, les compositions et l'état de relaxation des différentes couches ainsi que le schéma d'alignement des bandes d'énergie entre les différents matériaux qui constituent ces hétérostructures.

La fabrication des photodiodes p-i(MPQ)-n a débuté avec la définition de structures 'mésas' pour l'isolation électrique. On a tout d'abord utilisé la photolithographie avec le masque en contact avec l'échantillon pour définir les motifs, puis a suivi une gravure chimique à travers les couches épitaxiales jusqu'au substrat, à l'aide des solutions d'attaque $HCl:CH_3COOH:H_2O_2$ ou $HCl:H_3PO_4:H_2O_2$. Nous avons obtenu un taux de gravure adéquat et une bonne morphologie de l'InP, de l'InAsP et de l'InGaP après gravure. Toutefois, on a eu à faire face à des problèmes reliés au contrôle du taux de gravure, à la sur-gravure dans les directions latérales en-dessous des bords du masque et à la reproductibilité. Ces problèmes peuvent être attribués directement à la réaction exothermique entre l'acide chlorhydrique et le peroxyde d'hydrogène, une réaction qui contribue à élever la température de la solution et à produire une accumulation de chlore gazeux en solution. On a aussi observé que la qualité du peroxyde d'hydrogène avait un effet prononcé sur la reproductibilité du taux de gravure. Ce type de gravure étant anisotrope, on a dû prendre soin de bien aligner les bords du masque suivant l'une des directions cristallographiques afin d'obtenir les motifs

recherchés. Après avoir défini les structures 'mésas', on a réalisé les contacts électriques vers les couches d'InP en métallisant à l'aide des alliages Au-12%wt.Ge-5%wt.Ni (sur le type n) et Au-10%wt.Zn (sur le type p). Les motifs pour les contacts électriques ont d'abord été transférés sur les échantillons grâce à la technique dite de "lift-off", ou les alliages étaient déposés par évaporation thermique. Après la déposition, les échantillons ont subi des recuits thermiques rapides (RTR) dans le but d'améliorer l'ohmicité et la résistance des contacts. D'excellents contacts ohmiques ont été produits avec des couches de 100 à 300 nm d'Au-12%wt.Ge et Au-12%wt.Ge-5%wt.Ni sur l'InP de type n. Ces contacts étaient en général ohmiques avant même le traitement par RTR. Les meilleurs contacts sur l'InP de type p ont plutôt été fabriqués à l'aide d'une déposition en séquence de 5 nm Au/ 20 nm Zn / 100 à 300 nm Au, ceci étant suivi par de courts traitements par RTR. Ils ont exhibité un comportement hybride, à mi-chemin entre le contact ohmique pur et le contact Schottky additionné de courants de fuite en polarisation inverse. Ils avaient en moyenne des résistances de deux ordres de grandeur plus elevées que celles des contacts sur n-InP. On a conclu que la pénétration rapide et en profondeur des métaux dans les couches épitaxiales donnait comme résultat un mélange des composés métalliques et semiconducteurs qui nuisait à la reproductibilité des contacts. Cependant, de courts traitements par RTR à faible température ont produit des résultats suffisamment satisfaisants sur ces contacts pour nous permettre de poursuivre.

On a alors effectué sur ces photodiodes des mesures d'absorption optique en fonction du champ électrique par la technique de détection du courant de photo-absorption. On a noté une diminution du champ d'opération pour les modulateurs dont la discontinuité à la BV est faible. Ce qui a mis en évidence le rôle primordial que joue l'alignement des bandes dans l'optimisation des performances des hétérostructures à MPQ basé sur l'ESCQ.

On a remarqué que, pour tout dispositif fonctionnant sur le principe de l'ESCQ, un compromis doit être fait entre le déplacement en énergie et la polarisation des états propres du puit quantique induite par le champ électrique. L'absorption optique aux abords de la bande interdite est déterminée par l'effet du champ électrique sur les niveaux fondamentaux dans la BC et la BV. Les niveaux plus proches du fond du puit suivent plus étroitement les contours du puit déformés par le champ. Ils sont donc plus sensibles au champ électrique. Dans le cas général où les matériaux sont des alliages de composés III-V, le niveau fondamental de la BV est nettement plus près du fond du puit que celui de la BC puisque la masse effective des trous est bien supérieure à celle des électrons. La composante de la BV apporte alors la contribution dominante au déplacement total de l'énergie de la transition optique. L'extinction de la résonnance excitonique peut être modélisée par la délocalisation des fonctions d'ondes due à la transmission par effet tunnel (TET) à travers les barrières. La TET est fonction de la pénétration des fonctions d'onde de la BC et la BV dans les barrières, où de façon

équivalente, des grandeurs de leurs vecteurs d'onde respectifs dans les barrières. La fonction d'onde de le BC a tendance à se délocaliser avant celle de la BV à cause de la plus faible masse effective des électrons. Ainsi, la résistance à l'extinction de l'exciton par le champ est en général limitée par la composante de la BC. Une telle configuration est toujours sous-optimale parce que la hauteur de la barrière dans la BV est plus élevée que nécessaire alors que la hauteur de la barrière dans la BC est moins élevée que nécessaire. Il est toujours possible de concevoir une structure qui conservera l'énergie de la principale transition optique avec une barrière dans la BV moins élevée pour augmenter le déplacement vers le rouge induit par le champ, et une barrière dans la BC plus élevée pour améliorer la résistance à l'extinction de l'exciton. Cette structure conduira à un dispositif qui possède une profondeur de modulation plus grande et qui exige un champ moins élevé pour l'induire.

A partir du raisonnement présenté dans le paragraphe précédent, nous proposons d'utiliser l'ingénierie des alignements de bandes pour contrebalancer l'asymétrie des masses effectives en utilisant un alignement de bande asymétrique avec une forte discontinuité à la BC. De l'analyse de la physique de l'ESCQ sortent deux principes de conception des structures à MPQ basées sur cet effet.

1. Un compromis entre la profondeur de modulation et le champ électrique nécessaire pour faire fonctionner le dispositif (champ d'opération) est implicite dans le principe

physique de l'ESCQ. Ceci est dû au fait que les états propres du puit quantique doivent suivre la rampe en énergie, induite par le champ, dans des directions opposées. De plus, à un important déplacement en énergie doit correspondre une importante polarisation. Le contraire s'applique aussi. Cette observation met en lumière l'impossibilité d'optimiser la profondeur de modulation et le champ d'opération en même temps. Une stratégie d'optimisation doit trouver le compromis optimal entre les deux effets. ce qui dépend des exigences technologiques propres à chaque application particulière.

2. L'asymétrie entre les états propres à la BC et à la BV dans leur réponse à l'application du champ électrique est une conséquence directe de l'asymétrie entre les masses effectives des porteurs dans les deux bandes. L'alignement de bandes qui égale la délocalisation de la fonction d'onde dans la BC avec celle dans la BV donne la force d'oscillateur maximale pour la transition excitonique et cependant elle maximise aussi le changement dans le coefficient d'absorption par l'application du champ électrique.

L'application de ces deux principes de base à la conception d'hétérostructures pour la fabrication de modulateurs optiques fonctionnant à très haute vitesse et à faible champ d'opération nous conduit à la conclusion que les structures optimales devraient comprendre une faible discontinuité à la BV (moins que 60-100 meV) et une discontinuité à la BC 3-9 fois plus élevée que celle à la BV. La faible discontinuité à la

BV apportera une réduction du champ d'opération, gain qu'on pourrait mettre à profit pour abaisser la tension d'opération ou la capacité de la diode ou augmenter le coefficient d'atténuation du dispositif ou minimiser les pertes dues au guidage et au couplage de l'onde optique, ceci dépendamment des exigences technologiques particulières liées au type d'application envisagée. Les structures idéales devraient être réalisables à l'aide des alliages à base de (Al, Ga, In, P, As) sur substrat d'InP(001). Ces analyses et conclusions sont bien corroborées par les données expérimentales obtenues à partir des deux séries de modulateurs optiques fabriqués au cours de cette thèse.

En addition, nous avons développé un simple modèle afin d'étudier la possibilité d'améliorer l'efficacité de la conversion d'énergie solaire dans la limite radiative avec l'addition des MPQs dans la jonction des cellules solaires à simple énergie de bande interdite. Avec l'aide du modèle, nous concluons que les améliorations potentielles sont très faibles.

ACKNOWLEDGEMENTS

The future is always difficult to gauge, especially now. But I believe that I will eventually remembered this period as "that time after undergrad where I did a lot of work, earned very little and probably learned a few things." Then, it begins immediately after graduating from UBC with an 8 month stay at the INMS department of NRC in Ottawa where Alan Madej, Brad Whitford, Klaus Hohlfeld, John Sankey and Bill Cazameir taught me about optics, lasers and electronics, and let me use all those hazardous machine tools. Back at UBC, Tom Tiedje and Dave Pulfrey have always willingly offered their advice and aid. I feel rather disappointed not to have been able to work with them during these last four years. Through Tom Tiedje, I met John Currie, who by doing odd things like faxing me his CV, promptly managed to sway me into thinking that a quick M.A.Sc. plus a look at life in Montréal would be preferrable to the cornfields of West Lafayette or the swamps around Gainesville and Orlando. We spoke for the second time in mid January 1993 when I said that I would arrive in two weeks to start work. Upon arriving at Polytechnique in February 1993 after flying to a frozen Ottawa from a comparatively balmy Vancouver and driving down to an equally frozen Montréal in a car without heat, it was a bit of a shock to realize that they were not expecting me. This was when I met Remo Masut, who was kind enough to greet me while John was still busy in the lab. So, the Montréal phase was duly christened.

In the first year to year and a half, I split my time between LISA and MODFAB. Although my research activities eventually diverged completely from his, I am very grateful to my co-director, Professor John Currie, for welcoming me to Polytechnique and Montréal, and encouraging me to work freely within both the LISA and MODFAB laboratories during this important period of initiation. His energy and constant desire to find new ways to do work have been highly inspirational. At LISA and MODFAB, I met and had many pleasant exchanges with various members of the technical staff: Edwis Richard, André Lecours, Jacques Lajoie, Gino Turcotte, Robert Antaki, Mario Caron, Sundaraman Chetlur, Normand Gravel, Joel Bouchard and Dentcho Ivanov. I was welcomed and given the opportunity to work in the optical characterization laboratory of the Department of Physics at the University of Montréal by Professor John Brebner. There, I met Abderrahmane Aït-Ouali who eventually performed most of the optical characterizations on the modulator samples. We also worked together to develop the photocurrent measurement. After committing to a Ph.D., I quickly began to spend more time in the MOCVD lab. This trend continued so that in the last year and a half, I have worked almost exclusively there. I am deeply indebted to the current and former members of the MOCVD group for their ready offer of aid and advice, and for the efforts that they have made on my behalf. Pat Desjardins was a marvelous resource and a great example. Laurent Isnard has been a steady and reassuring presence. Ahmed Bensaada and Mario Beaudoin provided me with some much needed epitaxial layers and important advice about InP. In addition, I have also learned much about growth and

characterization from working and conversing with Stephane Guillon, Zahia Bougrioua, Hugues Marchand and Jacques-Edmond Paultre. I owe very a substantial thank you to my director, Professor Remo Masut. I admire his commitment to teaching and greatly appreciate that he has always been available for extended discussions. I have benefited enormously from these.

I dedicate this to my parents who have tirelessly encouraged and supported my efforts despite a near complete unfamiliarity with what I was doing.

TABLE OF CONTENTS

ABSTRACT iv

CONDENSÉ EN FRANÇAIS vii

ACKNOWLEDGEMENTS xvii

LIST OF TABLES xxii

LIST OF FIGURES xxv

LIST OF APPENDICES xxxii

SYMBOLS AND ABBREVIATIONS xxxiii

1 INTRODUCTION 1

2 EXPERIMENTAL METHODS AND BACKGROUND 7

2.1 *Sample cleaning* 7

2.2 *Growth of strained-layer, InP-based thin film materials by MOVPE.* 8

2.3 *Structural characterization by x-ray diffraction* 17

2.4 *Wet chemical etching of InP in HCl-based solutions* 23

2.5 *Au-based contact metallizations on InP* 28

2.6 *Measurement of field-dependent absorption curves by photocurrent detection* 37

2.7 *Additional remarks* 39

3 DETAILED BALANCE EFFICIENCY LIMIT IN QUANTUM WELL SOLAR CELLS 40

4 STRAIN AND RELAXATION IN MULTIPLE QUANTUM WELL STACKS 55

5 BAND ALIGNMENT ENGINEERING FOR THE QUANTUM-CONFINED STARK EFFECT 93

5.1 *Band alignment engineering for high-speed, low drive field quantum-confined Stark effect devices* 95

5.2 *Additional Remarks* 139

6 CONCLUSIONS 140

7 REFERENCES 143

8 BIBLIOGRAPHY 156

APPENDIX 169

LIST OF TABLES

Table 4-I Sample listing and structural parameters obtained from high-resolution (115+/115-) and (004) XRD scans. Using mismatches measured with respect to InP, the fully relaxed, free-standing lattice parameter of the InAsP quantum well sections was deduced from a knowledge of the lattice parameters for the strain-distorted unit cell. This was subsequently used to compute the As composition of the wells, biaxial well strain and relaxation (R). h/hc is the ratio of the multi-layer structure thickness to the Matthews—Blakeslee critical limit for a layer of the average composition. 62

Table 4-II Parameters used in the effective well width calculation. The barrier heights and E1 energies were obtained from the Marzin—Bastard envelope function calculation of the quantum well energies. E1 is the energy of the first quantized level with respect to the bottom of the well. The effective masses in the direction of the electric field are not significantly affected by strain so the values listed are linear interpolations between InAs and InP. The effective well widths are "equivalent" infinite well widths chosen such that the zero-field E1 energies match. $\Delta\alpha$ is the measured field-induced absorption coefficient change in each structure and the voltage at which it is attained. 79

Table 5-I Sample listing. The layer thicknesses and compositions are determined from a combination of x-ray diffraction, transmission electron microscopy and optical absorption measurements. The barrier heights and E_l levels are obtained by fitting quantum well transitions calculated using the Marzin—Bastard model for strained-layer superlattices to transitions measured by optical absorption at 8 K and 300 K. e1, hh1 and lh1 refer respectively to the n=1 levels in the conduction, heavy hole and light hole bands. The effective masses in the direction of the quantum confinement potential are linear interpolations between InAs and InP, given in units of the electron mass, m_0. 117

Table 5-II. Comparison of the multi-quantum well stacks studied in this paper using two common figures of merit for optical modulators. The samples are listed from top down in order of increasing total barrier height. $\Delta\alpha$ is the change in absorption coefficient available at an applied electric field, F. The $\Delta\alpha$ values are measured in the region of low on-state loss (low energy tail of the exciton resonance) for which $\alpha_0 < 500$ cm^{-1}. t is the total thickness of quantum well material available for electroabsorption. This demonstrates the trade-off between modulation depth and drive field as a function of barrier height. 123

Table 5-III. Variation of the quantum well transition energies of sample mod06 computed using the Marzin—Bastard model with changes in the band alignment. e1-hh1 and e1-lh1 refer respectively to the optical transitions between the n=1 conduction-heavy hole and conduction-light hole levels. ΔE_C, ΔE_V and ΔE_g are respectively the conduction band discontinuity, valence band discontinuity and total energy band gap difference between quantum well and barrier. E_1 refers to the n = 1 quantum well energy levels. As the partition of the band gap energy difference between CB and VB changes, the e1-hh1 transition remains nearly constant while the e1-lh1 shifts. This shows that in the InAsP/InP system, the difference between the heavy and light hole transitions can be a sensitive key for determining the band alignment........................ 137

LIST OF FIGURES

Figure 2.1 Critical thickness for the formation of misfit dislocation calculated using the Matthews—Blakeslee force balance model (see Ref. 15). 11

Figure 2.2 Double quantum well InAsP/InP test structure used to measure and calibrate growth parameters. The gas flow sequence for the structure is indicated on the right. Manifold duration is measured in seconds. [In], [As] and [P] refer to the flow of precursor species. By careful choice of the thicknesses of the InAsP quantum well, InP spacer and InP cap layers, it is possible to deduce the growth rate of the InAsP and InP, and the As incorporation from a single XRD rocking curve that may be acquired in 15 - 30 minutes. 20

Figure 2.3 XRD (004) rocking curve (upper) and simulation curve (lower) for the sample in Figure 2.2. The data acquisition time for this curve was 15 minutes. 21

Figure 2.4 InAsP/InP multiple quantum well sample after etching in a solution of $HCl:CH_3COOH:H_2O_2$ (viewed with an optical microscope using Nomarski contrast). The etched depth is 0.63 μm. The striations in the etched surface (top left) are due the the effects of the layer strain and the presence of misfit dislocations. Significant lateral advance of the etch front underneath the photoresist etch mask is clearly visible (top right, bottom left and right). The width of the photoresist neck in the top right photograph is 40 μm. The separation of the photoresist corners in the bottom photographs is 20 μm..................... 24

Figure 2.5 SEM micrograph of a lift-off photoresist profile on Si substrate. The thermal evaporation of a metal film onto the re-entrant photoresist profile facilitates the formation of a clean discontinuity in the metal film. A subsequent dip in a photoresist stripper, or solvent such as acetone, removes the unwanted metal and transfers the photomask pattern to the sample. 29

Figure 2.6 A 5 nm Au/ 200 nm Au-10%wt. Zn film on Zn-doped InP after a short anneal of 2 s at 300 °C (viewed with an optical microscope using Nomarski contrast). Before annealing, the metal film was uniform sheet of Au. The changes in the color and morphology of the metal sandwich layer indicate that significant microstructural changes have occured 32

Figure 2.7 A 200 nm Au-10%wt. Ge-5%wt. Ni film on S-doped InP after a short anneal of 2 s at 430 °C. Before annealing, the metal film was uniform sheet of Au. The color and morphology of the metal sandwich layer show that a very significant interaction between metal and InP has occurred. 33

Figure 2.8 Experimental set-up for measurement of the electric field-dependent changes of the optical absorption in the p-i(MQW)-n photodiodes. 38

Figure 3.1 Detailed balance efficiency limit for a single bandgap p-n junction photovoltaic cell in equilibrium with a surrounding black-body radiation field at 300 K and receiving incident radiation from a 5850 K solar spectrum. These conditions are equivalent to air mass zero (AM0). 44

Figure 3.2 Schematic relationship between the main elements required to model the behavior of a quantum well solar cell. The cell with quantum wells can be considered a superposition of a single bandgap cell coupled to a system of quantum wells. $Q'(E_{qw}, T_s)$ and $Q'(E_{qw}, T_c)$ represent the respective contributions of the quantum wells to the generation and recombination rates in the cell. t_{qw} and r_{qw} are constants that describe the degree of coupling between the single band gap cell and the quantum wells. 47

Figure 3.3 Calculated detailed balance efficiency limit as a function of energy bandgap for a) a single bandgap p-n solar cell and for b), c), d) solar cells with 500 meV deep quantum wells. t_{qw} and r_{qw} are coupling constants used to model the nature of photocharge transfer between quantum well and barrier. 50

Figure 4.1 Nominal layer and device structure for p-i(multi-quantum-well)-n optical modulators. 61

Figure 4.2 Symmetric (004) reflection high-resolution x-ray diffraction rocking curves. The arrows indicate the approximate positions of separate peaks due to tensilely-strained InP material in the samples where plastic relaxation has been detected (see Table 4-I.). 65

Figure 4.3 Transmission electron microscopy bright-field images of mod04: (a) g = (002), and (b) g = $(2\bar{2}0)$. 68

Figure 4.4 Absolute optical absorption spectra for the as-grown epitaxial layers listed in Table I at a) T = 8 K and b) T = 295 K. The n = 1 electron-heavy hole (e1-hh1) and electron-light hole (e1-lh1) transitions are identified with arrows. The full width half maxima (FWHM) at T = 8 K and at T = 295 K for the e1-hh1 transitions are summarized in the inset tables. 71

Figure 4.5 Dependence of the absolute conduction band discontinuity, δE_C (meV), on the As composition, x, of the $InAs_xP_{1-x}$ quantum wells. The data points corresponding to samples in the current study are identified with arrows. The other points correspond to samples in Refs. 20 and 21. The linear least squares fit of the all the data points gives a slope of 7.56 ± 0.08 meV/As%. 74

Figure 4.6 Dependence of the n = 1 electron-heavy hole (e1-hh1) and electron-light hole (e1-lh1) transition energy difference, as measured by optical absorption (Figure 4.4), on the compressive biaxial strain in the InAsP quantum wells, as measured by x-ray diffraction (Table 4-I). The inset diagram (top left) illustrates the modification of the quantum well band gap due to compressive strain. 75

Figure 4.7 Spectral photocurrent response of p-i(multi-quantum-well)-n diodes as a function of reverse-bias voltage at T = 295 K for a) mod05 (10.0% As), b) mod06 (15.6% As), c) mod04 (26.4% As) and at T = 11 K for d) mod02 (13.5% As). The nominal intrinsic layer thickness is 0.6 μm in a), b), c) and 1.9 μm in d). 78

Figure 4.8 The field-dependent energy red-shift of the quantum well levels for mod05 (10.0% As), mod06 (15.6% As) and mod04 (26.4% As) determined from the photocurrent curves (Figure 4.7). The shift as approximated by the effective well width method using the parameters in is included for comparison 80

Figure 4.9 The effective well width approximation. 89

Figure 4.10 The effect of variations in the finite barrier height on the QCSE calculated using the effective well width approximation for a typical InAsP/InP quantum well in the presence of a 50 kV/cm electric field. 91

Figure 5.1 Variation of the field-induced shift, ΔE_l, of the n = 1 conduction and valence band quantum well energy levels with barrier height. Useful enhancements to the redshift per unit field may be achieved by using valence band barriers lower than 60 - 100 meV. The redshift has been calculated for electrons and heavy holes in a 10 nm wide quantum well with an applied field of 50 kV/cm using the effective well width method (see Ref. 1, EWW curves) and the variational model (see Ref. 13, VAR curves). The values for the effective masses are representative of conduction and valence band effective masses for InGaAsP alloys with $E_g \sim 0.8$ - 1.35 eV. m_0 is the electron mass. 104

Figure 5.2 Band alignments at flat band are shown for a typical structure (left) and a balanced structure (right). 108

Figure 5.3 Conditions at the edge of the quantum well for a) flat band, b) moderate field and c) high field. T_{rect}, T_{trap}, and T_{tri} are the approximate analytical expressions for the probability tunneling currents obtained using the method of Wentzel, Kramers and Brillouin. See Ref. 20 for details............................ 110

Figure 5.4 The ratio of CB to VB barrier heights giving equivalent probability tunneling currents (quench) as a function of the electric field. The curves have been obtained by writing the expressions (see Ref. 19 for details) describing the tunnel currents under the conditions illustrated in Figure 5.5 and then iteratively solving for the band alignments to give equivalent currents at the CB and VB. The dotted lines indicate approximately where the wave functions have become delocalized from the well based on the magnitude of the tunnel currents. These curves permit a estimate of the minimum barrier height required at the CB for a given barrier height at the VB in an optimal MQWS. 113

Figure 5.5. Field-dependent absorption spectra measured by photocurrent detection for: a) 25 × (9.8 nm $InAs_{0.100}P_{0.900}$ / 9.8 nm InP) (mod05), b) 25 × (10.3 nm $InAs_{0.156}P_{0.844}$ / 10.3 nm InP) (mod06), c) 25 × (9.8 nm $InAs_{0.264}P_{0.736}$ / 9.8 nm InP) (mod04), d) 20 × (7.8 nm $InAs_{0.17}P_{0.83}$ / 8.2 nm $In_{0.91}Ga_{0.09}P$) (gp18) and e) 20 × (8.4 nm $InAs_{0.26}P_{0.74}$ / 9.6 nm $In_{0.88}Ga_{0.12}P$) (gp24). For each of the five samples, the series of curves corresponds to the series of increasing electric field values indicated in the inset numbers. Pertinent data for the multi-quantum well stacks are summarized in Table 5-I. 120

Figure 5.6 Energy redshift of the n=1 electron-heavy hole transition as a function of electric field. The curves for a) mod05, b) mod06, c) mod04, d) gp18 and e) gp24 are obtained from the spectra in Figure 5.7. Curve f) is data for a 40 × (10.5 nm $In_{0.53}Ga_{0.47}As$/6.8 nm $In_{0.52}Al_{0.48}As$ - lattice-matched to InP) MQWS operating at 1.55 μm from Ref. 27 and curve g) is data for a 21 × (10.0 nm $InAs_{0.53}P_{0.47}$/14.0 nm $In_{0.84}Ga_{0.16}P$) strain-balanced MQWS operating at 1.55 μm from Ref. 26. 121

Figure 5.7 The unstrained neutral line-up of the five common III-V binary compounds according to the quantum dipole model of Tersoff (Ref. 39) and Tejedor and Flores (Ref. 40). In the theory, the position of the VB maximum relative to a reference midgap level, E_B, may be computed from the bulk properties of the material alone. It is predicted that the bands across a heterojunction interface will be aligned such that the difference between the E_B levels in adjacent materials is small (nearly zero). The positions of E_B relative to the VB maxima are 0.50 eV (InAs), 0.76 eV (InP), 1.05 eV (AlAs), 0.50 eV (GaAs) and 0.81 eV (GaP) These values are reproduced from Ref. 39. The direct gap transitions are shown for GaP and AlAs. 129

Figure 5.8 Two possible strategies for obtaining heterojunctions with large conduction band offsets, small valence band discontinuities in the 25 - 60 meV range and a fundamental optical transition energy near 0.8 eV or 0.95 eV. The band alignments shown for the $In_{0.53}Ga_{0.47}As$/InP and $In_{0.53}Ga_{0.47}As/In_{0.52}Al_{0.48}As$ heterojunctions correspond to widely accepted values (Ref. 45). The band alignment shown for the strained InAsP/InP(001) heterojunction corresponds to the experimentally determined values in Refs. 7, 23 and 43, and agrees well with the model predictions of Ref. 39 130

Figure A.1. The ratio of electronic (V_e) to hole (V_h) barrier heights giving equivalent field-assisted tunneling escape probabilities, as a function of electric field and total well depth ($V_e + V_h$). The data points have been obtained by writing the expressions for the tunneling probabilities at the conduction and valence bands and then solving iteratively for the barrier heights. The relationship plotted here corresponds to $m_e = 0.055m_0$, $m_h = 0.5m_0$ and 10 nm thick barriers 174

Figure A.2. The influence of the finite barrier height on the red-shift of the fundamental hole level in a single 10 nm wide quantum well at 50 kV/cm. The computation has been performed using the variational description of the quantum-confined Stark effect developed by Bastard *et al.* (see Ref. 10). 175

LIST OF APPENDICES

Appendix Band alignment strategy for efficient optical modulation in quantum-confined Stark effect devices. 169

SYMBOLS AND ABBREVIATIONS

1D	1-dimensional (quantum confinement)
2D	2-dimensional (growth mode)
3D	3-dimensional (growth mode)
α	absorption coefficient
α_0,	initial absorption coefficient
δE_C	conduction band discontinuity
$\Delta\alpha$	absorption coefficient change (modulation depth)
ΔE_g	bandgap difference between quantum well and barrier
ξ	dimensionless wave vector; $\xi = kL/2$ where k is the wave vector and L is the width of the quantum well
λ	wavelength
a	lattice constant
$a_{//}$	in-plane lattice constant
a_{free}	unstrained lattice constant
A	area (of p-n diode junction)
ABS	optical absorption
AM0	air mass zero (solar spectrum)
AM1.5	air mass 1.5 (solar spectrum)
BC	bande de conduction

BV	bande de valence
C	capacitance
CB	conduction band
d	interplanar distance
d	thickness of quantum well material
DC	zero frequency component
DI	deionized water
e1	n = 1 conduction band quantum well level
$E1$, E_1	n = 1 quantum well level (generic)
ECR	electron cyclotron resonance (plasma etching)
E_g	bandgap energy
F	electric field
F_c, F_{c0}	recombination rate (solar cell)
FET	field effect transistor
F_s	generation rate due to illumination (solar cell)
f_w	geometrical factor due to solid angle subtended by the sun
FWHM	full width, half maximum
g	diffraction vector (TEM)
GSMBE	gas source molecular beam epitaxy
h, $\hbar$	Planck constant
h1	n = 1 valence band quantum well level

$h\nu$	photon energy
HBT	heterojunction bipolar transistor
hc	critical thickness (Matthews-Blakeslee)
hh1	n = 1 heavy hole quantum well level
HRXRD	high resolution x-ray diffraction
HWHM	half width half maximum
I	electrical current
IC	integrated circuit
I_{sc}	short-circuit current
kT, k_BT	thermal energy
KKI	$HCl:CH_3COOH:H_2O_2$
KPI	$HCl:H_3PO_4:H_2O_2$
L	well width, barrier width
LD	laser diode
L_{eff}	effective well width (of infinite well)
lh1	n = 1 light hole quantum well level
L_0	quantum well width
LP-MOVPE	low pressure metal-organic vapor phase epitaxy
m^*	effective mass
MBE	molecular beam epitaxy
m_e	conduction band effective mass

MDN	misfit dislocation network
m_h	valence band effective mass
m_{hh}	heavy hole valence band effective mass
m_0	electron rest mass
n	refractive index
MQW	multiple quantum well
MQWS	multiple quantum well stack
MOVPE	metal-organic vapor phase epitaxy
PL	photoluminescence
q	electronic charge
$Q(E_g, T_s)$	radiation flux of energy $h\nu > E_g$ from black body at T_s
$Q'(E_{qw}, T_s)$	radiation flux of energy $E_{qw} < h\nu < E_g$ from black body at T_s
QCSE	quantum-confined Stark effect
R	relaxation (strain)
RIE	reactive ion etching
r_{qw}	barrier to quantum well coupling constant
RTP	rapid thermal processing
SC	strong confinement
SEM	scanning electron microscopy
SK	Stranski-Krastanow (growth mode)
t	thickness of active quantum well material

T, (T_s, T_c)	temperature, (solar and ambient)
TEM	transmission electron microscopy
T_{rect}	tunneling transmission coefficient through rectangular barrier
t_s, t_c	probability of electron-hole pair creation from absorption event
T_{trap}	tunneling transmission coefficient through trapezoidal barrier
T_{tri}	tunneling transmission coefficient through triangular barrier
t_{qw}	quantum well to barrier coupling constant
V	voltage (electrical), barrier height (band structure)
VB	valence band
V_e	conduction band discontinuity
V_h	valence band discontinuity
V_{oc}	open-circuit voltage
WC	weak confinement
XRD	x-ray diffraction

1 INTRODUCTION

The effects of the ongoing revolution in information technology and long-haul, high-bandwidth communications cannot be overestimated. If it is even possible to imagine what would have been the *simultaneous* impact of both printing and industrialization on western civilization, the current double revolution promises change, opportunity and the accompanying general anxiety and mayhem that will be far swifter and more radical. Diode lasers, heterojunction bipolar transistors and photodetectors are examples of devices and applications which continue to make copious annual contributions to the list of cryptic acronyms like GRINSCH-SQW-LD, GSMBE, HEMT, HBT, LT-ALE, MODFET, p-i(ESQW)-n, WDM, etc. The need to continually supplement our regular language with new words and expressions is the certain signature of rampant innovation. In light of this, I feel very fortunate to have been able to study and begin to understand one of the branches of scientific research that has played an important role in creating and propelling the new changes. This is the study of thin film semiconductor materials and devices.

Most of the research, development and commercial production in semiconductor materials and devices is dedicated exclusively to Si. After 50 years of intense scientific and commercial activity, Si is now arguably the most well-understood and well-documented material ever. The principal reason for the success of Si as an electronic

material is because it is both superbly manufacturable and relatively inexpensive. However, due to the indirect bandgap, Si has limited applicability for optoelectronics and its electronic properties are significantly inferior to compound semiconductors like GaAs. Since each new generation of devices requires improved performance, the task of extracting further enhancements from a material that is already highly optimized is continuously compounded. We can plainly see that this will not continue indefinitely. So, it is natural to look increasingly to alternative materials.

III-V compound semiconductor materials are the most immediate alternative to Si. In many ways, III-V materials are the antithesis of Si. They possess comparatively superb electronic and optical properties but pose some serious and costly manufacturing problems. Still, in areas such as optoelectronics, high-speed electronics, space and military applications, where no viable substitutes exist, there has been important and substantial progress in bringing compound semiconductors, and particularly III-V materials based on GaAs and InP, to commercialization. More recently, there have been spectacular successes in the production of visible diode emitters and lasers from III-V materials based on GaN.

Central to the success of III-V alloy materials in its limited segments of the market is the ability to manufacture high-quality, low-dimension heterostructures demonstrating quantum confinement effects. Such heterojunction engineering is also possible in Si-

based materials, but the compound materials offer a far richer variety of energy band structures to create and/or enhance specific material properties for device applications. 25 years since the appearance of the first quantum heterostructures in the early 1970's, 1D quantum confinement structures account for nearly all of the current III-V device applications. In research circles, activity in 2D and 3D quantum confinement is currently the subject of hotly-contested competition for stature and recognition, but is not yet sufficiently mature for widespread commercial application. While this continues, there is still much work to be completed in 1D structures. Most of the work to date has been concentrated on the engineering of the energy band gap structure to create the special quantum confinement potentials for device applications. Also of particular interest are the important refinements that may be achieved by engineering the alignment of conduction and valence bands in the heterojunction structures. This is generally a more challenging exercise than band gap engineering from both theoretical and experimental perspectives. But, the rich design space of compound semiconductor heterojunctions appears to be well-suited to it.

This study hopes to demonstrate some of the important research and development issues relevant to the production of a III-V based device. The device is a strained-layer multiple quantum well (MQW) quantum-confined Stark effect (QCSE) optical modulator grown by metal-organic vapor phase epitaxy (MOVPE) and it can be directly related to all of the important issues that have been discussed in this introduction:

information technology, long-haul, high-bandwidth communications, hybrid integration with Si-based electronics, III-V developmental hurdles, quantum confinement and band alignment engineering. The main idea behind the device is based on the special room-temperature band edge absorption characteristics of multiple quantum well structures and the ability to significantly change them with an electric field. Fields on the order of 100 kV/cm are sufficient. So, by burying the multiple quantum wells in the junction of a p-i-n diode, it is possible to create an efficient voltage-dependent optical modulator. The diode is operated in reverse bias and behaves as a simple capacitive load whose electrical bandwidth is limited by its linear dimensions. This makes it possible to have very high operating frequencies (10 GHz - 1 THz) by making the devices small. The potential for impressively high modulation frequencies and the compatibility of the growth and processing of these devices with semiconductor diode lasers have led to widespread interest in their application for high-speed, long-haul optical fiber telecommunications. These p-i(MQW)-n photodiodes also possess enhanced non-linear optoelectronic properties and this has led to their application in photonic switching, optical interconnections and smart pixels.

In January of 1996, we grew a series of compressively-strained InAsP/InP MQW samples varying the strain from 0% - 0.8%. An exhaustive structural and optical characterization of the epitaxial layers was performed and optical modulator devices were fabricated. The experiment was designed to study some of the effects of strain

relaxation on the epitaxial layers and on the operating characteristics of the optical modulators. Rather curiously, a systematic correlation between the drive field required to operate the devices and the barrier height of the quantum wells was detected. Reflecting upon the observation led to the conclusion that this could have significant consequences for the design of the multiple quantum wells for QCSE devices. A second series of samples was produced in June 1997 in which the InP barriers were replaced by tensile-strained InGaP barriers to achieve a large degree of strain compensation in the structure. These structures were characterized, processed and studied by the same methods as before and they provided another demonstration of the drive field - barrier height effect. Having access to such a wide range of detailed physical data allowed the undertaking of a detailed investigation of the important material and device design issues for QCSE optical modulator devices. The effect of the band alignment of the quantum well and barrier on the overall performance of the optical modulator was identified as a key consideration for device design.

Then, the remainder of this document is an account and discussion of the work on QCSE optical modulators, covering the range from initial device processing experiments to the proposal of novel concepts in the engineering of band alignments for devices, that was pursued during the last 55 months in the MOCVD, LISA (Laboratory for Integration of Sensors and Actuators) and MODFAB (Microelectronic and Optoelectronic Device Fabrication) laboratories of the Engineering Physics Department of the École

Polytechnique de Montréal and in the optical characterization laboratory of the Department of Physics of the Université de Montréal.

2 EXPERIMENTAL METHODS AND BACKGROUND

In this chapter, we present a description of the experimental considerations and procedures that were used to realize the study. Primary emphasis is placed upon the growth, characterization and design of the epitaxial layers with a secondary emphasis on the device processing steps.

2.1 *Sample cleaning*

InP substrates and epitaxial layers are prepared before processing with a cleaning procedure. The goal is to remove contaminants and prepare the surface of the sample for material growth or processing. Samples are degreased in heated organic solvents, 10 minutes in each of: acetone followed by propanol followed by de-ionized water (DI). Acetone decomposes when overheated so care must be taken not to boil it. Propanol, on the other hand, may be boiled without adverse effects. After degreasing, a wet chemical oxidation followed by oxide strip may be performed to reveal fresh, clean semiconductor surface, if required. The oxidation and strip procedure that we use, called pirhana strip,[1] is common in Si wet bench processing. The samples are strongly oxidized by immersing in a room temperature solution of H_2SO_4:H_2O_2 (5:1). The dip effects a controlled oxidation at the surface of the sample that consumes semiconductor material to create a clean interface between oxide and semiconductor while oxidizing and removing organic

and metallic contaminants. After diluting the pirhana strip solution and rinsing in DI, the control oxide may be stripped immediately prior to further processing by dipping in a weak acid. For Si, the oxide is most effectively removed with a dip in weak HF solution (1-10%). For InP, a weak HCl solution is more effective. The native oxides that form at the surface of InP may be easily stripped by dipping in a solution of weak HCl (1 - 10%). The oxidized surface of InP is hydrophyllic while the bare semiconductor surface is hydrophobic. Samples being prepared for growth are not stripped in weak acid. They are placed in the growth chamber, where the oxide is stripped during the ramp up to the growth temperature (~ 500 °C - 700 °C) followed by a 10 minute anneal under PH_3 ambient.

2.2 *Growth of strained-layer, InP-based thin film materials by MOVPE*

The strained epitaxial layers are grown by metal-organic vapor phase epitaxy (MOVPE). A complete description of the theory and practice of vapor phase epitaxy using metal-organic precursors is given by Stringfellow.[2] Practical details related to the growth of InP-based materials in our reactor have been extensively documented in the theses of P. Cova,[3] C. A. Tran,[4] A. Bensaada[5] and H. Marchand.[6] Excellent introductions to the epitaxial growth of strained layers are provided by Pearsall[7] and Hull and Bean.[8] In this section, we describe briefly some specific issues concerning the growth of strained layers relevant to our experiments.

When growing thin layers of a crystalline material onto a chemically dissimilar substrate (heteroepitaxy), the observed growth modes are traditionally identified as belonging to one of three general classifications.

1. Growth may proceed layer by atomic layer, called the two-dimensional (2D) or Frank-Van der Merwe mode. For device applications, it is almost always necessary to maintain 2D growth to achieve high crystalline quality.
2. Growth may proceed in clusters, called the three-dimensional (3D) or Volmer-Weber mode.
3. Growth may proceed initially by the 2D mode for several mono-layers and then subsequently shift to the 3D mode, called the hybrid or Stranski-Krastanov[9] (SK) mode.

Various models exist to describe the conditions which favor one growth mode over another. These models are constructed by considering the energetics of the strained-layer, of the growth surface and of the precursor species adsorbed onto the growth surface. Overviews and discussions of many of these important issues can be found in the theses of H. Marchand[6] and P. Desjardins.[10]

The deposited heteroepitaxial layer often has a different lattice constant[11] from the host material. This gives rise to a lattice misfit that may be accomodated in several ways. For small misfits, the growth mode is preferentially 2D and leads to a pseudomorphic deformation of the layer. In comparison, the deformation of the host[12] may be neglected because it is many times thicker and possesses a similar modulus of elasticity. Therefore, the layer deforms elastically to adopt the lattice of the host in the plane normal to the growth direction with a corresponding elastic deformation in the orthogonal (growth) direction. For large misfits and/or thicker layers, the strain energy density in the crystal can become sufficient to activate a variety of strain relaxation mechanisms: 1) relaxation via misfit dislocations, 2) relaxation via 3D layer growth and 3) relaxation via composition inhomogeneities and segregation. Much of the activity in the science of crystal growth is dedicated to a study of these relaxation mechanisms and how they may be affected by manipulating the growth conditions.

The most studied and best understood relaxation mechanism is the formation of misfit dislocation networks in the crystal. As the thickness of a strained layer grows, it reaches a critical limit where the strain energy density at the strain interface is sufficient to generate lattice dislocation defects. This concept of a critical layer thickness is central to any discussion of strain relaxation. Briefs historical accounts of the theories of critical layer thickness for the formation of misfit dislocations can be found in any of a number

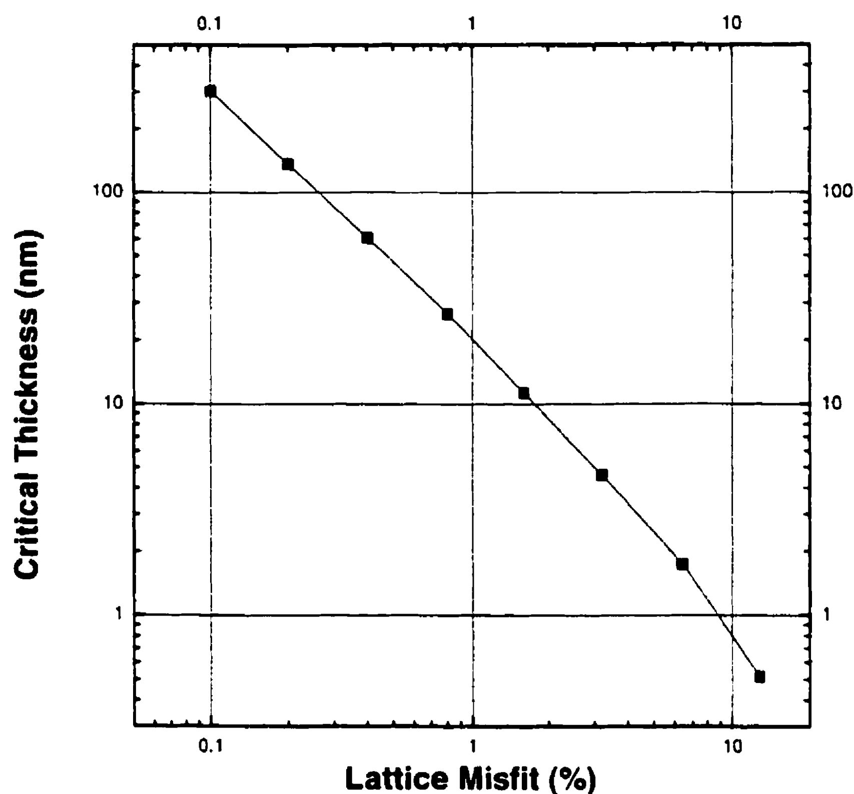

Figure 2.1 Critical thickness for the formation of misfit dislocation calculated using the Matthews—Blakeslee force balance model (see Ref. 15).

of excellent references (eg. Hull and Bean[8], Beanland et al.[13] or Yu et al.[14]). The critical thickness is usually calculated by balancing the strain energy of the layer against a critical energy for the formation of dislocations. A plot of the critical thickness versus layer strain produced using the well-known Matthews—Blakeslee[15] force balance model is shown in Figure 2.1.

The practical limitation of energy balance formulations is that they rely on the crystal reaching a state of thermodynamic equilibrium. From experiments, it is possible to grow non-equilibrium, metastable structures. For example, pseudomorphic, dislocation-free strained layers exceeding the critical thickness for equilibrium structures are often produced by resorting to low growth temperatures. This is evidence that there exist energy barriers to the formation of misfit dislocations. Therefore, the formation of misfit dislocations is strongly dependent on the growth conditions in addition to the equilibrium energy balance. And, we may grow defect-free non-equilibrium, or metastable, structures by choosing the appropriate growth conditions to suppress dislocation formation.

It is widely observed across numerous material systems that the 2D growth mode becomes unstable for misfits larger than ~ 1.8 %. When layer strains exceed ~ 1.8%, the layer strain energy density becomes sufficient to affect the growth mode and the layer morphology becomes prone to complex roughening transitions. The growth is initially 2D and undergoes a transition from 2D to 3D with increasing layer thickness. Such a hybrid (SK) growth mode is usually identified with the model proposed by Stranski and Krastanow. Growth proceeds initially with a 2D deposition of a pseudomorphic 'wetting' layer that is several (usually 1-2) monolayers thick. The elastic strain energy at the free surface of this layer is sufficient to induce the nucleation of clusters so that subsequent growth via a 3D mode. For example, Chen *et al.*[16] have reported observing that

preferential sites for 3D island nucleation may be provided by small spatial variations in the surface strain distribution. SK growth has recently received much attention because with proper control of the growth conditions, it is possible to grow hemispherically-shaped islands of dislocation-free, pseudomorphic material. In addition, it is possible to grow islands that are relatively uniform in size and that exhibit a large degree of auto-organization. The size and ordering of the islands makes them suitable for zero-dimensional confinement device applications. The SK model successfully describes the qualitative aspects of the 2D-3D transition. But, Cunningham and Goosen[17] remarked that it habitually fails to correctly predict the critical thickness at which the 2D-3D transition occurs. Furthermore, they noted that the hemispherical shape is inconsistent with III-V growth, which is known to proceed preferentially on well-defined crystal facets. They have proposed a model for 3D growth based on strain-induced (113) and (114) faceting when growing on GaAs(001).

A prime initiative of the art and science of crystal growth is to exert some degree of control over the layer morphology by manipulating the growth conditions to suppress or enhance specific relaxation mechanisms, and produce high quality metastable structures. Tersoff and Legoues[18] have remarked that strain relaxation process may be viewed as a competition between two mechanisms: surface roughening and misfit dislocations. They note that the surface of any strained layer is inherently unstable to undulations and roughening. But, the surface roughening process is thermally activated

and has an energy barrier that increases rapidly with decreasing layer strain. Therefore, this argument concludes that growth is preferentially 2D below some critical strain and it is possible to increase this critical strain by changing growth conditions such as the temperature. The remarks of Tersoff and Legoues underline the more general view that any number of competing relaxation mechanisms may be present, each of which exhibits its own characteristic energy barrier(s). Growth experiments, notably in MBE, have demonstrated that the 2D-3D transition can be suppressed by reducing the growth temperature, which has the effect of reducing the thermal lattice energy available for relaxation processes. Experiments have also shown that increasing the element V overpressure and/or growth rate can also have an effect on maintaining the stability of the 2D planar growth mode. These latter experiments reveal that the 2D-3D transition is highly sensitive to the surface mobility of the adsorbed group III species on the sample surface. Methods designed to suppress the 3D growth mode by limiting the diffusion of adsorbed species on the free surface have significant practical implications for growth by MOVPE. The growth temperature is always the most important parameter because nearly all of the growth and relaxation processes are thermally activated. But, in diffusion-limited[19] MOVPE, the growth temperature cannot be reduced significantly below 500 °C like it may be for growth by MBE. On the other hand, higher growth rates and a wider variety of growth conditions by changing the flow, pressure and chemical environment are available in diffusion-limited growth by MOVPE. This is partial

compensation because it offers a greater number of possible growth strategies and potentially, a finer degree of control over the growth surface.[20]

The third mechanism mentioned in the first paragraph of this section is relaxation by composition inhomogeneities and segregation. It arises mostly due to large differences in the sizes of the atoms forming the strained layer. There is a tendency in the crystal to remove the large atoms in order to relieve the strain. The large atoms migrate to and accumulate at favorable locations in the crystal, often the free growth surface. This is widely observed and studied in the growth of $Si_{1-x}Ge_x/Si$ strained layers. As with the other relaxation mechanisms, it is possible to suppress segregation to a large degree and produce metastable structures by choosing special growth conditions. For example, although the equilibrium solid solubility of Sn in Ge is < 0.01, Gurdal *et al.*[21] succeeded in producing $Ge_{1-x}Sn_x/Ge$ superlattices with x up to 0.24 by reducing the growth temperature into the sub-150 °C range. Surface segregation is generally not a prominent problem in the epitaxy of traditional GaAs and InP-based III-V strained layers. However, a striking example of surface segregation in III-V materials is provided by Antonell and Abernathy[22]. Their growth experiments on Tl-V and InTl-V compounds by gas source MBE demonstrated severe surface segregation of Tl rich alloys and the formation of pure droplets of metallic Tl.

For device applications, strain asymmetries in the lattice can make favorable modifications to the energy band structure of the material and the best performance is generally achieved with the maximum allowable strain. Therefore, it is our challenge to find methods to grow highly-strained layers and suppress these strain relaxation mechanisms and/or localize the damage to the crystal away from the active region. Aside from control of the surface morphology of the strained layer, we mention two other strategies.

1. A thick, strained buffer layer may be grown onto the host substrate that contains and confines the misfit and threading dislocations.[23,24,25] This is effectively a method of creating an interim substrate with a smaller misfit relative the target device layer.
2. Alternating layers of tensile and compressive strained material may be grown so that the product of average strain and thickness of the composite sequence does not exceed the critical limit for the formation of misfit dislocations.

In principle, these are viable techniques for extending the design space of strained layers for devices but there are still important technical and developmental problems to be resolved. The possibilities for continued research on the crystal growth issues are vast. Here are four growth experiments that can be pursued immediately.

1. Suppression of the 2D-3D growth transition in highly-strained planar InAs(P)/InP and InAs(P)/InGaAsP heterostructures by changing the growth conditions (temperature, deposition rate and element V overpressure).
2. Growth of self-assembled 3D islands in highly-strained InAs(P)/InP and InAs(P)/InGaAsP heterostructures using the 2D-3D growth transition.
3. The use of strain relaxed buffer layers to limit and confine threading dislocations. Variations on this include compositional grading and small area mesa growth strategies.
4. The use of alternating strain to achieve a high degree of strain compensation to extend the critical thickness of the superlattice stack.

2.3 *Structural characterization by x-ray diffraction*

High-resolution x-ray diffraction (XRD) is a workhorse technique for structural characterization of the epitaxial layers. It is a powerful, non-destructive measurement that can provide detailed information about the state of strain and morphology of the layer. It can also be easily adapted to provide rapid and accurate feedback. When XRD data is complemented with TEM and optical data, it is possible to obtain a very complete characterization of a sample. Our XRD measurements are performed using 0.15406 nm radiation from the $K_{\alpha 1}$ transition in Cu, a four Ge crystal Bartels cell monochromator and Philips diffractometer. The diffractometer is also equipped with a separate 2 crystal

analyzer at the detector to permit the acquisition of reciprocal space lattice maps. Such maps can provide extremely detailed data. The background theory of the XRD analysis is extensive and we will not describe it here. Proper, detailed descriptions of the methods that we have employed can be found in Refs. 26, 27, 28, 29, 30 and 31.

In most cases, we measure only simple (004) reflection symmetry rocking curves that allow a rapid characterization of the epitaxial layers for feedback to the MOVPE growth experiment. Acquisition times for scans may vary from several minutes to several days depending on the detail and accuracy of the information sought. As a special application of the XRD measurement for MOVPE, note that there are three parameters that may be extracted rapidly from a fast (< 30 minutes) (004) scan: the average mismatch of the layer, the superlattice period and the thickness of the cap layer. This is very important because it allows for adjustments to the growth parameters in between samples. By properly designing and coordinating the growth of test structures, it is possible to obtain immediate and accurate feedback about the growth conditions in the reactor.

To see why this is important, note that the various techniques commonly used to grow high-quality epitaxial layers of semiconductor materials can be divided into two general classifications: high vacuum methods (molecular beam epitaxy, MBE) and low or atmospheric pressure methods (metal organic vapor phase epitaxy, MOVPE). The

high vacuum methods are compatible with the use of a wide variety of in situ characterization techniques allowing dynamic observations to be made at the surface of the material during the growth process. In the case of the low pressure methods, growth may be performed at pressures ranging from 20 torr to atmospheric. This can greatly simplify many of the practical aspects related to the conception and maintenance of the growth chamber, permit a wider flexibility in the growth conditions and allow more elevated growth rates for higher throughput. The drawback, of course, is the general lack of available in situ information. The development of in situ growth monitoring techniques for MOVPE continues to advance steadily but historically, growth by MOVPE has relied heavily on ex-situ techniques such as X-ray diffraction (XRD), photoluminescence (PL), optical absorption (ABS) and transmission electron microscopy (TEM). As we have mentioned, these methods are highly complementary and allow us to form a coherent picture of the nature of the layers grown. However, a complete characterization is time-consuming whereas some initial feedback is often required immediately. XRD is best suited to this task and MOVPE operators usually become adept at interpreting the XRD spectra from their epitaxial layers.

The following example shows how it is possible to design a test structure that allows us to rapidly deduce three important growth parameters from a single XRD rocking curve that may be acquired in 15 - 30 minutes. Longer scans with less noise and more precise fits can be performed but the goal in the present case is to be able to

provide some useful immediate feedback. We can try to exploit two key points in XRD rocking curves. The characteristic scattering pattern of a section of crystal of finite thickness, t, is a single peak centered at an angle, θ, corresponding to a characteristic lattice period, d, that is modulated by a regular fringe pattern.

1. The thickness of the layer, t, may be related to the fringe spacing, $\Delta\omega$, by:

$$t = \frac{\lambda}{2\Delta\omega\cos\theta} \tag{2-1}$$

The angular separation, $\Delta\theta$, between the peak corresponding to lattice period, d, and a peak corresponding to a known reference (usually the substrate on which the layers are

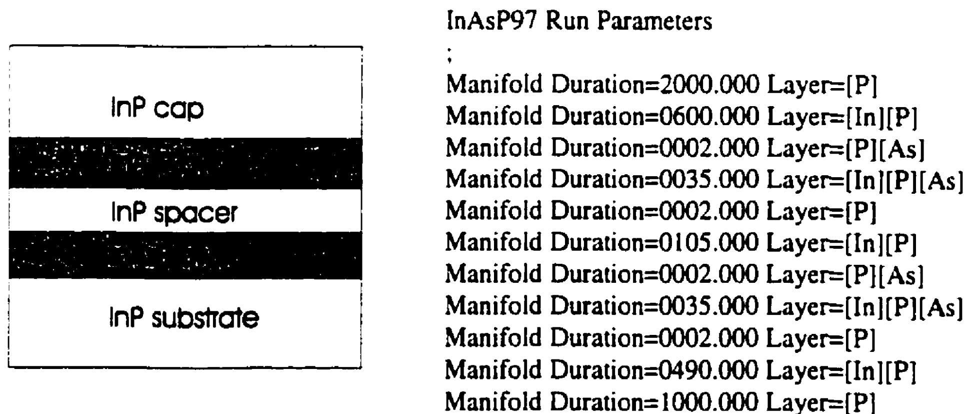

Figure 2.2 Double quantum well InAsP/InP test structure used to measure and calibrate growth parameters. The gas flow sequence for the structure is indicated on the right. Manifold duration is measured in seconds. [In], [As] and [P] refer to the flow of precursor species. By careful choice of the thicknesses of the InAsP quantum well, InP spacer and InP cap layers, it is possible to deduce the growth rate of the InAsP and InP, and the As incorporation from a single XRD rocking curve that may be acquired in 15 - 30 minutes.

grown), d_0, may be related via :

$$\frac{d-d_0}{d_0}=-\frac{\Delta\theta}{\tan\theta} \tag{2-2}$$

The test structure depicted in Figure 2.2 is a double InAsP/InP quantum well with an InP cap layer.

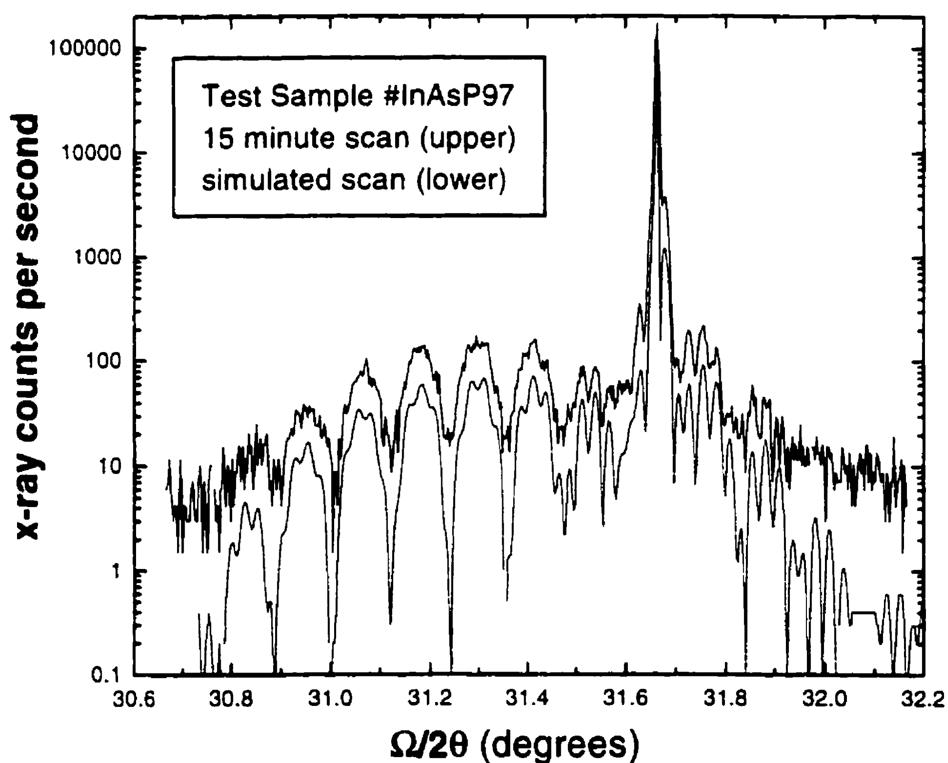

Figure 2.3 XRD (004) rocking curve (upper) and simulation curve (lower) for the sample in Figure 2.2. The data acquisition time for this curve was 15 minutes.

In (004) x-ray rocking curve of Figure 2.3, fitting the small, high frequency fringe period gives the InP cap thickness and also the thickness of the InP spacer via the ratio of their growth times. Fitting the large, low frequency fringes (multiple bump structure) gives the period of the InAsP/InP superlattice. Therefore, since the thickness of the InP spacer is known accurately, so is that of the InAsP quantum well. The position of the multiple bumps relative to the InP substrate peak is a sensitive function of the average As content in the superlattice. While the bump maxima are broad, the bump minima are sharp and well-defined. Therefore, fitting the bump minima relative to the InP substrate peak gives the As content in the quantum wells. When properly designed, this double qw test sample has enough redundancy that a reasonable fit of the simulated to measured spectra is impossible if any of these three parameters is far from its true value. For this sample we find the growth rates and As incorporation to be: InP (0.315 ± 0.005 nm/s) and InAsP (0.315 ± 0.008 nm/s, 22 ± 2 % As).

Basic symmetric and asymmetric reflection rocking curves and the information that can be extracted from them are the most straightforward application of the possible XRD characterization methods. Recommendations for continued work with more sophisticated measurements include:

1. Reciprocal lattice maps.
2. Specular reflectivity, low-angle XRD measurements.

3. Complementary ellipsometric measurements.

2.4 *Wet chemical etching of InP in HCl-based solutions*

In order to produce photodiode structures, a method is required for fast, smooth etching of InP and related alloys to produce mesa structures for electrical isolation of the devices. Both wet and dry etch techniques are applicable. Etching in wet chemical solutions generally provides faster material removal rates (~ 100 - 2000 nm/min) and good passivation of the mesa sidewalls and other etched surfaces. Smooth dry etching of InP in plasma environments is also possible. These techniques are known as reactive ion etching (RIE) and electron cyclotron resonance (ECR) etching. Dry etches can be highly anisotropic and permit finer control of the etched depth and generally much finer control of the lateral etch dimensions. However, the material removal rates are much lower (~ 20 - 40 nm/min) and the exposed etch surfaces suffer significant radiation damage. An excellent discussion of some important issues involved in the production high-quality mesa structures is given by Sloane.[32] In our case, HCl-based wet chemical etch solutions were chosen because of many reports of the good etching characteristics on InP and since the reagents are widely available and do not require special safety procedures beyond the usual precautions for strong acids.

MoD4 after etch2

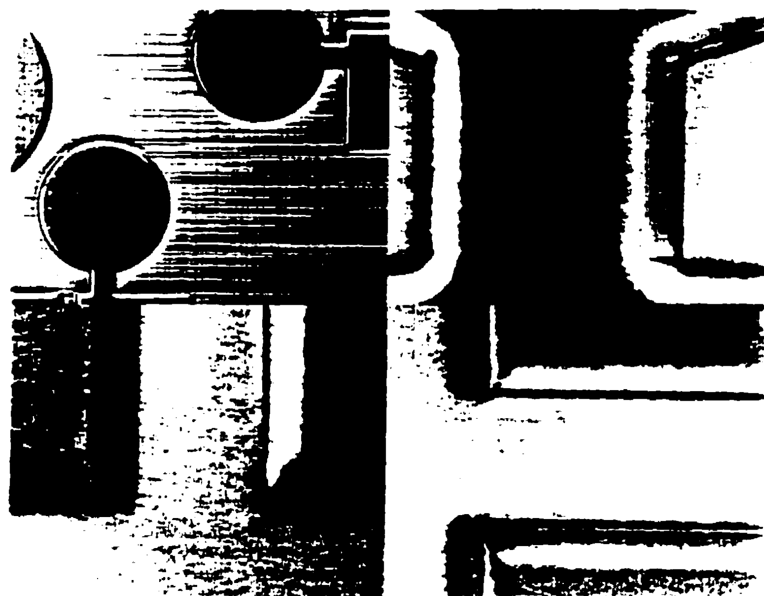

Figure 2.4 InAsP/InP multiple quantum well sample after etching in a solution of $HCl:CH_3COOH:H_2O_2$ (viewed with an optical microscope using Nomarski contrast). The etched depth is 0.63 μm. The striations in the etched surface (top left) are due the the effects of the layer strain and the presence of misfit dislocations. Significant lateral advance of the etch front underneath the photoresist etch mask is clearly visible (top right, bottom left and right). The width of the photoresist neck in the top right photograph is 40 μm. The separation of the photoresist corners in the bottom photographs is 20 μm.

Most of the wet etching experiments were based on the work of Kambayashi *et al.*[33] and Adachi *et al.*[34] using the $HCl:CH_3COOH:H_2O_2$ (KKI) system. Kambayashi *et*

al. reported that KKI could be used with sufficient fine control to obtain mesa structures with mirror end facets suitable for fabricating laser diodes. The samples were patterned with positive photoresist etch masks and immersed in the etch solutions according to the recipes given in Refs. 33 and 34. We confirm that KKI solution does etch InP rapidly with good surface morphology. However, we also observe some important problems associated with KKI. The solution stability is poor. Upon mixing HCl with H_2O_2, the solution begins heating. The etch rate was observed to increase with the rise in temperature and runaway after 10-15 minutes. Also, there was significantly enhanced etching beneath the mask edges with a rapid (2 - 3 μm/minute) lateral advance of the etch front (see Figure 2.4).

Some of these observations were also reported by Flemish and Jones.[35] They note that the buffer acid serves the role of a non-aqueous solvent. This is necessary since Notten[36] reported that HCl solutions weaker than 5ML gave negligible etch rates for InP, thus leading to the conclusion that the etch rate of InP in HCl-based solutions is strongly dependent on the concentration of molecular HCl. Flemish and Jones explained that the poor stability of the KKI solution is due to the exothermic oxidation of Cl^- ions in aqueous solution by H_2O_2 producing heat and Cl_2. The presence of Cl_2 dissolved in solution compounds the problem of etch control since is Cl_2 can rapidly etch InP. We confirm that within minutes of mixing HCl and H_2O_2, a strong odor due to Cl_2 is detectable and the KKI solution develops a yellow tint. Flemish and Jones report that

the etch rate of the solution may be stabilized by increasing the amount of the non-aqueous solvent, CH_3COOH, and by adding H_2O_2 only just prior to etching. The goal is to maintain a sufficient concentration of molecular HCl in the presence of an oxidizing agent to achieve fast, smooth etching while suppressing undesirable effects such as auto-heating of the solution and the formation of Cl_2. We confirm that this does stabilize the solution but that it also reduces the etch rate so that far longer etch times are required. Our observed etch rates were also generally inferior to those reported in refs. 33, 34 and 35. This is likely due to the highly variable quality of the H_2O_2 reagent available in the laboratory. H_2O_2 degrades rapidly upon exposure to light and heat. More recently, the CH_3COOH buffer solvent has been replaced with H_3PO_4 (KPI) and we found that this improves the stability of the solution. However, enhanced etch rates underneath the mask edges and lateral etch fronts that are able to advance at alarming rates are still observable. It is unclear whether this is due to the diffusion-limited removal of active chemical species, insufficient adhesion between the photoresist mask layer and the InP surface, some combination of these two, or other mechanisms.

Despite these problems, both KKI and KPI solutions were used to successfully etch 1 - 3 μm deep mesa structures. Our understanding and control of these etch solutions is so far only adequate for our limited purposes. Much refinement is possible and other groups have successfully applied both solutions to produce high aspect ratio

mesas with small lateral dimensions suitable for waveguide devices. Suggestions for further investigation include:

1. The effect of stirring and non-stirring of the solution during etch on the stability of the solution and on etch rates beneath the mask edges.
2. Ensure fresh, non-degraded H_2O_2 solution. This should increase the vertical etch rate and perhaps even resolve much of the lateral etch problem by minimizing etch time and exposure of the sample to Cl_2 accumulated in the solution. We could also experiment with other more stable oxidizing agents such as $K_2Cr_2O_7$.
3. Study and identify the key etch planes. By properly designing and aligning the mesa structures along preferred crystal directions, it should be possible to minimize the ratio of vertical to lateral etch.
4. The revelation of striations in the crystal by etching that may be due to strain and/or dislocations is another possible method for characterizing strain and relaxation. Often, these signatures are also visible on the unetched surface when using Nomarski contrast to view under an optical microscope.

2.5 *Au-based contact metallizations on InP*

In order to operate the photodiode and manipulate electric fields in the junction containing the quantum wells, a method of establishing low impedance, resistive electrical contact to the p and n-doped semiconductor layers is required. This is done by depositing metal onto the sample surface and performing a post-deposition heat treatment to form a metal/semiconductor contact. Au-based alloys are the most commonly used metallizations on InP. There are vast numbers of reports in the literature on ohmic contact metallizations to InP.[37,38,39,40,41,42,43] Au is a popular metallization on InP because good results can be obtained. But there are significant technological problems caused by the Au-InP chemistry. Often, violent mixing of InP and the Au alloys due to solid state diffusion occurs rapidly upon heating the sample to form the contact. This makes it difficult to reliably fabricate shallow junction devices. Long-term degradation due to contact migration is also known to occur in many InP-Au alloy contact systems.

Lift-off photolithography is used transfer metal patterns from a photomask onto the sample surface. The samples are pattern by contact photolithography using photoresist designed for lift-off processing (OCG BPRS100).[44] It is also possible to use an older method where conventional photoresist was dipped in chloro-benzene for 5 minutes prior to development to harden the surface of the photoresist and create the re-

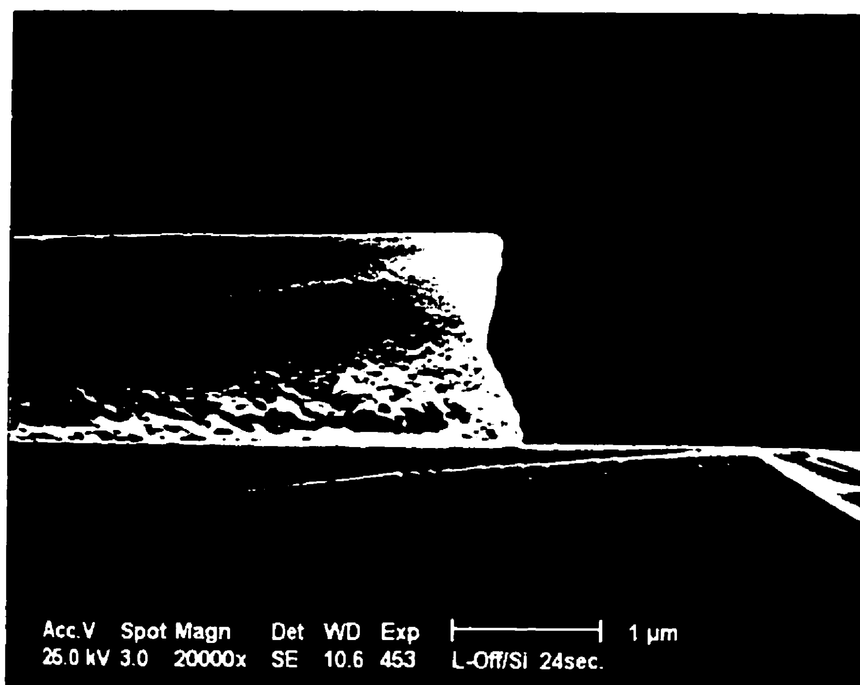

Figure 2.5 SEM micrograph of a lift-off photoresist profile on Si substrate. The thermal evaporation of a metal film onto the re-entrant photoresist profile facilitates the formation of a clean discontinuity in the metal film. A subsequent dip in a photoresist stripper, or solvent such as acetone, removes the unwanted metal and transfers the photomask pattern to the sample.

entrant PR profile upon development (see Figure 2.5). Immediately prior to being placed in the evaporator, the samples are dipped in a weak HCl solution for 5 minutes to remove the native oxide, diluted down to $< 0.01\%$ HCl, and then dried with a N_2 jet. Following this, the samples are placed in the evaporator and maintained overnight at

10^{-4}-10^{-5} torr. Following pump down to 2- 4 × 10^{-6} for 60 - 120 minutes, the evaporation is performed. Pure metal specimens are on W filament boats that are resistively heated. The sample is shielded from the metal source by a shutter. Power to the filament is slowly ramped up until the detector placed near the sample indicates a stable deposition rate of 0.5 - 1.5 nm/s. Metal is then deposited on the sample (usually between 50 - 300 nm) by opening the shutter for a pre-determined duration. A dip in ACE strips the PR leaving behind the desired pattern. Depositions of Au/Ge/Ni and other metals (Ti) with sufficiently high evaporation temperatures was straightforward but the deposition of Au/Zn alloys required some ingenuity. The main problem is posed by the low evaporation temperature and high vapor pressure of Zn. We found that the direct thermal evaporation of metallic Zn was impossible to control. Successful contact depositions were performed with the aid of an Au-10%wt Zn alloy. The evaporation proceeds with the deposition of a thin 5 nm wetting layer of pure Au metal on InP, since the adhesion of Zn on InP is poor. This is followed by the sequential evaporation of Zn and then Au from the alloy, leading to a graded Zn-Au top layer.

The contacts anneals are performed in a AG & Associates Heatpulse 410A rapid thermal processing (RTP) oven. The oven consists of two banks of quartz halogen lamps, above and below the sample. The heating cycles are executed with a programmable computer-controlled lead-lag circuit using the signal from a Si thermocouple placed beside the sample to complete the feedback loop. The sample is

placed face up on a Si wafer and covered with a second wafer of Si or InP. The anneal chamber is purged with N_2 and N_2-10%H_2, ramped to 80 °C and held for 2 minutes. This stabilizes the start conditions for the RTP cycle. The RTP cycles consist of a ramp (20 - 200 °C/s) up to the anneal temperature followed by a steady-state hold at a preset temperature in the range 300-450 °C for a duration of 1s up to a several minutes. It is important to note that thermal anneal cycles performed in rapid anneal ovens differ from those performed using hot-plate, or thermal oven methods. With a hot plate, or conventional oven, heating occurs almost entirely by thermal contact. It is possible to stabilize and accurately monitor the plate or oven temperature. So, we can be certain that the temperature of the metal/semiconductor interface reaches at most the plate/oven temperature. In RTP processing, however, heating occurs by thermal contact and by absorption of the radiation from the heating lamps. It is generally not possible to measure directly the true temperature of the thin metal film and metal-InP interface and we can only infer it from the Si-imbedded thermocouple signal. However, both the optical absorption and thermal heat capacity of the thin film metal alloy and semiconductor interface are likely to be somewhat different from that of the thermocouple, which corresponds to a 500 μm thick slab of Si.

After the anneals are completed, I-V characterizations of test structures are performed by injecting a controlled current and detecting the voltage developed across the test load, which may be a diode, contact, etc. These measurements are performed

Figure 2.6 A 5 nm Au/ 200 nm Au-10%wt. Zn film on Zn-doped InP after a short anneal of 2 s at 300 °C (viewed with an optical microscope using Nomarski contrast). Before annealing, the metal film was uniform sheet of Au. The changes in the color and morphology of the metal sandwich layer indicate that significant microstructural changes have occured.

with a HP4155 semiconductor analyzer. Contacts formed to undoped or highly n-doped InP using the Au/Ge/Ni system are habitually ohmic with varying contact resistivities. In fact, the n-contacts are often ohmic upon the initial deposition of Au-Ge-Ni metal without a thermal anneal. Contacts formed to p-InP however, typically show a low impedance, leaky Schottky diode behavior.

Figure 2.7 A 200 nm Au-10%wt. Ge-5%wt. Ni film on S-doped InP after a short anneal of 2 s at 430 °C (viewed with an optical microscope using Nomarski contrast). Before annealing, the metal film was uniform sheet of Au. The color and morphology of the metal sandwich layer show that a very significant interaction between metal and InP has occurred.

Numerous studies on the optimization of metal layers and anneal sequences for achieving low contact resistivities exist in the literature.[45] But generally, the more serious technological problem is the rapid interdiffusion and mixing of Au and In at the interface and not the contact resistivity. Upon heating to sufficiently high temperatures (> ~300 °C), In diffuses rapidly into the Au film and Au penetrates deeply into the InP

material.[46] This poses grave problems for the fabrication of shallow junction devices such at HBTs, FETs and solar cells. We observed that thermal anneals of 5s at 380 °C were sufficient to allow the Au/Zn alloy to punch through a 300 nm thick p-doped InP cap layer and completely short-circuit the diode. Similar results were observed for 100 nm thick p-doped AlGaAs cap layers on GaAs/AlGaAs p-i(mqw)-n samples. After anneal cycles with only very modest thermal loads (300 °C, 2s), the color and morphology of the metal film changes radically (see Figure 2.6 and Figure 2.7). This is very clear evidence that the processes of solid state diffusion have low activation energies and may occur extremely rapidly. The shortest anneal sequences tended to produce the best results consistent with a need to limit the interfacial reaction and diffusion.

These are certainly non-ideal contacts. But, extremely low contact resisitivities were not required for our purposes since the photodiode junction is operated exclusively in reverse bias. A reverse bias applied to the p-n junction is a forward bias applied to any weak metal-semiconductor Schottky junctions. The impedance of a forward biased metal-semiconductor contact (~ 100 - 1 kΩ) is much lower than that of the p-n junction in reverse bias (~ 10 MΩ). Therefore, the fraction of the total applied voltage developed across the metal-semiconductor contacts is negligible with nearly the entire applied voltage always being developed across the junction of the photodiode. Furthermore, our

devices employed large area contacts (~ 200 μm × 200 μm), which allows a large process window. To see why, consider the leading order behavior of the non-ideal metal-semiconductor contact modeled by a leaky Schottky diode. This behaves essentially as the parallel combination of a regular diode with a finite breakdown field and a resistor. As the cross-sectional area, A, of the diode increases, the resistive branch scales as $1/A$ while the rectifying branch remains unchanged. Therefore, a contact metallization procedure may produce very different I-V curves depending on the size of the contact. Contacts with sufficiently large areas behave as low impedance resistors since the resistive branch dominates the total transport of charge. Meanwhile, smaller area contacts that are otherwise identical behave as a leaky Schottky diodes when the rectifying path has a similar or lower impedance than the resitive branch.

In cases like ours, it is possible to work around these pitfalls associated with the Au-InP contact and obtain acceptable results. But, the main goal of a contact metallization is to find a reliable method for creating a clean, stable, low-impedance metal/semiconductor interface with minimal interdiffusion and contact penetration. The available literature on contact metallizations to InP and GaAs is filled with wildly varying strategies for achieving this. Some examples:

1. Ti/Pt/Au[47,48] contacts to both n-InP and p-InP are a viable option if slightly elevated contact resistivities can be tolerated. A good discussion of the behavior of the interface dynamics of Ni, Pt, Ti and Mo on InP is given by Ashizawa et al.[49]
2. More recently, it was reported that the addition of trace quantities of Zn to the Au film InP led to stabilization of the interface and the elimination of the interdiffusion.[50] The authors of this report propose that the diffusion of In in the Au matrix is interstitial and that the trace quantities of Zn block the intersites.
3. The authors of Ref. 46 deposit a thin 5 nm of the Au alloy and perform the anneal sequence allowing the material mixing to take place. Once all the Au has been consumed, no further penetration of the metal into the semiconductor is observed. A second, thick evaporation of Au metal onto the low resistivity InP-Au/Zn complex then provides the connection to external elements.

In conclusion, there are two issues of *equal* importance that need to be addressed: minimum contact resistivity and minimum contact penetration. A good contact technology must satisfy both of these requirements. Unfortunately, many of the studies in the literature systematically neglect the issue of contact penetration. For example, the applicability of results obtained from studies of contact metallizations and anneal sequences performed using substrates[40,43] is highly questionable. Such studies are performed on materials that are often doped well beyond attainable levels in epitaxial

layers[51,52] and completely neglect any analysis of contact penetration into the semiconductor material.

2.6 *Measurement of field-dependent absorption curves by photocurrent detection*

Measurements of the electric field-induced changes to the band edge absorption spectra are performed by detecting the photocurrent response to a tunable monochromatic illumination source. Electric field-dependent absorption spectra for the multi-quantum well stacks were measured by detecting the photocurrent response of the diodes as a function of the wavelength of the input radiation and the reverse-bias voltage. The experimental apparatus is depicted in Figure 2.8. Illumination provided by a quartz halogen broad spectrum bulb (150W). The radiation emitted from the bulb is modulated with a chopper and focussed into a 0.3 m scanning grating monochromator. At the exit port of the monochromator, the higher order Bragg reflections of short wavelengths are low pass filtered by either a red crystal or GaAs wafer. The remaining IR radiation is focussed onto the photodiode. The photocurrent signal from the diode is AC coupled to a lock-in amplifier. The capacitive voltage divider circuit allows the adjustment of the bias voltage, protects the diode against power transients and blocks the DC offset and drift signals from reaching the lock-in. After the acquisition, the exact offset in terms of wavelength is adjusted by comparison with true absorption spectra

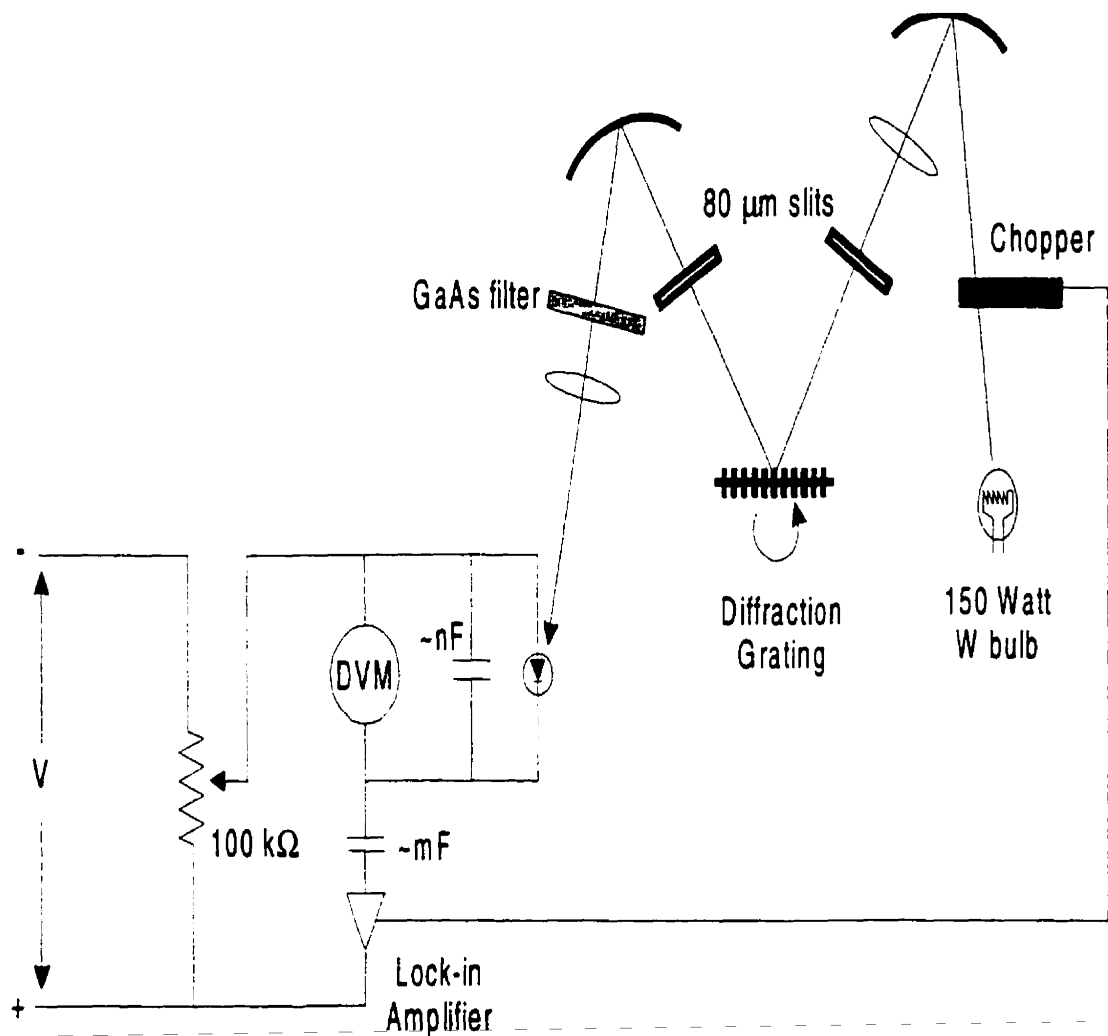

Figure 2.8 Experimental set-up for measurement of the electric field-dependent changes of the optical absorption in the p-i(MQW)-n photodiodes.

obtained for the device layers using the BOMEM DA3 Fourier Transform interferometric spectrometer.

2.7 *Additional remarks*

Before continuing, it is appropriate to acknowledge and clarify the important contributions of the other members of the research team that were crucial to obtaining both the physical samples and a complete characterization of the samples. Ahmed Bensaada, Laurent Isnard, Mario Beaudoin, Hugues Marchand, Zahia Bougrioua and Stephane Guillon have all made various contributions by growing samples and/or assisting with the growth of samples. Photoluminescence and optical absorption measurements at room temperature, low temperature and as a function of temperature were performed on the multi-quantum well samples by A. Ait-Ouali at the University of Montreal. The transmission electron micrographs, as well as the XRD data on several samples, were provided by Pat Desjardins, who also provided much needed advice on the structural characterization of strained layers. Mario Beaudoin provided a very useful computer program for calculating the energy levels in a strained-layer superlattice. Photoluminescence data for a large number of recent samples was provided by Stephane Guillon.

3 DETAILED BALANCE EFFICIENCY LIMIT IN QUANTUM WELL SOLAR CELLS

In a single bandgap solar cell, the open-circuit voltage (V_{oc}) and short-circuit current (I_{sc}) are coupled via the dark current relationship for a p-n junction diode. An approach using quantum wells proposed by Barnham and Duggan[1] relies on the possibility of decoupling V_{oc} and I_{sc} to allow a quasi-independent optimization of these factors. If this were possible, the detailed balance efficiency limit of quantum well solar cells would be greater than that of single bandgap cells. In experiments using $Al_{0.3}Ga_{0.7}As$/GaAs test structures and AlGaAs control samples, a significant enhancement of I_{sc} with only modest penalty in V_{oc} was reported,[2] corresponding to a conversion efficiency 1.1 times higher than the control. This chapter describes a brief theoretical analysis of the reported claims[1,2,3,4] that the presence of quantum wells in the depletion region may significantly enhance the detailed balance energy conversion efficiency limit over that of single bandgap devices.

To begin, we review the treatment of the detailed balance efficiency limit problem. The key background material for both single and multiple bandgap p-n junction photovoltaic devices is contained in the respective works of Shockley and Queisser[5] and Henry.[6] We consider a p-n junction photovoltaic device, maintained at a temperature of 0 K. Radiation is incident on the junction in all directions from a

surrounding black-body radiator of temperature T_c = 300 K. The junction may be considered as a negligibly thin slab of cross-sectional area, A, that absorbs all incident photons of $h\nu \geq E_g$ to generate electron-hole pairs that may thermalize and/or re-radiate. In equilibrium, the detailed balance principle states that each physical process and its inverse balance independently. This allows considering the fundamental absorption-radiative recombination process independently of all the other physical processes occurring in the material. We assume that incident photons of energy greater than the bandgap energy, $h\nu \geq E_g$, are absorbed and converted into photocharges that thermalize down to E_g. So, the energy of absorbed photons in excess of E_g is automatically lost via thermalization and photons of energy $h\nu < E_g$ do not participate. Absorption in the junction leads to a separation of the photocharges by the built-in electric field. Small piles of charge accumulate to create a non-zero open-circuit voltage condition at the terminals.

In order to calculate the limiting efficiency, we assume the radiative limit. Applying the detailed balance principle, each absorption event is balanced by a radiative recombination event. Therefore, the open-circuit voltage is a forward bias voltage such that the recombination rate it induces in the junction balances exactly the rate of photons being absorbed in the junction from the black-body field. The open-circuit voltage condition is equivalent to a short-circuit current condition whereby shorting the terminals together allows the small piles of photocharge generated in the junction to

contact each other directly and recombine via the short. If the junction were now maintained in thermal equilibrium with a surrounding black-body radiation field, absorption from the field would be the same and an equal recombination rate would be required to balance the photocharge generation. Thus, the absorption-recombination balance establishes the steady state dark current condition in the radiative limit for a p-n junction maintained at T_c. The dark current is simply the absorption rate of photons in the junction given by

$$F_{c0} = 2At_c Q(E_g, T_c) \tag{3-1}$$

where A is the cross-section area of the junction, the factor 2 is due to radiation/absorption on both sides of the slab, t_c is the probability that a photon absorbed will create a photocharge pair, and $Q(E_g, T_c)$ is the number of photons of energy $h\nu \geq E_g$ radiated from a black-body at $T = T_c$ obtained by integrating the Planck distribution to give

$$Q(E_g = h\nu_g, T_c) = \frac{2\pi}{c^2} \int_{\nu_g}^{\infty} \frac{\nu^2}{e^{\frac{h\nu}{k_B T_s}} - 1} d\nu \tag{3-2}$$

Next, we consider radiation from a black-body at, say, T_s = 6000 K that is incident on the p-n junction diode maintained at T_c = 300 K. The steady state continuity

condition for photons and photocharges leads to a balance of the generation and recombination rates described by

$$0 = F_s - F_c(V) - \frac{I}{q} \qquad (3\text{-}3)$$

where

$$F_s = A f_w t_s Q(E_g, T_s) \qquad (3\text{-}4)$$

is the generation rate in the junction due to the solar radiation incident on one side of the junction. Solar radiation is modelled by a black-body radiation spectrum with $T_s = 6000$ K. $f_w = 2.18 \times 10^{-5}$ is the geometric factor equal to the fraction of the solid angle subtended by the sun (a 1.39×10^6 km diameter object at a distance of 149×10^6 km). t_s is the probability that an absorption event creates a photocharge pair. $t_s = t_c = 1$ in the radiative limit.

$$F_c(V) = F_{c0} \frac{np}{n_i^2} = F_{c0} exp(V / kT_c) \qquad (3\text{-}5)$$

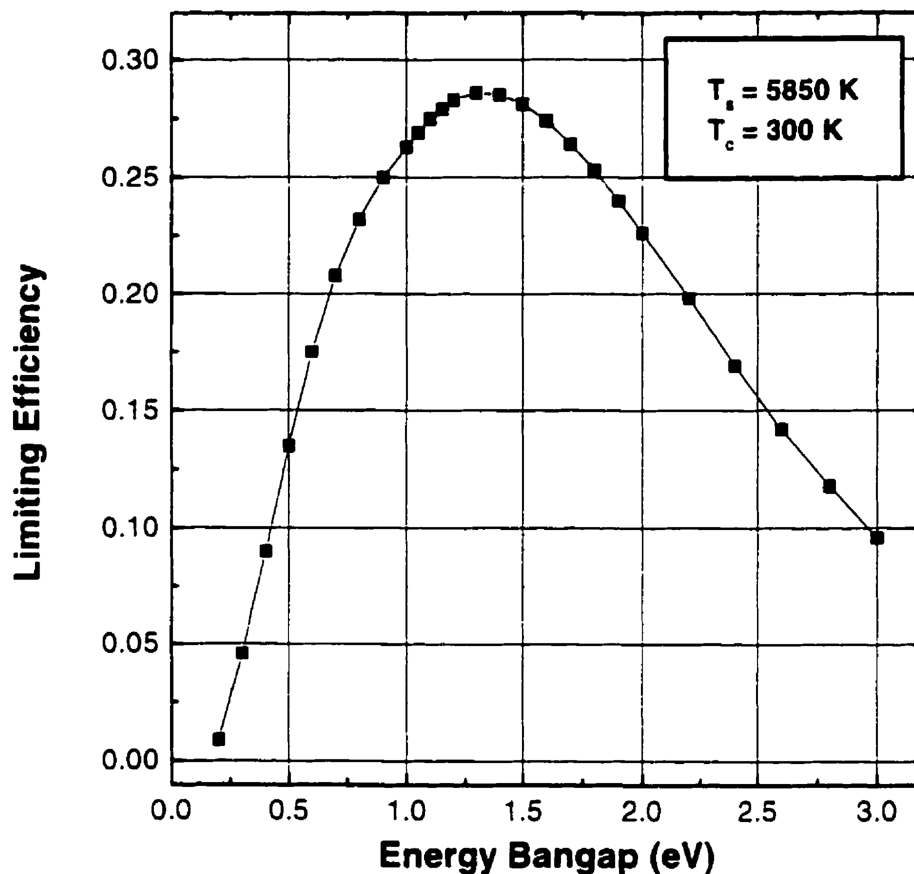

Figure 3.1 Detailed balance efficiency limit for a single bandgap p-n junction photovoltaic cell in equilibrium with a surrounding black-body radiation field at 300 K and receiving incident radiation from a 5850 K solar spectrum. These conditions are equivalent to air mass zero (AM0).

is the radiative recombination rate in the junction due to the forward bias V. I is the current flowing in a load connected to the terminals and q is the electronic charge.

(3-3) is the key expression that determines the current-voltage relationship for a cell as a function of the input variable set $\{E_g, T_s, T_c, f_w, t_s, t_c\}$. Since F_{c0} is negligibly small relative to F_s, $I_{sc} \sim qF_s$ and $V_{oc} \sim kT_c \ln (F_s/F_{c0})$. Non-radiative processes and other non-ideality factors may be modelled and included in (3-3), but we ignore them in the radiative limit. For any set of the input variables, we determine the maximum of the product $I \cdot V$ and divide it by the total incident power to obtain the detailed balance efficiency limit. For example, illumination at air mass zero (AM0) gives $f_w t_s Q(0, 6000) = 160$ mW/cm^2 or $f_w t_s Q(0, 5850) = 145$ mW/cm^2. Using $T_s = 5850$K and $T_c = 300$K generates the familiar limiting detailed balance efficiency versus E_g curve with a broad maximum near 1.35-1.40 eV. A plot of the efficiency limit as a function of E_g is shown in Figure 3.1 for $\{E_g, T_s, T_c, f_w, t_s, t_c\} = \{E_g, 5850 \text{ K}, 300 \text{ K}, 2.18 \times 10^{-5}, 1, 1\}$.

The main drawbacks of the single bandgap cell are two-fold. First, as we have already mentioned, all energy from absorbed photons in excess of the bandgap energy, E_g, is lost via thermalization. Second, radiation with energy $h\nu \leq E_g$ does not participate. These are the main reasons why the detailed balance efficiency limit is only ~ 30% and not higher. Multiple bandgap strategies and devices have been devised to 'scavenge' as much as possible of the remaining power from solar spectrum.[6] Quantum well photovoltaic cells are a variant of these multi-bandgap strategies. We may regard the quantum well system as a separate device that has been brought into thermal contact with the single bandgap cell, and the black-body field at T_c, while receiving illumination

from the black-body field at T_s. The addition of quantum wells is modelled by changing the terms F_s and $F_c(V)$. We make the following simple modifications. The contribution to the power developed at the terminals of the cell due to the additional absorption in the quantum wells is modelled by including an addition absorption term in (3-4) to give

$$F_s = Af_w t_s (Q(E_g, T_s) + t_{qw} Q'(E_{qw}, T_s)) \tag{3-6}$$

where t_{qw} is the probability of photocharge escape per unit time from the quantum well after an absorption event to participate in processes at the terminals, and

$$Q'(E_{qw}, T_c) = Q(E_{qw}, T_c) - Q(E_g, T_c) \tag{3-7}$$

is the additional absorption in the range below the principal bandgap energy and above the quantum well bandgap energy. The following analog for the dark current expression, (3-5), is used to model the radiative recombination rate.

$$F_c(V) = 2At_c(Q(E_g, T_c) + r_{qw} Q'(E_{qw}, T_c)) exp(\frac{V}{kT_c}) \tag{3-8}$$

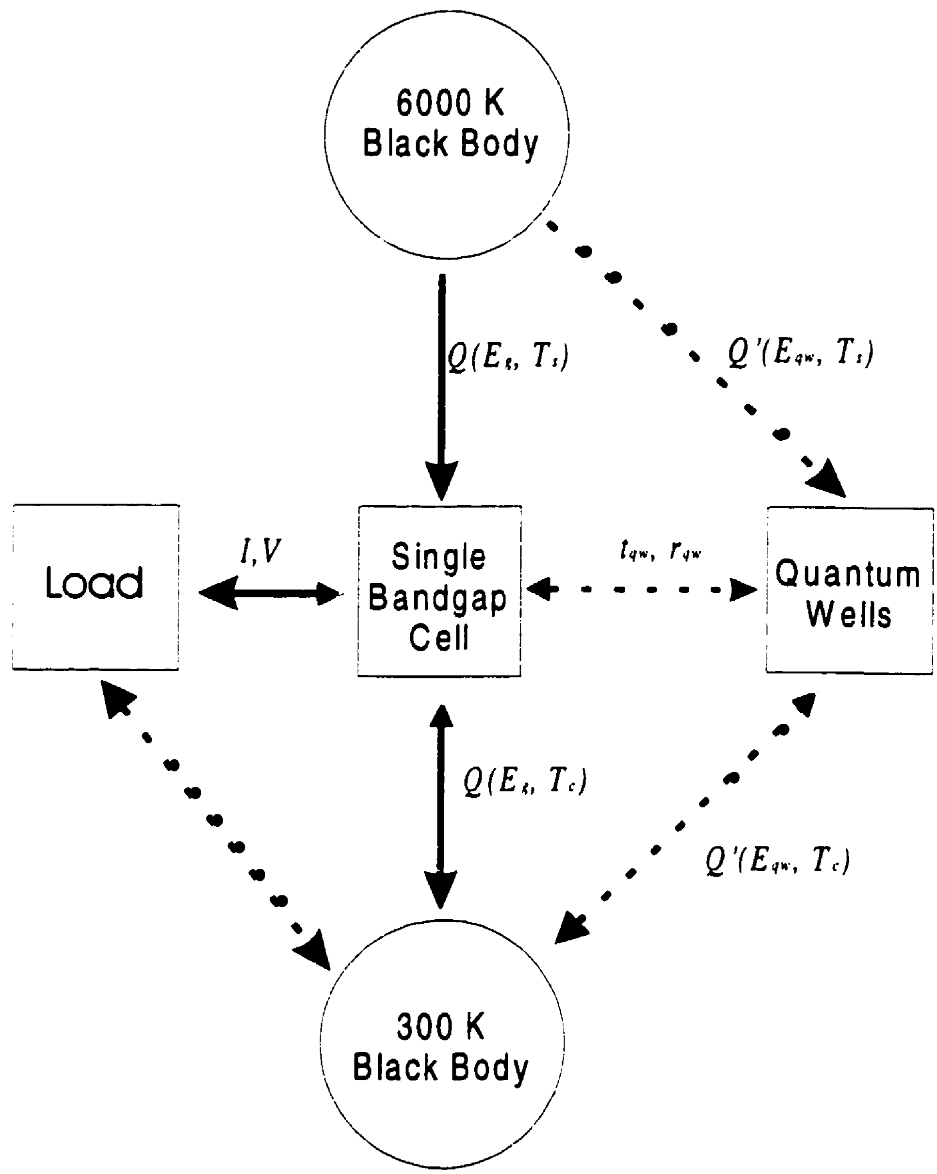

Figure 3.2 Schematic relationship between the main elements required to model the behavior of a quantum well solar cell. The cell with quantum wells can be considered a superposition of a single bandgap cell coupled to a system of quantum wells. $Q'(E_{qw}, T_s)$ and $Q'(E_{qw}, T_c)$ represent the respective contributions of the quantum wells to the generation and recombination rates in the cell. t_{qw} and r_{qw} are constants that describe the degree of coupling between the single band gap cell and the quantum wells.

where the quantity r_{qw} $Q'(E_{qw}, T_c)$ is the rate of photocharge thermalization down to the quantum well energy bandgap followed by a recombination event. The new elements are shown schematically in Figure 3.2. There will be an increase in I_{sc} due to the additional photon absorption in the quantum wells provided that some significant fraction of the photocharge generated in the quantum wells escapes into the barriers. At the same time, there will be a penalty in V_{oc} because the recombination is more efficient in the junction and a smaller forward bias voltage is required to balance the absorption process. The physical arguments of Barnham and Duggan[1], and Corkish and Green[4] contend that the $t_{qw}Q'(E_{qw}, T_s)$ term may significantly boost I_{sc} while the $r_{qw}Q'(E_{qw}, T_c)$ term leads to only a modest penalty in V_{oc}. Hence, these arguments require that $t_{qw} > r_{qw}$. Araujo and Marti[7] have raised the counterpoint that this violates the absorption-emission symmetry. They maintain that in equilibrium the absorptivity of a body must equal its emissivity ($t_{qw} = r_{qw}$) and a significant decoupling of V_{oc} and I_{sc} is not be possible. In practice, although admittedly lacking genuine rigor and using very crude absorption models, I found that it was possible to obtain results that support or discount the claims of enhanced efficiency by varying the model parameters for $t_{qw}Q'(E_{qw}, T_s)$ and $r_{qw}Q'(E_{qw}, T_c)$. However, it was possible to show using this very simple model, that any potential gains in conversion efficiency are small.

In a best case scenario $t_{qw} = 1$ and $r_{qw} = 0$. However, this is too unrealistic. Low temperature photocurrent data from Ref. 3 suggests that, even when the thermal energy

is well below the barrier height of the quantum well, photocarrier escape from the quantum wells can be extremely efficient in the presence of small electric fields such as the built-in field of the junction. So, there is some justification for making an *a priori* assumption that $t_{qw} = 1$. Equilibrium considerations require that the absorptivity and emissivity from the quantum wells balance at flat band. At the same time, the quantum efficiency of quantum well modulators and detectors increases with increasing reverse bias voltage. Hence, the efficiency of photocharge escape from quantum wells is an increasing function of the electric field and we require that r_{qw} be an increasing function of the forward bias voltage. Unfortunately, modelling of field-dependent absorption, emission and well-barrier charge transfer rapidly becomes unwieldy. This would be outside the scope of the present work.

A simplified approach is applied that remains computationally tractable and still allows us to obtain some important insights. Boundary conditions for r_{qw} are chosen so that $0 < r_{qw} < 1$ ($r_{qw} \sim 0$) when the junction field is maximal. This corresponds to the built-in field when $V = 0$. $r_{qw} = 1$ at flatband, where $V \approx qE_g$. r_{qw} is modelled using the following three different trial functions:

$$r_{qw}(V) = \frac{V}{qE_g} \qquad (3\text{-}9)$$

$$r_{qw}(V) = \left(\frac{V}{qE_g}\right)^2 \qquad (3\text{-}10)$$

$$r_{qw}(V) = e^{4\frac{V-qE_t}{qE_t}} \qquad (3\text{-}11)$$

Figure 3.3 illustrates the results of the efficiency limit calculation for 500 meV

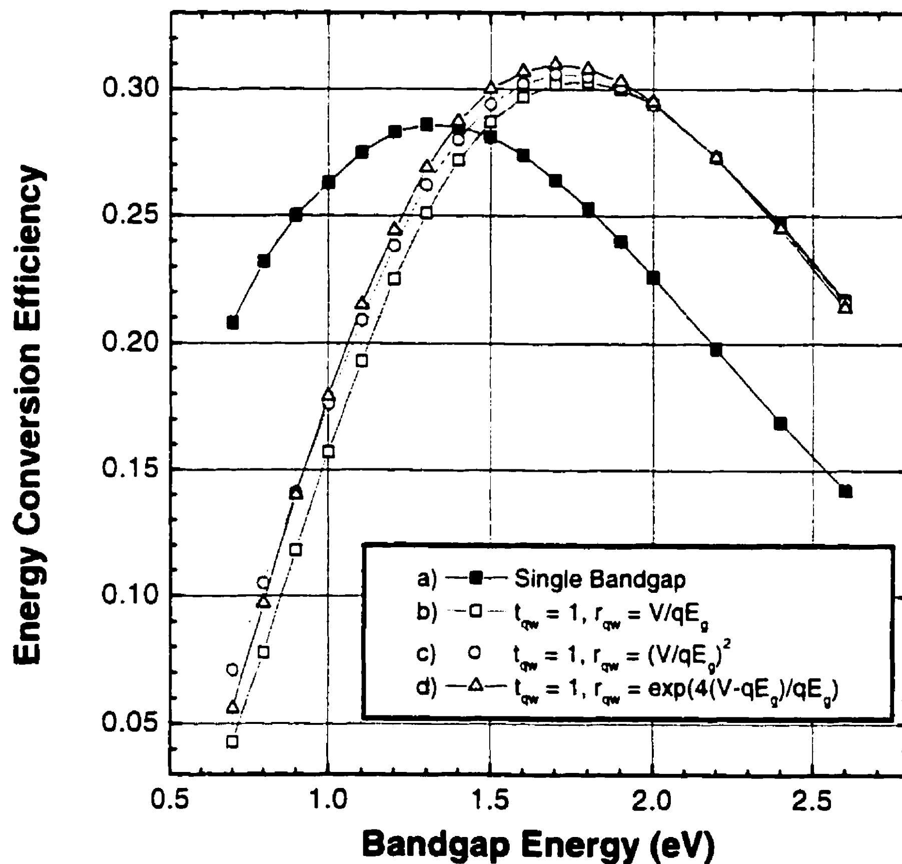

Figure 3.3 Calculated detailed balance efficiency limit as a function of energy bandgap for a) a single bandgap p-n solar cell and for b), c), d) solar cells with 500 meV deep quantum wells. t_{qw} and r_{qw} are coupling constants used to model the nature of photocharge transfer between quantum well and barrier.

deep quantum wells. The addition of quantum wells shifts the maximum efficiency bandgap energy towards the blue. This is fairly obvious since the addition of quantum wells boosts I_{sc} and reduces V_{oc}, as if a single bandgap cell with a smaller E_g had been substituted. So, the optimal bandgap energy for the barrier material in quantum well cells will be higher than that for a cell without quantum wells. Despite the fact that we have assumed the maximum efficiency for photocharge transfer from quantum well to barrier (t_{qw} = 1), the resulting improvements are not large. This indicates that the potential enhancements to the conversion efficiency using quantum wells, if they exist, are bound to be small (~ 10% relative improvement).

In Ref. 2, a 1.1 times improvement in the conversion efficiency for a quantum well $Al_{0.3}Ga_{0.7}As$/GaAs cell relative to a single bandgap $Al_{0.3}Ga_{0.7}As$ cell was measured using a suboptimal cell design. It was then proposed that it would be possible to further enhance the gain with an improved cell design. However, there are two very important points that have been neglected in the conclusions of Refs. 2 and 3.

1. For solar illumination that may be modelled by the emission spectrum of a 5850-6000 K black body, the maximum in the detailed balance efficiency limit occurs at ~ 1.35-1.40 eV depending on whether it is AM0, AM1.5, etc. Because of this, a single bandgap $Al_{0.3}Ga_{0.7}As$ (E_g ~ 1.78 eV) control sample is clearly not optimal (see Figure 3.1). The addition of GaAs quantum wells is fully expected to improve the

conversion efficiency. In fact, a single bandgap GaAs (1.42 eV) cell would have demonstrated a more significant improvement over the $Al_{0.3}Ga_{0.7}As$ control cell. A single bandgap GaAs cell should have been the control sample for this experiment. Another acceptable alternative would be to use InP (1.34 eV) single bandgap cells as control samples with InGaAs(P)/InP quantum well test cells since 1.34 eV is close to the maximum efficiency for a single bandgap cell.

2. The conversion efficiency with quantum wells is 1.1 times the efficiency of the control. The experiment was performed with p-i-n photodiode devices that are suboptimal for photovoltaic energy conversion. However, there is a good reason to expect that this improvement will not scale when passing to more optimal structures. The samples (see Refs. 2 and 8 for detailed sample listings and current-voltage plots) used in the study are suboptimal because the p-doped emitter layers are quite thick (300nm). In contrast, GaAs and InP solar cells are designed to have minimum emitter thickness (normally 30 - 100 nm). The thick emitters in the samples of Ref. 2 significantly attenuate the power of the signal due to absorption in the barriers while allowing the quantum well signal to pass and are responsible for the very low current densities achieved (~1mA/cm^2). The thicker the emitter, the bigger the difference in I_{sc} that will be measured between a single bandgap control sample and a test sample with quantum wells. Thinning the emitter to achieve a better solar cell will have the effect of increasing the signal due to barrier absorption while leaving

the quantum well signal unchanged. Hence, the relative enhancement of I_{sc} in samples with thin emitters (<100 nm) will be significantly diminished. For example, the 10% I_{sc} boost applies to only a total current density of ~ 1 mA/cm^2. This gives only a ~ 0.1 mA/cm^2 boost, whereas properly designed single bandgap GaAs and InP cells normally achieve ~ 30 mA/cm^2.

Still, a theoretical basis for these enhancements has not been entirely discounted and we may continue to consider how the proposed strategy could work. For example:

1. The process of carrier escape and capture is not symmetric in the presence of an electric field. We need to investigate the nature of this asymmetry for small fields (typically ~ 1.5 V / 3 μm = 5 kV/cm).
2. The energy of photons absorbed in excess of E_g is considered to be lost via thermalization of the photocharges. This energy is then transferred back to the surroundings and does not contribute to the photovoltaic effect. The presence of the quantum wells may provide mechanisms for recovering some of this lattice energy to be 'recycled' for thermally-assisted escape of photocarriers from the quantum wells The principal counterpoint to this possibility is that the presence of quantum wells allows for the possibility of further thermalization losses as carriers fall into the wells.

From a thermodynamic perspective, a photovoltaic cell can be regarded as a device that transfers energy from bodies maintained at different temperatures (6000K and 300K). A single bandgap cell represents a set of physical mechanisms whereby the energy flows from the high temperature body to the low temperature body and a fraction of the energy flow may be converted to useful work. Conceptually, a quantum well cell represents the set of mechanisms due to the single bandgap cell plus an additional set. Using this formulation, detailed entropy arguments could perhaps resolve whether it is possible to enhance the limiting efficiency with the quantum well cell.

In conclusion, a simple model of quantum well interaction with a single bandgap cell has been developed. With the aid of this model, a careful analysis of the available experimental data shows that efficiency enhancements, if they exist, are small. Therefore, the quantum well solar cell, as it has been proposed in Refs. 1 - 3, is not a practical method for achieving substantial gains in solar energy conversion efficiency.

4 STRAIN AND RELAXATION IN MULTIPLE QUANTUM WELL STACKS

This chapter describes an experiment carried out to investigate the effects of strain and strain relaxation on a series of multiple quantum well p-i-n photodiodes. The work was submitted to and published in the Journal of Applied Physics. My contribution to the work includes: design of the experiment and of the epitaxial layers in collaboration with Ahmed Bensaada, modest participation in the growth of the samples, acquisition and analysis of the XRD data for the experiment, fabrication of the photodiode structures, acquisition and analysis of the field-dependent photocurrent data, determination of the quantum well and band alignment parameters from the available data using the computer program provided by Mario Beaudoin, analysis of the quantum-confined Stark effect and I was responsable for writing the manuscript.

4.1 *Strain and relaxation effects in InAsP/InP multiple quantum well optical modulator devices grown by metal-organic vapor phase epitaxy*

by R. Y.-F. Yip, A. Aït-Ouali, A. Bensaada, P. Desjardins, M. Beaudoin, L. Isnard, J.L. Brebner, J.F. Currie and R. A. Masut.

Groupe de recherche en physique et technologie des couches minces (GCM)

Département de génie physique, École Polytechnique de Montréal, et

Département de physique, Université de Montréal

C.P. 6079, succ. "Centre-Ville", Montréal QC, Canada H3C 3A7

Submitted to the Journal of Applied Physics on August 26, 1996

Accepted for publication on November 7, 1996.

J. Appl. Phys. ***81****, 1905 (1997)*

ABSTRACT

Strained-layer multiple quantum well (MQW) InAsP/InP optical modulators have been fabricated from layers grown by metalorganic vapor phase epitaxy. The devices are a series of p-i(MQW)-n photodiodes in which the active core regions consist nominally of 25 periods of 10 nm InAsP quantum wells of 4.4%, 10.0%, 15.6% and 26.4% As composition separated by 10 nm InP barriers. Structural parameters for the samples were obtained using high-resolution x-ray diffraction rocking curves and transmission electron microscopy. The series contains samples with both coherently strained and partially relaxed multi-layers, where the relaxation is characterized by misfit dislocations. The band offsets for the heterostructures were determined by fitting the energy positions of the optical absorption peaks with those computed using the Marzin—Bastard model for strained-layer superlattices [as in M. Beaudoin *et al.*, Phys. Rev. B **53,** 1990 (1996)]. The conduction band discontinuities thus obtained are linear in the As composition (7.56 ± 0.08 meV per As % in the InAsP layer) at low and room temperature for As concentrations up to 39%, and up to 17% average relaxation. Comparisons between the coherently strained and partially relaxed samples demonstrated a broadening of optical transition linewidths due to relaxation which appears to be of minor consequence for optical modulator devices as the essential optical and electrical properties remain intact. The electric field-dependent red-shift of

the n = 1 electron-heavy hole transition was measured by a photocurrent method and found to be enhanced in structures with lower barrier heights.

I. INTRODUCTION

The growth of alloy semiconductor thin films to create the desired energy band structure for a device application often involves strained-layer epitaxy. In the case of III-V semiconductor lasers, the benefits of strain-induced modifications to the valence band structure of the material are widely recognized[1,2,3,4]. Device designs seek to maximize these benefits by introducing the largest possible strains without compromising the integrity of the crystal. But, it is difficult to avoid introducing at least some misfit dislocations into the device layers. In large lattice mismatch heteroepitaxy, misfit dislocation networks (MDNs) are deliberately introduced via buffer layers to relieve stress in the layers and control the relaxation process[5,6,7,8,9]. Dislocations resulting from relaxation are therefore present in many strained-layer devices and studying how they may affect overall device performance is of prime importance. For example, the dislocations in the active layers of semiconductor lasers are efficient non-radiative recombination centers and play a role in both rapid and gradual degradation processes[10,11,12,13]. In transistors and transport devices, dislocations act as effective scattering potentials and introduce deep trap states[14,15] with deleterious effects on the

electronic mobility and high frequency operation. Very low defect densities in the active layers of these devices are usually catastrophic for both performance and reliability.

p-i-n photodiode devices appear not to be as seriously affected by the presence of moderate MDN densities in their layer structures. This is mostly due to two factors. First, relaxation and stress relief in strained systems can proceed principally via the formation of MDNs near the interfaces bordering a strained layer[15,16]. In this case, there can be few dislocations threading through the core section of the strain layer or superlattice forming the main light absorbing region of a photodiode and good optical absorption characteristics are preserved. Secondly, both the photonic and electrical power densities in these devices are usually very low so that little energy is available to perturb the defect states and drive further plastic relaxation of the crystal. Relaxed layers have previously been used to fabricate InAsP/InP multi-quantum well (MQW) p-i-n optical modulators[17,18] based on the quantum-confined Stark effect[19] (QCSE), where the InAsP grown on InP is compressively strained with a mismatch of up to 3.23%. The structural and optical properties of InAsP/InP multi-quantum well structures (MQWSs) have also been studied using high resolution x-ray diffraction (HRXRD) and transmission electron microscopy (TEM) to characterize both coherently strained and relaxed structures[20,21]; in which, the Marzin—Bastard envelope function formalism[22] was used to fit the optical absorption transition peaks to the quantum well energy levels. These structural studies confirmed that the relaxation in this system for moderate strains

does indeed proceed via the generation of MDNs localized at the interfaces bordering the InAsP/InP MQWS. Thus, the MQW optical modulator in the InAsP/InP strained-layer system is a good candidate with which to study some of the effects of relaxation on device performance. In this paper, we present structural and optical characterizations of a series of InAsP/InP MQW layers and optical modulator devices which were fabricated with these layers. The As compositions and MQW layer thicknesses in the series were chosen to give samples with increasing degrees of relaxation. The operation of these devices appears not to be significantly affected by the presence of relaxation and we argue that the QCSE modulator may be an example of a device where strain relaxation and dislocations do not seriously affect the high frequency operation.

II. EXPERIMENT

The epitaxial layers for this study were prepared by low-pressure metalorganic vapor phase epitaxy (LP-MOVPE) using trimethyl-indium, tertiarybutyl-arsine and phosphine precursors, and doped with diethyl-zinc and silane. The epilayer growth on S-doped (~2×10^{18} cm^{-3}) InP (001) substrates was carried out using Pd-purified H_2 as a carrier gas and with a substrate temperature of 600 °C, a reactor pressure of 40 Torr and a total gas flow rate of 2880 sccm[23]. We estimate that the flow velocity at the substrate under these conditions is 60 cm/s. The nominal layer and device structure for the samples is shown in Figure 4.1 and detailed in Table 4-I. mod03, mod04, mod05,

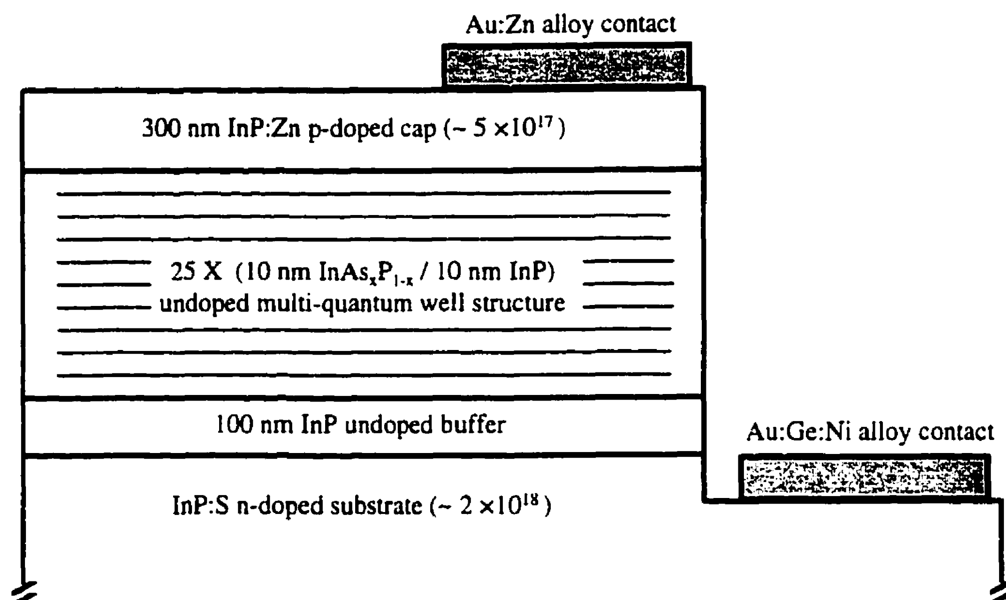

Figure 4.1 Nominal layer and device structure for p-i(multi-quantum-well)-n optical modulators.

mod06 and mod07 were grown in a single series and the devices were fabricated in a single batch. mod07 is a control sample identical to the other samples in the series but with the MQWS replaced by a single uninterrupted section of undoped InP. mod02 was produced in a different run using the same growth parameters but differs from the others in the thicknesses and number of its constituent layers[24]. However, it has been extensively characterized by TEM, HRXRD and optical absorption and many of its structural characteristics have been precisely determined[21]. It serves as an important reference and is included in the current discussion.

Table 4-I. Sample listing and structural parameters obtained from high-resolution (115+/115-) and (004) XRD scans. Using mismatches measured with respect to InP, the fully relaxed, free-standing lattice parameter of the InAsP quantum well sections was deduced from a knowledge of the lattice parameters for the strain-distorted unit cell. This was subsequently used to compute the As composition of the wells, biaxial well strain and relaxation (R). h/hc is the ratio of the multi-layer structure thickness to the Matthews—Blakeslee critical limit for a layer of the average composition.

Sample	**Multi-layer structure**		**Critical limit**	**In-plane mismatch**		**Biaxial strain in wells**		R	
	multi-quantum well structure	cap layer	h/hc	$[110]$	$[\bar{1}10]$	$[110]$	$[\bar{1}10]$	$[110]$	$[\bar{1}10]$
mod07	500 nm InP	300 nm	-	-	-	-	-	-	-
mod03	25 X (9.4 nm $InAs_{0.044}P_{0.956}$/ 9.4 nm InP)	280 nm	1.9	< 0.001%		-0.14%		< 1%	
mod05	25 X (9.8 nm $InAs_{0.100}P_{0.900}$/ 9.8 nm InP)	290 nm	5.2	< 0.001%		-0.31%		< 1%	
mod06	25 X (10.3 nm $InAs_{0.156}P_{0.844}$/ 10.3 nm InP)	310 nm	9.3	0.012%	0.003%	-0.49%		5%	1%
mod04	25 X (9.8 nm $InAs_{0.264}P_{0.736}$/ 9.8nm InP)	290 nm	17	0.079%	0.034%	-0.77%	-0.81%	20%	9%
mod02	50 X (11.9 nm $InAs_{0.135}P_{0.865}$/ 11.9 nm InP)	1550 nm	18	0.050%	0.024%	-0.38%	-0.41%	23%	11%

Both symmetric (004) and asymmetric (115+/115-) HRXRD rocking curves for the samples were acquired using a Cu-Kα_1 x-ray source and a Philips four-crystal diffractometer with the monochromator aligned to Ge(220). TEM samples with <110> surface normals were prepared by mechanical polishing followed by low-angle (4°) Ar^+ ion milling at 5 keV. The ion energy was gradually reduced to 2.5 keV during the final stages of thinning to reduce damage. The cross-sectional observations were made with a Philips CM30 microscope operated at 300 kV. Optical absorption spectra from 8 K up to room temperature were measured for the as-grown epitaxial layers using a free-flow, He-circulating cryostat with optical ports and a BOMEM DA3 Fourier transform interferometric spectrometer with a quartz halogen broad-spectrum source and Ge photodetector.

Following the material characterization steps, photolithographically defined circular device isolation mesas with diameters ranging from 100 μm to 800 μm were formed by etching through the epitaxial layers down to the substrate in a solution of $HCl:CH_3COOH:H_2O_2$[25]. Lift-off photolithography was used to pattern 200 nm thick layers of thermally evaporated Au-12% wt. Ge alloy metal onto the n-InP substrate and Au-10% wt..Zn alloy metal onto the p-doped cap. The samples were subjected to a single flash anneal cycle of 2 s at 300 °C to improve the contact resistivity.

In forward bias, turn-on voltages for the diodes ranged from 0.7 V to 1.0 V. Reverse-bias behavior varied from avalanche breakdown starting near -6 V up to Zener breakdown in excess of -15 V. Room temperature measurements of the electric field-induced Stark shift of the quantum well optical transitions were performed by detecting the photocurrent response of the diodes as a function of reverse bias voltage using a tungsten lamp source, 0.1 m scanning monochromator and lock-in amplifier. Temperature-dependent photocurrent spectra from 295 K down to 11 K were also measured for mod02, where the sample was attached to a copper cold-finger mount and placed in a close cycle He-cooled cryostat with appropriate optical access ports.

III. RESULTS

A. Structural characterization

The HRXRD results are summarized in Table 4-I and typical (004) rocking curves for the samples are displayed in Figure 4.2. The HRXRD data were analyzed with a combination of computer simulations of the rocking curves using dynamical diffraction theory[26] and some formal calculations. Details of the HRXRD analysis used can be found in Refs. 27, 28, 29 and 30. The three orthogonal components ($[001]$, $[1\bar{1}0]$, and $[110]$) of the average MQWS mismatch with respect to InP, as defined by

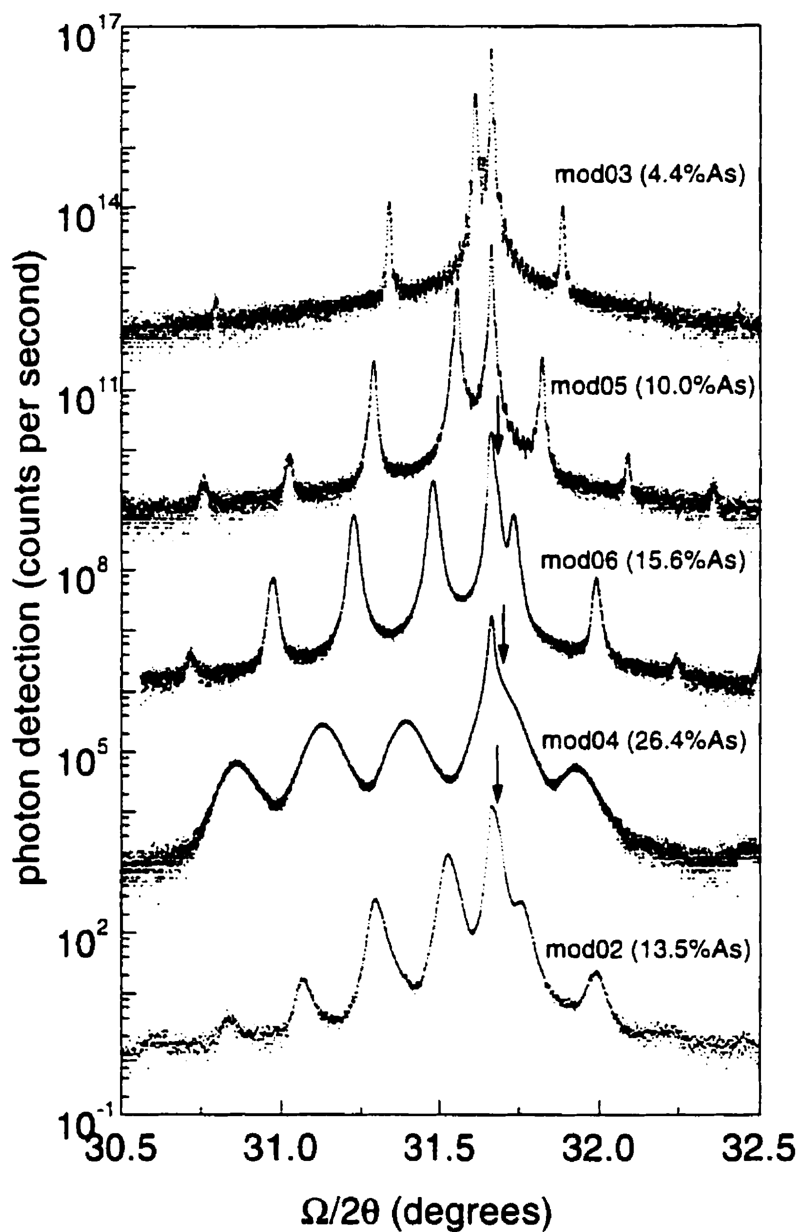

Figure 4.2 Symmetric (004) reflection high-resolution x-ray diffraction rocking curves. The arrows indicate the approximate positions of separate peaks due to tensilely-strained InP material in the samples where plastic relaxation has been detected (see Table 4-I).

$$\frac{\Delta a}{a} = \frac{a_{InAsP} - a_{InP}}{a_{InP}} \tag{4-1}$$

were determined from relative displacements of the zero order MQWS peaks with respect to the InP substrate peak in the HRXRD spectra. These mismatches gave the $[001]$, $[1\bar{1}0]$, and $[110]$ lattice constants for the strain-distorted unit cell; from which the lattice constant of the free-standing, fully relaxed unit cell, a_{free}, for the MQWS was recovered assuming a tetragonal distortion due to biaxial strain in the (001) plane. The average As composition of the MQWS was then obtained from a_{free} by linear interpolation (Vegard's law) between the lattice constants of InAs and InP. Finally, from a knowledge of the lattice constants of the free-standing and distorted cubic cells, the biaxial strain in both wells and barriers was determined. For samples with plastic relaxation, the tensile strain in the barriers and cap layers is by definition the in-plane mismatch.

The ratios of the total MQWS thicknesses to their corresponding critical limits[31,32] for the formation of misfit dislocations has also been calculated and listed in Table 4-I by considering the MQWS as single epitaxial layer of its average composition grown on a thick substrate. The relaxation, R, was computed using

$$R = \frac{a_{//} - a_{InP}}{a_{free} - a_{InP}} \tag{4-2}$$

where $a_{//}$ is one of the in-plane lattice constants.

We did not detect any relaxation in mod03 (1.9 hc) and mod05 (5.2 hc) and consider them to be coherently strained. However, the Matthews and Blakeslee critical limits for the generation of misfit dislocations in equilibrium structures have been exceeded so these are metastable structures and a very low density of misfit dislocations is possibly present in the two samples. mod06 (9.3 hc) is slightly-relaxed and likely has a low density MDN at the MQWS/buffer interface. mod04 (17 hc) and mod02 (18 hc) show very clear evidence of plastic relaxation. The TEM micrographs for mod04 (shown in Figure 4.3) and mod02 (shown in Ref. 21) confirmed the presence of MDNs at the MQWS/buffer and MQWS/cap interfaces. The relaxation is anisotropic (see Table 4-I) and has proceeded first via the generation of misfit dislocation lines parallel to $[1\bar{1}0]$ followed eventually by the same process along [110][33].

The relaxation can also be observed qualitatively in the evolution of the symmetric (004) rocking curves of Figure 4.2. The spectra for mod03 and mod05 show sharp, intense peaks with the presence of finite thickness fringes, indicative of good layer perfection. The loss of such thickness fringes would be a good first indication of the

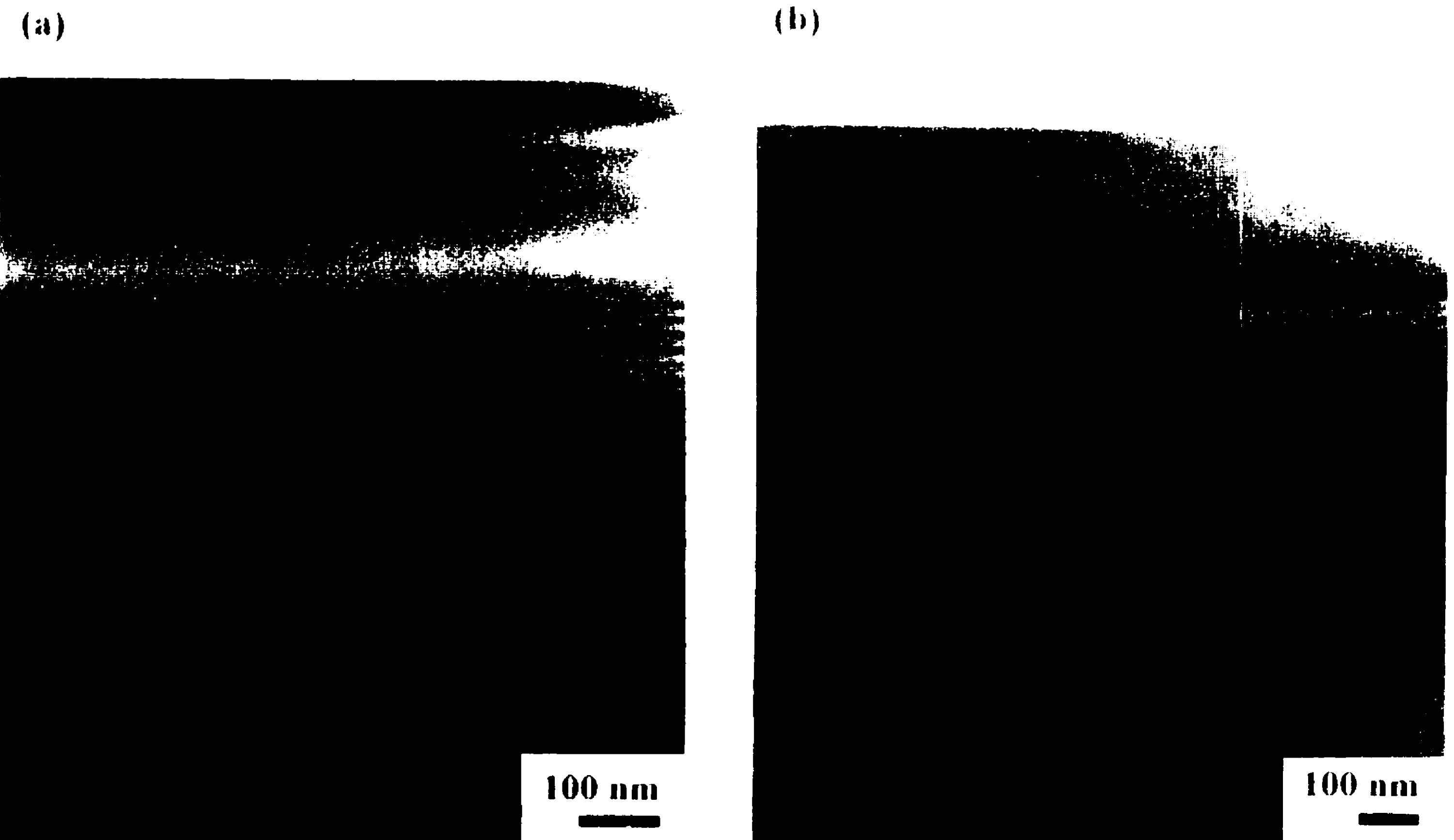

Figure 4.3 Transmission electron microscopy bright-field images of mod04: (a) $g = (002)$, and (b) $g = (2\bar{2}0)$.

presence of misfit dislocations.[30] The diffraction peaks for mod06 have a similar form to those of the coherently strained samples but the thickness fringes have disappeared and a slight broadening is detectable indicating that significant numbers of defects are just beginning to be introduced into the crystal at this strain energy. Dislocations distort the diffracting Bragg planes and cause broadening of the diffraction peaks.[28] The broadening that increases in the mod04 and mod02 peaks is due to their higher MDN densities. A small shoulder to the right of the substrate peak, indicated by the arrows, is perceptible in the spectra of mod06, mod04 and mod02. This corresponds to the signal from the InP material in the barriers and cap layer that is in tensile strain as a result of the plastic relaxation. These peaks shift to the right with increasing tensile strain as the in-plane mismatch increases. Note that the first order satellite peak of the MQWS in the mod04 spectrum is predicted to be nearly coincident with the substrate signal (the geometric mean of the zeroeth order and second order peaks). This indicates that the feature to the right of the substrate is largely due to the tensile-strained barriers and cap layer. In mod02, the shoulder remains closer to the substrate signal than in mod04 because the relaxation of the cap layer away from the MQWS is greater. The resolution in Figure 4.2 does not allow a precise determination but HRXRD scans using the diffractometer in its triple-axis mode with an additional analyzer at the detector confirmed the presence of separate substrate and tensilely-strained InP peaks. The triple-axis measurements and TEM micrographs also showed that the MQWS/cap relaxation is more severe in mod02 than in mod04.

B. Optical absorption

The optical absorption spectra at 8 K and 295 K are displayed in Figure 4.4. These spectra are well-complemented by photoluminescence measurements that have also been performed on these samples and will be presented elsewhere[34]. Here, we focus the discussion exclusively on the behavior of the n = 1 electron-heavy hole (e1-hh1) and electron-light hole (e1-lh1) band-edge transitions. The excitonic features associated with these optical transitions are identified with arrows and the absorption curves are displayed in the dimensionless units of the absorption coefficient, α, times the interaction length, d. For reference, the absorption coefficient due to the e1-hh1 transition in sample mod04, after normalizing to the total width of quantum well material, is ~24000 cm^{-1} at 8 K and ~11000 cm^{-1} at 295 K. Higher order transitions, such as those associated with the n = 2 levels, are visible in most of the spectra and excitons associated with the InP band edge (~1.424 eV) are also well-resolved at 8 K. Notice that these latter excitons are slightly red-shifted in the mod06 (15.6% As) and mod04 (26.4% As) spectra due to the relaxation-induced tensile strain in the InP barrier and cap sections. There is significant relaxation in mod02 as well but the red-shifting is less evident because mod02 contains a much thicker InP buffer that is coherent with the substrate, and a thick cap that has relaxed away from the MQWS. mod02 (13.5% As) also contains ~2.4 times more quantum well material than the other samples; hence the

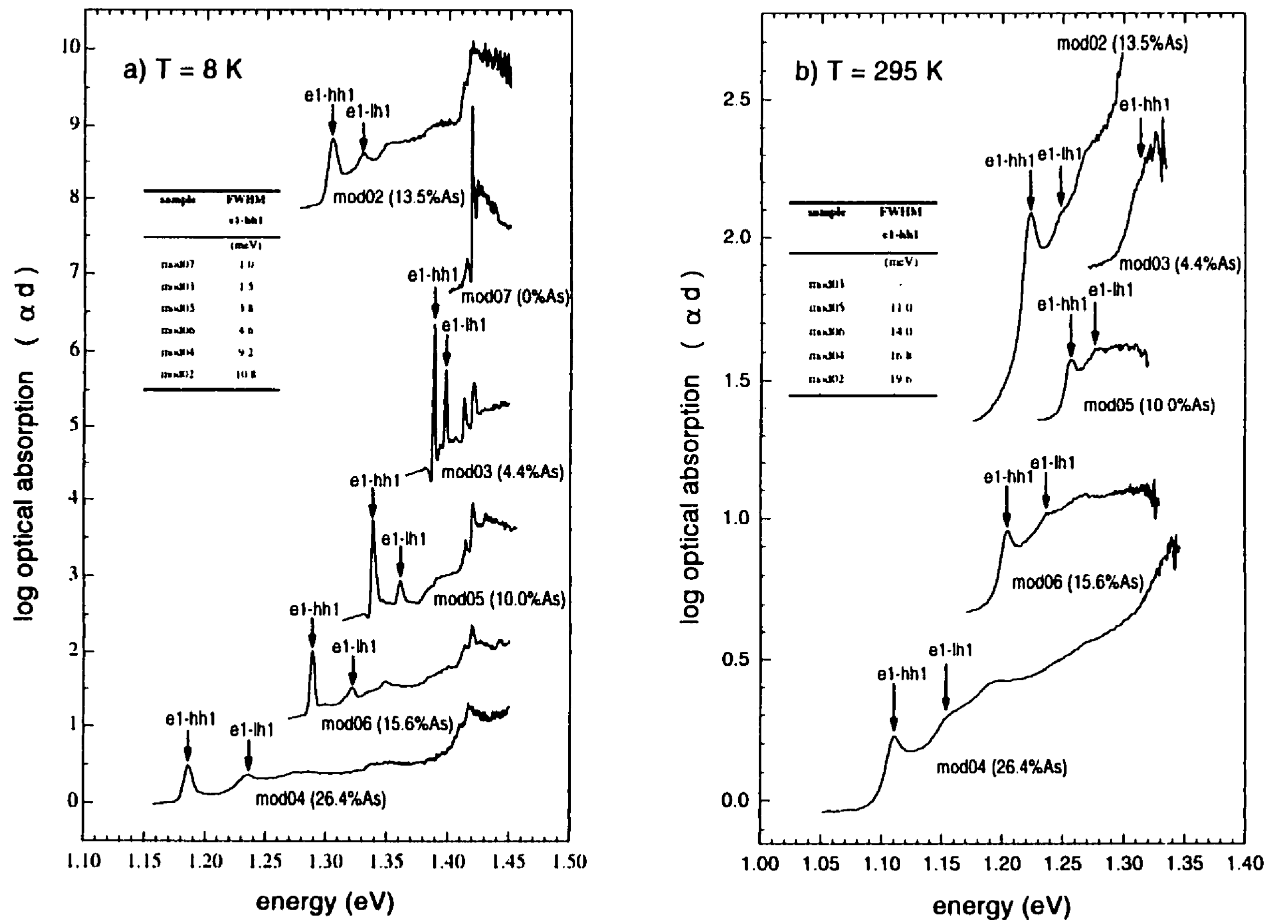

Figure 4.4 Absolute optical absorption spectra for the as-grown epitaxial layers listed in Table I at a) T = 8 K and b) T = 295 K. The n = 1 electron-heavy hole (e1-hh1) and electron-light hole (e1-lh1) transitions are identified with arrows. The full width half maxima (FWHM) at T = 8 K and at T = 295 K for the e1-hh1 transitions are summarized in the inset tables.

sharper appearance of the mod02 absorption features relative to the other samples at 295 K is mostly a scaling effect.

In mod03 (4.4% As), the n = 1 electronic level is only ~18 meV below the barrier level, and therefore less than the thermal energy at 295 K. Despite this, we had expected an excitonic feature to be clearly resolvable at 295 K because room-temperature excitonic features have been observed in shallow GaAs/AlGaAs MQWSs[35]. The lack of a clear excitonic feature at room-temperature for mod03 is due to the strain splitting of the hh1 and lh1 valence band levels. As a result, the mod03 absorption spectrum at 295 K comprises two broad excitonic features separated by only ~9 meV.

Using the summary of absorption linewidths (see inset tables in Figure 4.4) as a guide to study the absorption spectra, we attribute the linewidth broadening trends to three main factors: temperature, alloy disordering and relaxation. Temperature broadening effects add from 3.6 to 4.7 meV to the half widths and can be explained by LO phonon scattering of the excitons[36,37]. We attribute the broadening trend in the low temperature spectra for the samples without relaxation, mod07 (0% As), mod03 (4.4% As) and mod05 (10.0% As), to alloy disordering. This is an important effect as the linewidths increase rapidly with the As fraction. Unfortunately, it is difficult to discern clearly a broadening trend due to relaxation from that of alloy disorder in the subsequent

samples mod06 (15.6% As), mod04 (26.4% As) and mod02 (13.5% As), because both increase with the As fraction.

A precise determination of the barrier heights and quantum well transition energy levels was made using the Marzin—Bastard envelope function model[22,38] and the structural and optical absorption data. Details of the calculation method and procedure can be found in Refs. 20, 21 and 22. First, the structural parameters of the preceding section were used as inputs in the model, considering the average value of the $[1\bar{1}0]$ and [110] relaxation. From this, the model predicted the optical transitions for the samples for a given specification of the heterostructure conduction band offset, δE_C. Next, the excitonic binding energies and red-shift due to the built-in field had to be accounted for independently. Accordingly, nominal windows of 9 ± 3 meV and 6 ± 3 meV (the reduced mass of the e1-hh1 system is ~1.5 times that of the e1-lh1 system) were assigned for the binding energies of the hh and lh excitons, respectively. The red-shift of the e1-hh1 and e1-lh1 transitions for mod03, mod05, mod06 and mod04 due to the built-in field of ~17 kV/cm was estimated to be ~1 meV (see next section). The red-shift in mod02 was negligible because its undoped section is ~3.2 times thicker than that of the other samples, giving a built-in field of only ~5 kV/cm. Finally, an optimal fit to the measured optical transitions was obtained by sweeping δE_C.

In Figure 4.5, the results for δE_C corresponding to the best fits are plotted against the As fraction in the InAsP quantum wells. All the points from Refs. 20 and 21 have been plotted along with those obtained in the current study. The plot of Figure 4.5 represents 20 band offset fits performed at 8 K and at room temperature on 11 InAsP/InP MQWSs. The 11 MQWSs span a range of As fractions from 4.4% to 38.9%; of which 7

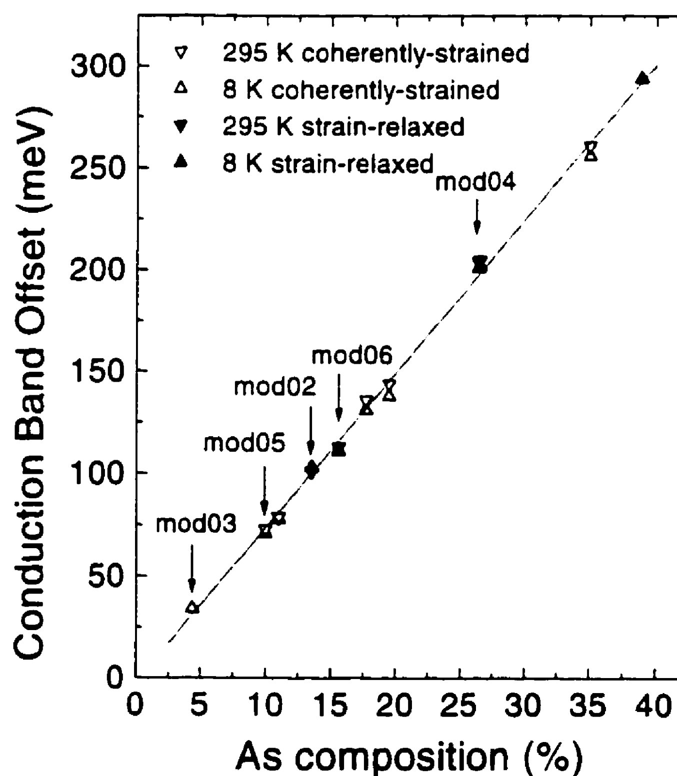

Figure 4.5 Dependence of the absolute conduction band discontinuity, δE_C (meV), on the As composition, x, of the $InAs_xP_{1-x}$ quantum wells. The data points corresponding to samples in the current study are identified with arrows. The other points correspond to samples in Refs. 20 and 21. The linear least squares fit of the all the data points gives a slope of 7.56 ± 0.08 meV/As%.

structures are coherently strained and 4 structures have varying degrees of plastic relaxation. We observe that δE_C has a simple linear dependence on the As fraction (7.56 $\pm$ 0.08 meV/As%). In terms of the relative band offset, δE_C represents 75.8 $\pm$ 2.7 % of the total strained band gap difference δE_g. This linear dependence is consistent with the

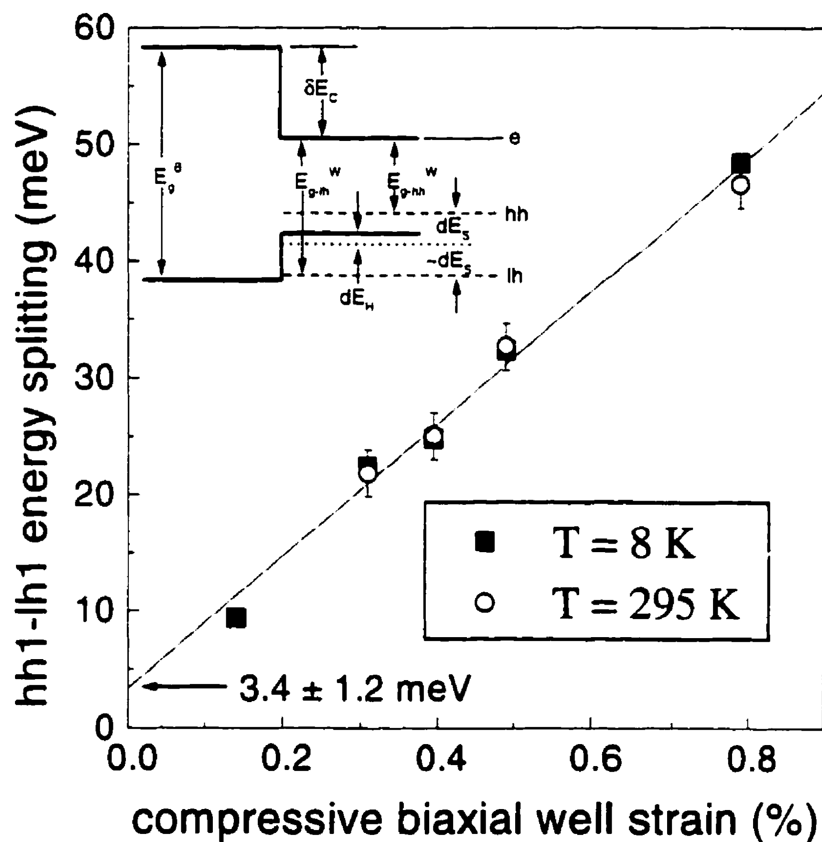

Figure 4.6 Dependence of the n = 1 electron-heavy hole (e1-hh1) and electron-light hole (e1-lh1) transition energy difference, as measured by optical absorption (Figure 4.4), on the compressive biaxial strain in the InAsP quantum wells, as measured by x-ray diffraction (Table 4-I). The inset diagram (top left) illustrates the modification of the quantum well band gap due to compressive strain.

predictions of the quantum dipole model of Tersoff.[20,39]

An internal consistency check for the general accuracy of this analysis was performed. In Figure 4.6, the difference between the e1-lh1 and e1-hh1 optical transition energies, as measured by optical absorption, is plotted against the compressive biaxial strain in the InAsP quantum wells determined from the structural characterization by HRXRD. The inset in Figure 4.6 illustrates the strain-induced modifications to the well and barrier band gaps described by the strain Hamiltonian of Pikus and Bir[40]. Biaxial strain in the InAsP quantum wells introduces two general modifications to the band gap. First, the entire valence band structure is displaced relative to the conduction band by the hydrostatic deformation of the crystal. Then, the hh and lh bands are split by the shear deformation of the crystal. The case illustrated in the diagram is for coherent, compressive strain in the InAsP quantum wells. Any relaxation of the MQWS away from the substrate would introduce similar modifications to the InP barrier due to tensile strain. The influence of the strain anisotropy in the relaxed samples is negligible[21,41] and the average of the $[1\bar{1}0]$ and [110] strains has been used. For small strains, the hh1-lh1 energy splitting induced by the shear term should have a nearly linear dependence on the biaxial well strain[42]. Therefore, we expect the hh1-lh1 energy difference to consist of a linear term due to the biaxial strain and an approximately constant term due to the binding energy difference between heavy and light hole excitons. The plot of Figure 4.6 affirms this and the linear least squares

estimate for the intercept of 3.4 ± 1.2 meV is in agreement with our previous assumptions about the exciton binding energies.

C. Quantum-confined Stark effect (QCSE)

The photocurrent response of mod05 (10.0% As), mod06 (15.6% As), mod04 (26.4% As) at room temperature and of mod02 (13.5% As) at 11 K as a function of reverse bias voltage is displayed in Figure 4.7. mod03 has not been included because thermal broadening makes it impossible to accurately determine the position of the e1-hh1 transition at room temperature. Using the photocurrent spectra and the optical absorption spectra, we estimated the electric field-induced red-shift of the e1-hh1 optical transition and the change in the optical absorption coefficient, $\Delta\alpha$. The analyses in the preceding sections provided an accurate knowledge of the quantum well widths, barrier heights and energy levels for both conduction and valence bands. This allowed a calculation of the expected QCSE energy shift based on the 'effective well width' method[19] (see Appendix). The measured and calculated energy shifts for mod05 (10.0% As), mod06 (15.6% As) and mod04 (26.4% As) are plotted in Figure 4.8 and the key parameters and results for the e1-hh1 transitions in these samples are summarized in Table 4-II. The field dependence of the exciton binding energy is a comparatively small effect and has been neglected in the approximation.

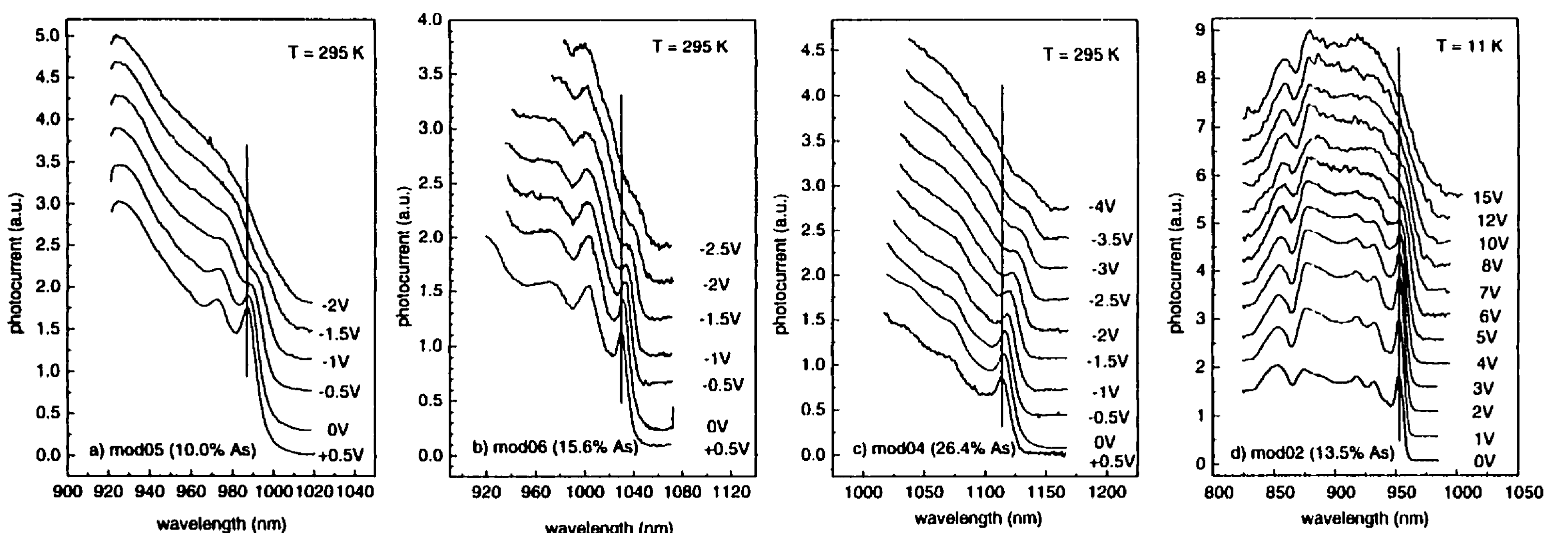

Figure 4.7 Spectral photocurrent response of p-i(multi-quantum-well)-n diodes as a function of reverse-bias voltage at T = 295 K for a) mod05 (10.0% As), b) mod06 (15.6% As), c) mod04 (26.4% As) and at T = 11 K for d) mod02 (13.5% As). The nominal intrinsic layer thickness is 0.6 μm in a), b), c) and 1.9 μm in d).

Table 4-II Parameters used in the effective well width calculation. The barrier heights and E1 energies were obtained from the Marzin—Bastard envelope function calculation of the quantum well energies. E1 is the energy of the first quantized level with respect to the bottom of the well. The effective masses in the direction of the electric field are not significantly affected by strain so the values listed are linear interpolations between InAs and InP. The effective well widths are "equivalent" infinite well widths chosen such that the zero-field E1 energies match. $\Delta\alpha$ is the measured field-induced absorption coefficient change in each structure and the voltage at which it is attained.

	Quantum well region		**Barrier heights**		**E1 levels**		**Effective masses**		**Effective well widths**		$\Delta\alpha$
Sample	**well width**	**As content**	**e1**	**hh1**	**e1**	**hh1**	**e1**	**hh1**	**e1**	**hh1**	
	(nm)	(%)	(meV)	(meV)	(meV)	(meV)	(m_0)	(m_0)	(nm)	(nm)	(cm^{-1}) ± 200
mod05	9.8	10.0	73	25	20	3.5	0.0734	0.626	16.0	13.0	2800 @ -1.0 V
mod06	10.3	15.6	113	39	24	3.7	0.0703	0.613	15.1	12.9	3100 @ -1.5 V
mod04	9.8	26.4	204	52	32	4.3	0.0642	0.587	13.5	12.2	3200 @ -2.5 V

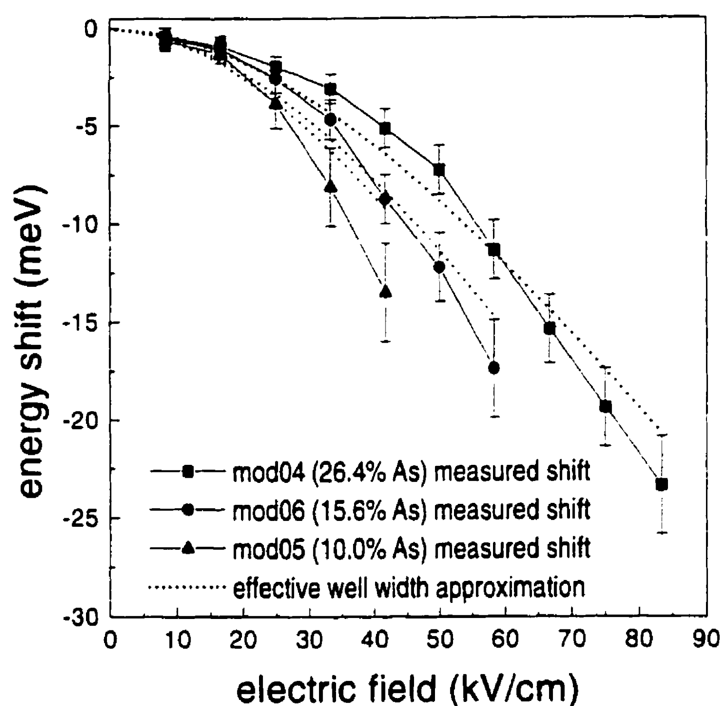

Figure 4.8 The field-dependent energy red-shift of the quantum well levels for mod05 (10.0% As), mod06 (15.6% As) and mod04 (26.4% As) determined from the photocurrent curves (Figure 4.7). The shift as approximated by the effective well width method using the parameters in is included for comparison.

$\Delta\alpha$ does not vary significantly among mod05 (10.0% As), mod06 (15.6% As) and mod04 (26.4% As) despite the differences in well depths, and degree of relaxation. The energy shifts in the relaxed samples are not detectably affected by the dislocations. The devices with shallower wells have less relaxation, less alloy disorder and hence sharper zero-field excitons but also field ionize more easily. There is good agreement between measured curves and the effective well width approximation in the low to moderate field range. At higher fields, and especially for lower barrier heights, electron and hole wave functions penetrate significantly into the finite barriers and the

approximation based on an infinite well loses validity. Under such conditions, the quasi-triangular barrier at the edge of the finite well is poorly approximated by the effective infinite well. Ultimately, all three devices give nearly the same change in absorption coefficient but this is achieved at significantly lower fields in the devices with shallower wells.

The behavior of mod02 is more difficult to analyze. In Figure 4.7d, we display the photocurrent spectra acquired at 11 K because of its improved resolution. The usual field-induced broadening of the e1-hh1 and e1-lh1 excitonic levels is clearly apparent but *without* any appreciable red-shift. This is similar to simple field ionization of excitons by an electric field in the direction parallel to the quantum wells. However, the exciton peak remains well-resolved at an electric field of ~42 kV/cm (~8 V), a value well beyond the unconfined ionization field. The exciton broadens as if it were quantum-confined. It is unlikely that this is due simply to the presence of dislocations because the relaxation characteristics of mod02 are quite similar to those of mod04. However, unlike mod04, mod02 contains much thicker buffer and spacer layers. The MQWS in mod02 is separated from the heavily doped contact layers on both sides by ~360 nm spacer layers of undoped InP. These spacer layers containing MDNs could affect the process of photo-carrier collection and partly explain the behavior. mod02 is currently under continued investigation.

IV. DISCUSSION

In every sample, the widths of the individual InAsP quantum wells are below the Matthews—Blakeslee critical limit for lattice dislocations while it has been exceeded for the MQWS. The relaxation is therefore characterized by the generation of MDNs at the outer interfaces of the MQWS. This causes a broadening of the optical absorption transitions. The dislocations perturb the crystalline energy band structure presumably in a manner similar to the way they distort the diffracting Bragg planes and broaden peaks in the HRXRD rocking curves. However, the number of defects in the core of the MQWS is sufficiently low that no dislocations threading through the MQWS in cross-section TEM measurements have been observed for either of the two extreme cases, mod04 (17 hc) and mod02 (18 hc). Thus as expected, the absorption and photocurrent spectra show that the good optical absorption properties of the light-absorbing intrinsic sections has been preserved. This is the first criterion that must be satisfied for the use of relaxed layers in photodiode devices.

The second criterion to be satisfied is the preservation of the essential electrical characteristics of the diodes in reverse bias. In-plane charge transport is seriously compromised by MDNs but the geometry of photodiodes is more forgiving. For example, it has been shown that MDNs in the InGaAs base region of AlGaAs/InGaAs/GaAs heterojunction bipolar transistors generally do not influence the

DC electrical behavior[14]. The operation of a QCSE optical modulator depends on the generation of rapid changes in the electric field across the MQWS junction; which in turn, is determined by charge transport to the heavily doped contact layers and capacitance effects across the junction. Because this does not rely on the transport of charge across the junction and through the MDNs, the generation and high frequency modulation of electric fields in the MQWS junction will not be greatly influenced by MDNs. The exception is at high fields near avalanche breakdown where the small number of dislocations that thread through the MQWS junction could facilitate charge leakage and the breakdown process. However, QCSE modulators are typically operated well below breakdown fields.

A more important concern is the effect of MDNs on the electric field uniformity. Non-uniformities could create significant field components parallel to the quantum wells and cause premature field broadening. In all the relaxed samples except mod02, the MDNs have formed very close to the heavily doped contact layers. The electrical response on the part of dislocation loops that extend into the contact layers is overwhelmingly screened by the large quantities of mobile charge. Hence, only the parts of the MDNs present in the undoped regions may appreciably affect the electric field. Placing the contact layers near the MQWS limits the extent of these potentially troublesome sections by making them very thin. As a result, the QCSE measurements in

mod05, mod06 and mod04 have demonstrated that the MDNs generally do not affect the electric field uniformity across the layers at the typical operating voltages.

We also need to consider that MDNs may affect the transport of photo-charge away from the junction. Optical absorption in QCSE modulators may saturate when the photo-charge cannot be efficiently cleared from the quantum wells in the core of the MQWS[43] but the junction can typically never be overwhelmed by photo-charge densities large enough to saturate the electric field. In these devices, the gross removal of such photocharge from the junction is essentially a dc process and hence largely unaffected by MDNs. It is important to remember, however, that while the dc characteristics of charge transport can be generally unaffected by moderate MDN densities, the high frequency characteristics are seriously compromised. This is a critical consideration if the photodiode is to serve as a high speed detector. In such a case, the effect of MDNs on the carrier mobility limits the frequency response of the diode. Noise and dark current characteristics are also compromised[8]. A good strategy for minimizing any undesirable effects in all cases is to bury the MDNs in the heavily doped contact layers.

Finally, we observe that the energy shift per unit electric field is clearly greater in the samples with shallower wells in agreement with similar results in the GaAs/AlGaAs[43] system. This is a result of the influence of the finite barrier height on the energy of the first quantized level with respect to the bottom of the well, E1. As an

alternative to the usual $m^*F^2L^4$ dependence[44], the shift can be shown to be dependent on $F^2L^2/E1$ (see Appendix); where m^* is the effective mass, F is the electric field and L is the quantum well width. Thus for two MQW systems having the same e1-hh1 transition energy, the one with wider and/or shallower wells will have a smaller E1 and demonstrate a larger shift for the same electric field. The use of shallower wells may not improve the maximum absorption coefficient change because of increased field broadening[45,46] of the excitonic feature, but an optical modulator using shallower wells may achieve useful on/off contrast ratios at lower fields. This is an important consideration for high-speed applications with severe drive voltage limitations[47].

The barrier height effect indicates that a clear advantage exists for structures with large conduction band offsets. There is considerable evidence that field-induced broadening of the excitonic transitions is determined by the electronic confinement. Compared to the valence band, the conduction band wave functions are less well-confined and field-assisted electronic tunneling probabilities can be significant at relatively low fields[45,46,48]. For two heterostructures differing only in their band offsets, the shift will be enhanced in the one with the smaller valence band discontinuity since the valence band term dominates. At the same time, the enhanced electronic confinement in this structure will also improve the resistance of the exciton to field ionization. In particular, it may be interesting to compare the performance of strain-relaxed InAsP/InGaAsP/InP, or even InAsP/InAsP/InP, MQW modulators with lattice-

matched InGaAsP/InGaAsP/InP[49] and InGaAs/InGaAsP/InP[50] MQW modulators for high-speed, low drive voltage applications at 1.3 μm and 1.55 μm. We expect that broadening due to MDNs at the outer interfaces of the separate confinement heterostructures in properly designed strained-layer InAsP structures can be largely compensated by: a "faster" shift and greater resistance to optical saturation by hole pile-up[43,50,51] due to the smaller valence band offset, superior electronic confinement due to the larger conduction band offset, reduced alloy disorder broadening and simplified growth conditions.

V. CONCLUSIONS

Strained-layer InAsP/InP p-i(MQW)-n optical modulators have been fabricated by MOVPE using layers with varying degrees of strain and relaxation. The samples have been characterized and analyzed using complementary HRXRD, TEM and optical absorption methods. We demonstrate in agreement with Refs. 20 and 21 that, following a determination of the multi-layer structural parameters, the e1-hh1 and e1-lh1 optical transition energies for such strained-layer superlattices may be accurately reproduced using the Marzin—Bastard model. Further evidence has been presented to support the hypothesis that the conduction band discontinuity for the InAsP/InP heterostructure follows a simple linear dependence on the As composition. Lower barrier heights in the MQWSs were found to enhance the QCSE red-shift and reduce the drive field. This

latter result showed that QCSE optical modulator performance can be improved by using heterostructures with large conduction band offsets. Misfit dislocation networks resulting from plastic relaxation at the interfaces bordering the MQWSs broaden optical absorption linewidths and degrade modulator performance but the devices can continue to function quite acceptably. If such partially relaxed structures can be stable, the use and control of misfit relaxation will in some instances allow a greater latitude in the design and fabrication of strained-layer materials and devices.

ACKNOWLEDGEMENTS

We thank G. Turcotte and J. Bouchard for their excellent technical assistance in realizing this study. This work was supported by the Natural Sciences and Research Council (NSERC) of Canada and the Fonds pour la Formation de chercheurs et l'aide à la recherche (FCAR) du Québec.

APPENDIX: EFFECT OF FINITE BARRIER HEIGHT ON THE QUANTUM-CONFINED STARK EFFECT

An electric field applied perpendicular to a quantum well causes the discrete levels of the well to red-shift. However, the excitonic transitions associated with these levels can continue to be well-defined for fields that are many times the usual bulk

ionization field because the conduction and valence band wave functions remain highly localized due to the quantum confinement. Thus according to Miller *et al.*,[19] large field-dependent changes in the band edge optical absorption are possible because the main excitonic transition at the band edge red-shifts appreciably before field broadening becomes severe.

The problem of electric field-dependent energy levels in a superlattice was first treated by Bastard *et al.*[44] using a variational method. The problem has since been studied by a variety of increasingly sophisticated methods[19,45,46,48,52,53,54]. The central issue in all formulations is that there do not exist any true bound states of the system for non-zero electric fields. Instead, we seek approximations to quasi-bound states that are long-lived. The usual strategy is to modify the band structure in the periphery of the quantum well to render the problem suitable for computation. Some recent approaches have given precise solutions for a wide variety of superlattice structures and electric field conditions[45,46,48,54]. However, these methods are complex and can obscure some of the fundamental physics. The original approach of Bastard *et al.*,[44] later extended by Miller *et al.*,[19] continues to be a very useful guide for designing optoelectronic devices because it provides an excellent insight into the physical situation. In this treatment of the problem, the response of the finite well to an applied electric field is approximated by the response of a wider infinite well, chosen so that their zero-field energy levels match (see Figure 4.9). An exact solution to the infinite well problem exists and the variational

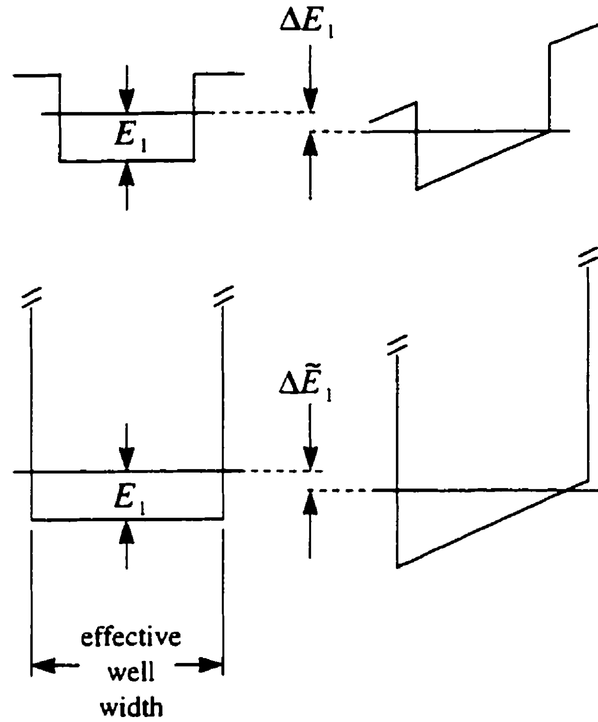

Figure 4.9 The effective well width approximation.

calculation of Ref. 44 gives an expression for the red-shift of the n = 1 energy level, $\Delta \tilde{E}_1$, in the low-field limit as:

$$\Delta \tilde{E}_1 \cong -C_{var} \frac{m^* e^2 F^2 L_{eff}^4}{\hbar^2} = -\frac{1}{8}\left(\frac{1}{3} - \frac{2}{\pi^2}\right)^2 \frac{m^* e^2 F^2 L_{eff}^4}{\hbar^2}\ ; \qquad \text{(A1)}$$

where m^* is the effective mass, e is the electronic charge, F is the electric field and L_{eff} is the width of the effective infinite quantum well. This gives the well-known $\sim m^* F^2 L_{eff}^4$ dependence of the red-shift. Equation (A1) may be rewritten as:

$$\Delta\tilde{E}_1 \cong -\frac{1}{8}\left(\frac{1}{3}-\frac{2}{\pi^2}\right)^2 \frac{\pi^2}{2}\frac{e^2F^2L_{eff}^2}{E_1} = -C_{var}\frac{\pi^2}{2}\frac{e^2F^2L_{eff}^2}{E_1} \tag{A2}$$

with

$$E_1 = \frac{\hbar^2\pi^2}{2m^*L_{eff}^2}. \tag{A3}$$

Hence, the red-shift varies as $\sim F^2L_{eff}^2 / E_1$. In this paper, the solution to the zero-field finite well problem for E_1 has been given by an envelope function calculation using the Marzin—Bastard model, but a first approximation for multi-quantum well structures may be obtained by solving the usual relations for a single finite well:

$$E_1 = \frac{\hbar^2\xi^2}{2m^*(L_0/2)^2} \tag{A3}$$

and

$$\xi^2 + \xi^2\tan^2\xi = \frac{2m^*(L_0/2)^2}{\hbar^2}V, \tag{A4}$$

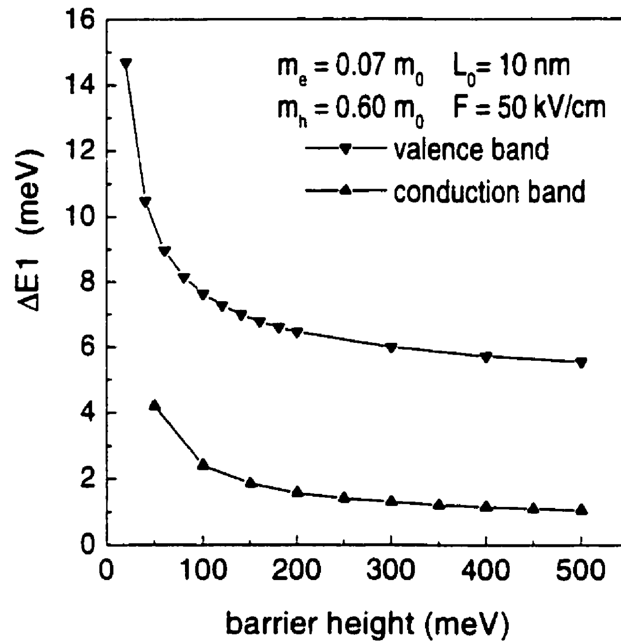

Figure 4.10 The effect of variations in the finite barrier height on the QCSE calculated using the effective well width approximation for a typical InAsP/InP quantum well in the presence of a 50 kV/cm electric field.

where V is the barrier height. We make the distinction between the width of the finite well, L_0, and the width of the effective infinite well, L_{eff}. E_1 is the energy of the first quantized level with respect to the bottom of the *finite* well. Hence, the utility of (A2) is that it gives the dependence of the red-shift explicitly on E_1 and L_{eff}; which are functions of L_0 *and* the barrier height V.

Heuristically, energy levels close to the bottom of the well "experience" greater changes in the local energy structure following the application of an electric field and follow more closely the contours of the field-distorted quantum well. Consequently, the red-shift per unit field is larger for these levels. The asymptotic limit as E_1 tends to zero is $eFL_0/2$ by geometrical inspection. The dependence of $\Delta\tilde{E}_1$ in (A2) on V for sample conditions in an InP-based quantum well is plotted in Figure 4.10. Most of the red-shift is developed in the valence band because it has a smaller E_1 due to the larger effective mass. Some caution should be exercised in interpreting the result as shallower wells giving larger shifts also suffer from enhanced field broadening. The present experiment with InAsP/InP quantum wells has shown that the excitonic features in the room temperature absorption spectra of quantum wells with electronic barriers of ~ 70 meV (mod05) are completely washed out by field broadening at only 30 - 40 kV/cm. Hence, efforts to reduce electronic barriers below this are dubious. Alternatively, Figure 4.10 shows that useful gains in $\Delta\tilde{E}_1$, and hence ΔE_1, should be possible by diminishing the hole barriers into the sub-60 meV range. Whether or not using shallower and wider wells can enhance the maximal absorption coefficient change depends upon the particular MQW structure under consideration. However, genuine reductions in drive field should be possible in most cases.

5 BAND ALIGNMENT ENGINEERING FOR THE QUANTUM-CONFINED STARK EFFECT

"For two heterostructures differing only in their band offsets, the shift will be enhanced in the one with the smaller valence band discontinuity since the valence band term dominates. At the same time, the enhanced electronic confinement in this structure will also improve the resistance of the exciton to field ionization." These concluding remarks of the previous chapter indicate that the ideal structure for a quantum-confined Stark effect application should incorporate an asymmetric band line-up with disproportionately large conduction band offset. If we are able to arrive at an understanding of the physical mechanism of the quantum-confined Stark effect and obtain some quantitative estimates for the degree of band line-up asymmetry required, it will then be possible to begin the design of optimal structures. This chapter presents a discussion of some important issues involved in the design and realization of the multi-quantum well stack for the quantum-confined Stark effect devices. The work has been prepared and submitted for publication as two papers. The first is a rapid communication presenting only the central idea and the second is a long detailed treatment. Since there is overlap between the content of the two manuscripts, only the second, longer manuscript is presented in this chapter. The shorter manuscript is included as an appendix to this thesis (see page 156). For the rapid communication, "Band alignment strategy for efficient optical modulation in quantum-confined Stark

effect devices," my contributions to the work included: the main idea, data analysis and model calculations and I was responsable for writing the manuscript. For the longer paper, "Band alignement engineering for high-speed, low drive voltage quantum-confined Stark effect devices," my contributions to the work included: establishment of the main idea, data analysis and model calculations, design of the InAsP/InGaP samples (in collaboration with P. Desjardins and L. Isnard), fabrication and characterization of the photodiode structures, band alignment analysis on the samples (with the aid of the computer program provided by M. Beaudoin) and I was responsable for writing the manuscript.

5.1 *Band alignment engineering for high-speed, low drive field quantum-confined Stark effect devices*

by R. Y.-F. Yip, P. Desjardins, L. Isnard, A. Aït-Ouali, H. Marchand, J.L. Brebner, J.F. Currie and R. A. Masut.

Groupe de recherche en physique et technologie des couches minces (GCM)

Département de génie physique, École Polytechnique de Montréal, et

Département de physique, Université de Montréal

C.P. 6079, succ. "Centre-Ville", Montréal QC, Canada H3C 3A7

Submitted to the Journal of Applied Physics on September 12, 1997

Abstract

An analysis and discussion of the device physics for the quantum-confined Stark effect based on barrier height and band alignment considerations is presented. It identifies two important design principles for band structure engineering of the multi-quantum well stack: 1) Due to the counterbalance relationship between field-induced redshift and field-induced polarization of the quantum well eigenstates, design strategies must look to attain an optimal balance or compromise between minimum drive field and maximum absorption coefficient change. This can be achieved with an appropriate choice of the valence band discontinuity. 2) In III-V semiconductors, the strong asymmetry in the field response of the conduction and valence band eigenstates is due directly to the asymmetry of the conduction and valence band effective masses. As a result, optimum device performance is obtained by using a heterostructure with a disproportionately large conduction band offset to compensate the effective mass asymmetry and balance the field-induced wavefunction leakage in the conduction band to that in the valence band. The relative wavefunction leakage between conduction and valence bands is compared by examining tunneling currents through the quantum well barriers as a function of electric field and barrier height. For conduction and valence band effective masses of respectively 0.055 and 0.5 times the electron mass, the optimal band alignment requires a conduction band discontinuity 3 - 9 times greater than the valence band discontinuity. Applying these design principles to high-speed, low drive voltage

optical modulators shows that the overall performance of these devices may be improved by using a combination of balanced band alignments and low valence band barriers. The low valence band barriers reduce the drive field required to operate the devices, which has direct effects upon the drive voltage, device capacitance, attenuation coefficient and optical coupling and propagation losses. The analysis and discussion is supported by experimental modulation depth and drive field data obtained from strained-layer multiple quantum well InAsP/InP and strain-compensated InAsP/InGaP optical modulators fabricated with layers grown on InP(001) by metal-organic vapor phase epitaxy.

I. INTRODUCTION

The engineering of band line-ups becomes a practical method for boosting device performance as advances in the growth and characterization of IV-IV, III-V and II-VI semiconductor alloys continue to widen the range of heterojunctions available to device and system designers. In the past, only lattice-matched, or nearly lattice-matched heterojunctions could be grown reliably. This severely restricted the set of heterojunctions with different band line-ups that could be used to fabricate a device. As a result, practical band line-up engineering was rather limited. More recently, advances in the understanding of growth and strain relaxation, and in the development of characterization methods makes it possible to produce metastable epitaxial layers over a

much larger range of strains and alloy compositions. The band line-up of a heterojunction is strongly dependent on both the alloy compositions of its constituents and on the state of strain at the interface. Therefore, access to this expanding range of heterojunctions impacts directly on the ability to perform practical band alignment design and engineering for devices.

The term quantum-confined Stark effect[1] (QCSE) refers to the fact that quantum wells have enhanced band edge optical absorption properties at room temperature that may be significantly tuned by an electric field. It is possible to obtain a relatively thick slab of material with these enhanced properties by forming a multiple quantum well stack (MQWS). By embedding the MQWS in a p-i-n photodiode, we obtain efficient voltage-controlled optical modulators. These photodiodes are operated in reverse bias and behave as simple capacitive loads whose electrical bandwidth is limited by the linear dimensions. So, very high operating frequencies (10 GHz - 1 THz) are achievable by making the devices small. The potential for impressively high modulation frequencies and the compatibility of the epitaxial growth and device processing with semiconductor diode lasers have led to widespread interest in the use of QCSE optical modulators for high-speed, long-range optical fiber telecommunications.[2,3] QCSE modulators are also used as primary building blocks in more complex applications such as photonic switching and smart pixel arrays.[4,5] This naturally raises the question of how to design the band structure of the MQWS for QCSE applications. Surprisingly, despite a

considerable body of material on the QCSE dating from the initial work of Mendez et *al.*,[6] clear design principles for the MQWS have not been established. In this paper, we propose two design principles and show that the design of the MQWS for QCSE devices may be considered a model problem in band line-up engineering.

Since the drive field required to operate QCSE optical modulators has been observed to decrease for decreasing valence band (VB) barrier heights,[7] and since premature delocalization[8,9,10] of the conduction band (CB) eigenstate is usually the main reason for loss of exciton oscillator strength with increasing field, we are led to conclude that device performance may be improved by using MQWSs with asymmetrically large CB offsets.[11] In the following section, we present a theoretical analysis on the effects of band alignment and barrier height variations on the device physics which concludes with two design principles for the band structure of the MQWS. Then, the theoretical analysis and design principles are compared against experimental data that have been obtained for QCSE optical modulators fabricated from strained InAsP/InP and strain-compensated InAsP/InGaP MQWSs grown in InP(001). Finally, the design principles are applied to the design of MQWSs for high speed, low drive voltage modulators for optical fiber telecommunications.

II. THEORY

Using simple 'particle in a box' models, it is possible to argue convincingly that optimization strategies for the design of the MQWS may be derived from the fact that the band structure effective mass in III-V semiconductors is significantly smaller in the CB compared to that in the VB. This leads directly to design principles based on achieving a balance between field-induced redshift and wavefunction polarization (quench), and a balance between the field-induced delocalization of the CB and VB wavefunctions.

A. Redshift

An enhancement of the redshift per unit field with decreasing barrier height is attributed to two mechanisms:

(1) Lowering the barrier height lowers the zero-point energy of the quantum well eigenstate relative to the bottom of the well and enhances its sensitivity to the energy gradient.

(2) The wavefunction penetration into the barrier under field is greater for lower barriers which decreases the degree of spatial localization of the eigenstate in the field distorted corner of the quantum well. This state necessarily attains a lower zero-

point energy than its counterpart in a quantum well with a higher barrier because of the uncertainty principle.

The field-induced redshift, ΔE_1, of the n = 1 zero-point energy level, E_1, in a quantum well is given approximately by[7]

$$\Delta E_1 \sim \frac{F^2 L^2}{E_1} \tag{5-1}$$

where F is the magnitude of the electric field, L is the well width and E_1 is the energy of the level measured with respect to the bottom of the quantum well at flat band. Here, only the optical transitions between the fundamental (n = 1) levels that define the absorption characteristics at the band edge are considered. For this discussion, the leading order behavior of these energy levels in MQWSs is described adequately by the solution for a finite rectangular well:

$$E_1 = \frac{\hbar^2 \xi^2}{2m^*(L/2)^2} \tag{5-2}$$

and

$$\xi^2 + \xi^2 \tan^2 \xi = \frac{2m^*(L/2)^2}{\hbar^2} V \tag{5-3}$$

where $2\xi/L$ is the wave vector in the well, m^* is the effective mass and V is the barrier height (or well depth).[12] The total redshift of the optical transition between electron and hole levels is the sum of the separate contributions from the CB and VB. Equations (5-1) - (5-3) show that L, m^* and V are the principal design parameters affecting the redshift.

The dependence on L suggests the use of wide wells to enhance the redshift of the quantum well energy levels. However, if the wells are too wide, the CB and VB wavefunctions can be strongly polarized when displaced to opposite sides of the well by an applied field and the value of the overlap integral[13] between the wavefunctions diminishes rapidly. This leads to a rapid reduction of the oscillator strength with applied field as the exciton is quenched inside the well. Hence, the maximum well width in QCSE applications is limited by the characteristic dimensions of the exciton system (equivalent Bohr radius ~ 10-15 nm). Typically, L is chosen to be somewhat inferior to the characteristic Bohr radius of the exciton so that the confinement potential of the quantum well approximately matches and bolsters the weaker Coulomb potential. This illustrates an important point about the QCSE: *the redshift and quench resistance are counterbalanced.* Upon application of the electric field, the electron and hole eigenstates

follow the contours of the linear energy gradient in opposing directions. A large redshift necessarily induces a strong polarization of the eigenstates with the corresponding reduction in the overlap integral and the oscillator strength of the absorption resonance. The converse is also true so that heterostructures exhibiting enhanced resistance to field quenching of the exciton resonance tend to display correspondingly less prominent redshifts per unit field. Since it is not possible to independently maximize redshift per unit field and minimize exciton quench, an optimal design for the MQWS seeks to balance these two considerations according to application-specific requirements.

According to equations (5-1) - (5-3), the VB component makes the dominant contribution to the total shift since E_l in the VB is usually much smaller than E_l in the CB due to the much larger VB effective mass.[14] Energy levels nearer to the bottom of the well exhibit enhanced sensitivity to applied energy gradients and yield larger redshifts per unit field. In addition to localizing the wavefunction more strongly in the bottom of the well, a large effective mass also improves the quench resistance by decreasing penetration of the wavefunction into the barrier under field.[15] In principle, a method for significantly modifying the effective masses along the direction of the confinement potential while maintaining a constant band gap (E_g) could be used to obtain optimal structures.

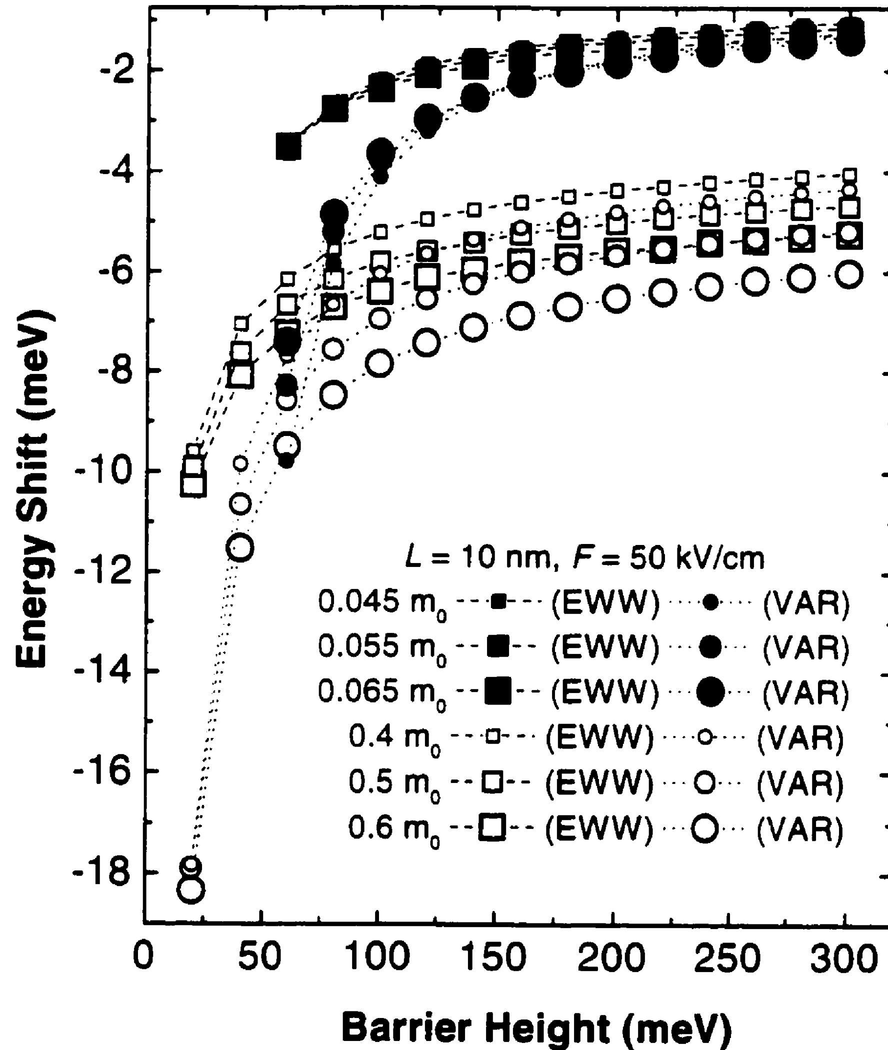

Figure 5.1 Variation of the field-induced shift, ΔE_l, of the n = 1 conduction and valence band quantum well energy levels with barrier height. Useful enhancements to the redshift per unit field may be achieved by using valence band barriers lower than 60 - 100 meV. The redshift has been calculated for electrons and heavy holes in a 10 nm wide quantum well with an applied field of 50 kV/cm using the effective well width method (see Ref. 1, EWW curves) and the variational model (see Ref. 13, VAR curves). The values for the effective masses are representative of conduction and valence band effective masses for InGaAsP alloys with $E_g \sim 0.8$ - 1.35 eV. m_0 is the electron mass.

Figure 5.1 illustrates how changes in the barrier height, V, affect the redshift, ΔE_l, and shows that useful enhancements to the redshift per unit field may be achieved by using VB barriers lower than 60 - 100 meV. Here, the redshift has been calculated for electrons and heavy holes in a 10 nm wide quantum well with an applied field of 50 kV/cm, using the effective well width method[1] (EWW curves) and the variational model[13] (VAR curves). The values for the effective masses span the range of CB and VB effective masses for InGaAsP alloys with E_g ~ 0.8 - 1.35 eV. Equations (1) - (3) show that $E_l \sim \xi^2 \sim V$ for small ξ and V. So, E_l has a nearly linear dependence on the barrier height for $V < \sim 60$ meV. On the other hand, as V increases to large values greater than ~ 100 meV, E_l saturates to the zero-point energy for an infinite well. Therefore, since $\Delta E_l \sim 1/E_l$, the redshift per unit field is nearly constant for $V > \sim 100$ meV but, as shown in Figure 5.1, increases significantly as the barrier height drops lower than 60 - 100 meV. Thus, it is possible to enhance the redshift per unit field and reduce the drive field by choosing VB barriers lower 60 - 100 meV. Less significant redshift enhancements are also available from the CB component. However, the wavefunctions in sub-100 meV CB wells are easily delocalized by modest electric fields (~ 50 kV/cm). The VAR curves show that the redshift actually increases with decreasing CB effective mass. Hence, it increases only with increasing wavefunction delocalization. This makes it impractical to enhance device performance by tuning V at the CB and strategies for reducing drive field should therefore concentrate on tuning V at the VB.

The contributions to the redshift due to barrier penetration effects and the uncertainty principle become significant for certain combinations of low barriers, narrow wells and/or strong fields. Under such conditions, QCSE calculations which use strongly-confined wavefunctions can significantly underestimate the true redshift. For small *V*, the effective well width method underestimates contributions due to these wavefunction delocalization effects. This accounts for the main difference between the EWW and VAR curves in Figure 5.1. Agreement with our experimental data is better for the VAR curves. Another example of this effect is clearly visible in a comparison of the simulated field-dependent optical absorption spectra for 'flat' and 'tilted' barriers computed by Yamanaka *et al.* (Figure 2 of Ref. 9) and by Ikeda and Ishikawa (Figure 4 of Ref. 10). The correction due to barrier penetration effects amounts to ~20% of the calculated redshift in Ref. 9. In the variational model used to produce the VAR curves in Figure 5.1, this contribution to the redshift is described by a series expansion in inverse powers of the barrier wave vector (see equations (19) to (23) in Ref. 13). However, the dependence of the redshift on these wavefunction delocalization effects is difficult to describe in a compact form like equation (5-1) and more sophisticated calculation models beyond the scope of the present discussion would be required to determine its exact nature. For present purposes, we can establish that equation (5-1) provides a reasonable estimate of the lower limit for the enhancement of the redshift per unit field with decreasing barrier height.

B. Quenching

When the width of the quantum well is chosen appropriately, field polarization of the CB and VB wavefunctions within a well does not lead to a severe reduction in the oscillator strength of the resonance. Instead, the resonance is quenched principally when a wavefunction becomes delocalized from the well by tunneling through the field-distorted barrier into the unbounded continuum. The authors of Refs. 8, 9, and 10 have remarked upon this in some detail and have concluded that field assisted tunneling is the primary mechanism responsible for exciton quench. In addition, quenching in most MQWSs used for QCSE applications is characterized by tunneling and wavefunction leakage at the CB. This must be the case when the ratio of CB to VB effective masses, m_e/m_h, is small, unless there is a large CB offset to compensate the effective mass asymmetry. As an example, consider a MQWS in which the band gap energy difference between well and barrier is partitioned equally between CB and VB. $m_e << m_h$ guarantees a larger zero-point energy level in the CB well with smaller well binding energy, and smaller attenuation constant in the barrier section. Therefore, the wavefunction penetration into the barrier and the probability tunneling current through the barrier is higher at the CB than at the VB both for flat band and under field. By inspection, field-induced quenching in this equipartitioned MQWS is due to premature delocalization of the CB wavefunction from the well. Such a configuration is not

optimal because the VB barrier height is higher than required, increasing the zero-point energy of the fundamental VB level and limiting the redshift. At the same time, the CB barrier height is lower than required to match the delocalization of the CB wavefunction to that in the VB, limiting quench resistance. Clearly, it is possible to conserve the fundamental optical transition energy and *choose an asymmetric band alignment with a larger CB offset that simultaneously improves both the resistance to quenching and the redshift per unit field without penalty.* The optimal asymmetry required to balance CB and VB wavefunction leakage is a function of the asymmetry between the CB and VB effective masses.

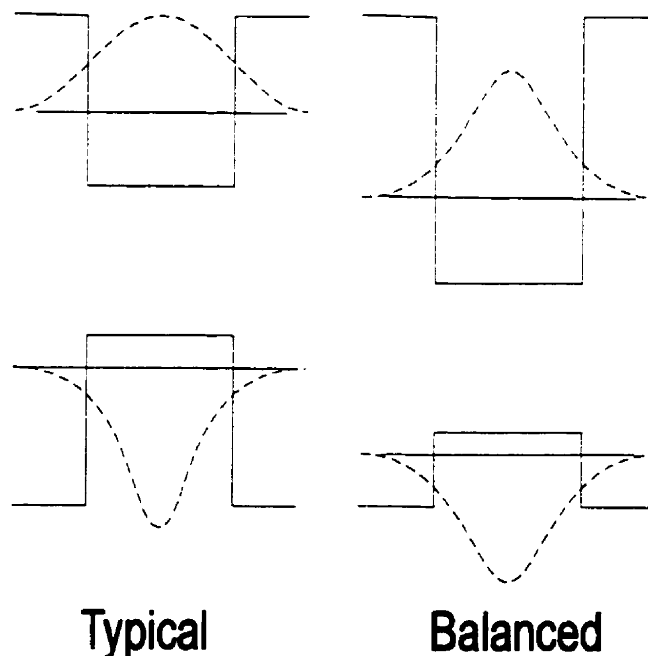

Figure 5.2. Band alignments at flat band are shown for a typical structure (left) and a balanced structure (right).

First, we establish the optimal band alignment at flat band that gives the maximum exciton oscillator strength. For a given well width, L, and total band gap difference, V_e+V_h, this condition occurs when both CB and VB eigenstates are equally localized in the well, maximizing the overlap integral (see Figure 5.2). The effective well widths[1] corresponding to infinite barriers that are often used in the approximate solutions for the finite well redshift provide a convenient measure of the degree of the spatial localization of the wavefunctions. Consider the solution for a single quantum well. The n = 1 energy level of a finite well is given by equation (5-2), which we equate to the expression for a wider infinite well of effective width, L_{eff}:

$$E_1 = \frac{\hbar^2 \xi^2}{2m^*(L/2)^2} = \frac{\hbar^2 \pi^2}{2m^* L_{eff}^{\ 2}} \tag{5-4}$$

Equation (5-4) yields

$$L_{eff} = \frac{\pi}{2\xi} L \tag{5-5}$$

where ξ is given by equations (5-2) and (5-3). Therefore, according to equations (5-3) and (5-5) the effective well width, L_{eff}, at the CB and VB are equal if and only if

$$m^*_e V_e = m^*_h V_h \qquad (5\text{-}6).$$

An identical result is obtained by equating the magnitude of the wavevectors (attenuation coefficients) in the barrier, or by equating the tunneling probability currents for electron and hole through rectangular barriers. We choose $m_e = 0.055m_0$ and $m_{hh} = 0.50m_0$ (m_0 is

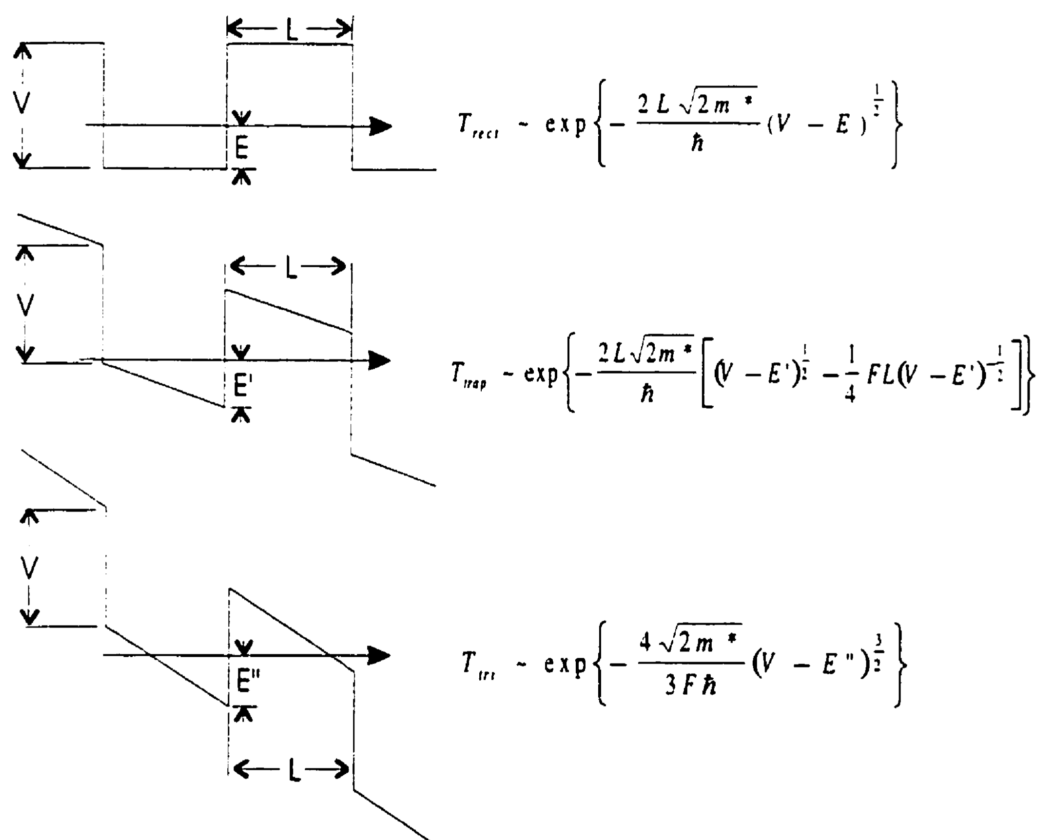

Figure 5.3 Conditions at the edge of the quantum well for a) flat band, b) moderate field and c) high field. T_{rect}, T_{trap}, and T_{tri} are the approximate analytical expressions for the probability tunneling currents obtained using the method of Wentzel, Kramers and Brillouin. See Ref. 20 for details.

the electron mass), which are values that are consistent with InGaAsP alloys with a band gap energy in the 1.3 - 1.55 μm range (0.95 - 0.8 eV).[16] Therefore, $V_e/V_h \sim 9$ for the optimal band alignment at flat band.

Next, we investigate the effects of the electric field on the balanced wavefunction leakage condition by using tunneling transmission probability currents to compare the degree of wavefunction localization at the CB and VB as a function of barrier height and electric field. The degree of band alignment asymmetry required for balanced leakage may then be estimated by solving for the barrier heights at the CB and VB which give equal tunnel currents. The three possible field conditions are illustrated in Figure 5.3. T_{rect}, T_{trap}, and T_{tri}, are the transmission tunneling currents through rectangular, trapezoidal and triangular barriers, respectively. The approximate analytical expressions for these tunneling currents shown in Figure 5.3 are obtained using the Wentzel-Kramers-Brillouin approximation method. The expressions show that the main factors that determine the tunneling current, or wavefunction leakage, are the magnitude of the attenuation coefficient (wavevector) in the barrier and the width of the barrier. The situation for $F = 0$ has already been discussed. At small fields ($F < (V - E)/L$), the balance is given by a ratio of trapezoidal expressions. As the field increases, the lower VB barrier becomes triangular ($F > (V_h - E_h)/L$) while the higher CB barrier remains trapezoidal ($F < (V_e - E_e)/L$) and the balance is given by a ratio of trapezoidal CB to

triangular VB expressions. Finally at sufficiently high fields, the balance is given by triangular CB and VB expressions.

Detailed investigations of similar tunneling problems have already been performed in the study of field emission of electrons (Fowler-Nordheim tunneling[17]) at metal-vacuum (MV) interfaces and field tunneling through metal-insulator-metal (MIM) interfaces.[18] But, there are two differences between this problem and the MV and MIM problems which must be addressed. 1) In a quantum well, the energy levels rise relative to the bottom edge of the barrier with applied field, so that the quantity $V - E$ decreases (ie. $E < E' < E''$, where the primes simply distinguish one case from the others) as shown in Figure 5.3; whereas, this quantity at the MV and MIM interfaces remains constant with applied field. 2) Unlike the MV and MIM problems which involve only the electron mass, field-assisted transport through quantum well barriers depends on both quantum well and barrier mass terms. For a leading order approximation, we neglect the difference between well and barrier effective masses, and choose nominal values for the CB and VB effective masses ($m_e = 0.055m_0$, $m_h = 0.50m_0$) giving $m_h/m_e \sim 9$ for InGaAsP alloys in the 0.8 - 0.95 eV range. 9:1 is a reasonable estimate for the effective mass asymmetry in the 0.8 - 0.95 eV range that is bounded by the ratios for the binary compounds: InP (1.34 eV, $m_h/m_e \sim 8.2$), GaAs (1.42 eV, $m_h/m_e \sim 7.3$), InAs (0.36 eV, $m_h/m_e \sim 17.8$). Apart from these modifications, the remainder of the analysis is similar to the MV and MIM problems. The well-established theory and results for the MV and

MIM problems are applied to compute the tunneling currents through rectangular, trapezoidal and triangular barriers,[17,18,19,20] and solve iteratively for the barrier heights

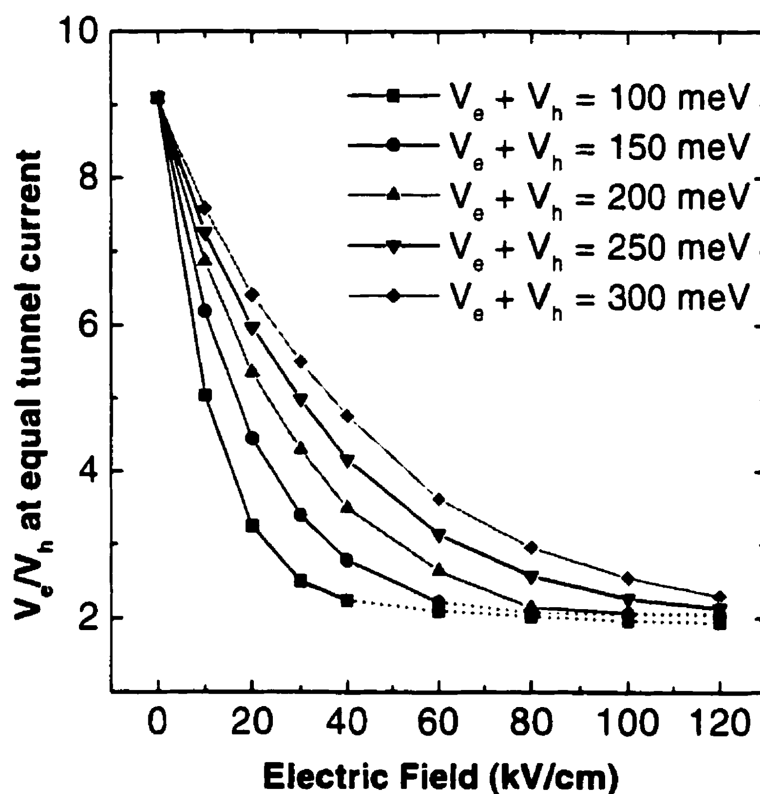

Figure 5.4. The ratio of CB to VB barrier heights giving equivalent probability tunneling currents (quench) as a function of the electric field. The curves have been obtained by writing the expressions (see Ref. 19 for details) describing the tunnel currents under the conditions illustrated in Figure 5.3 and then iteratively solving for the band alignments to give equivalent currents at the CB and VB. The dotted lines indicate approximately where the wave functions have become delocalized from the well based on the magnitude of the tunnel currents. These curves permit a estimate of the minimum barrier height required at the CB for a given barrier height at the VB in an optimal MQWS.

giving equivalent tunneling currents at CB and VB. The ratio of V_e/V_h corresponding to equal tunneling currents in the 10 nm wide CB and VB barriers is evaluated for increasing field and for a range of total quantum well depths (V_e+V_h) from 100 meV to 300 meV. These relations are plotted in Figure 5.4. The dotted lines indicate approximately where the absorption resonance has been completely quenched by comparing the evolution of the magnitude of the tunneling currents with experimental data (photocurrent spectra presented in the next section).

In Figure 5.4 , for each value of the total well depth V_e+V_h, there is a curve representing the band alignment for which the CB and VB wavefunctions are equally localized. This corresponds to the band alignment giving maximum oscillator strength as a function of applied field. For points off this curve, premature delocalization of either the CB or VB wavefunction with increasing applied field is responsible for quenching the absorption resonance. Quenching is VB-limited above the curve and CB-limited below the curve. Moving away from the curve into the region above corresponds to a decrease in the VB barrier height and increase in CB barrier height. This increases the redshift per unit field while decreasing oscillator strength, defining a compromise between field sensitivity and oscillator strength. Moving away from a curve into the region below, however, decreases both the redshift per unit field and oscillator strength since it increases the VB barrier height while decreasing it in the CB. Therefore, an optimal band alignment may occur only on a curve or in the region of VB-limited

quench above it. As such, the curves of Figure 5.4 provide an estimate for the minimum CB barrier height required for a given VB barrier height. Since realizable MQWSs correspond to fixed V_e/V_h ratios, it is not possible to satisfy the optimal oscillator strength condition across the entire range of operating fields. Therefore, an optimal alignment corresponds to the horizontal curve which best matches a member of the family of curves shown in Figure 5.4, or remains in the region above it, over the range of intended operating fields. For the effective masses that we have chosen, Figure 5.4 shows that this corresponds to $V_e/V_h \sim 3$ - 9 across a wide range of total well depths, V_e+V_h.

A survey of the literature shows that examples of QCSE-based devices incorporating MQWSs with band alignments near or in the target region of Figure 5.4 are rare. This implies that important improvements to the overall performance of devices may be achieved by including band alignment considerations in the design criteria. For example, a popular heterojunction such as $In_{0.53}Ga_{0.47}As$/InP, for which $V_e \sim 200$ meV and $V_h \sim 380$ meV, makes an especially poor choice for QCSE applications from a band alignment perspective. To date, most designs for MQWSs have tended to concentrate on the use of high barriers and/or reduced well widths to increase wavefunction localization and oscillator strength for obtaining the largest possible modulation depths. However, a principal effect of these strong localization designs is to impede the redshift and elevate the drive fields required to operate the devices.

In conclusion, from the combined redshift and quench analyses, the VB discontinuity is clearly a more important design parameter than the CB discontinuity. So, the band structure design should

(1) choose an appropriate VB barrier height to balance application-specific drive field versus optical modulation depth requirements, and then

(2) balance CB versus VB wavefunction leakage by choosing a sufficiently high CB barrier to ensure that premature delocalization of the CB eigenstate does not dominate the overall behavior.

III. EXPERIMENT

Strained-layer MQWSs were prepared by low-pressure metal-organic vapor phase epitaxy using trimethyl-indium, trimethyl-gallium, tertiarybutyl-arsine and phosphine precursors. The epitaxial layer growth on S-doped ($\sim 2\times10^{18}$ cm^{-3}) InP (001) substrates was carried out using Pd-purified H_2 as a carrier gas and with substrate temperatures of 600 °C for InAsP/InP and 620 °C for InAsP/InGaP. The reactor pressure during growth was maintained at 40 Torr. The flow conditions were chosen to give a free stream velocity at the substrate of ~ 60 cm/s with a full reactor evacuation time of ~ 1 s. In all cases, a nominal 100 nm buffer layer of undoped InP was grown on the substrate,

Table 5-I. Sample listing. The layer thicknesses and compositions are determined from a combination of x-ray diffraction, transmission electron microscopy and optical absorption measurements. The barrier heights and E_l levels are obtained by fitting quantum well transitions calculated using the Marzin—Bastard model for strained-layer superlattices to transitions measured by optical absorption at 8 K and 300 K. e1, hh1 and lh1 refer respectively to the n=1 levels in the conduction, heavy hole and light hole bands. The effective masses in the direction of the quantum confinement potential are linear interpolations between InAs and InP, given in units of the electron mass, m_0.

Sample	**Structure**	**Barrier Heights**			**E1 levels**			**Effective Masses**		
		e1	**hh1**	**lh1**	**e1**	**hh1**	**lh1**	**e1**	**hh1**	**lh1**
		(meV)	(meV)	(meV)	(meV)	(meV)	(meV)	(m_0)	(m_0)	(m_0)
mod05	25 × (9.8 nm $InAs_{0.100}P_{0.900}$ / 9.8 nm InP)	73	25	5	20	3.5	3.8	0.0734	0.626	0.111
mod06	25 × (10.3 nm $InAs_{0.156}P_{0.844}$ / 10.3 nm InP)	113	39	10	24	3.7	6.1	0.0703	0.613	0.095
mod04	25 × (9.8 nm $InAs_{0.264}P_{0.736}$ / 9.8 nm InP)	204	52	7	32	4.3	5.1	0.0642	0.587	0.095
gp18	20 × (7.8 nm $InAs_{0.17}P_{0.83}$ / 8.2 nm $In_{0.91}Ga_{0.09}P$)	138	86	4	35	6.7	2.8	0.070	0.610	0.104
gp24	20 × (8.4 nm $InAs_{0.26}P_{0.74}$ / 9.6 nm $In_{0.88}Ga_{0.12}P$)	210	120	5	38	6.5	3.8	0.065	0.590	0.095

followed by the growth of the MQWS and then a 300 - 500 nm Zn-doped cap layer for the p-contact. The structural characteristics of the samples and the results of the analyses by x-ray diffraction (XRD) and transmission electron microscopy (TEM) are summarized in Table I. Optical absorption spectra at 8 K and at room temperature were measured for the as-grown epitaxial layers using a free-flow, He-circulating cryostat with optical ports and a BOMEM DA3 Fourier transform interferometric spectrometer with a quartz halogen broad-spectrum source and Ge photodetector. The band offsets, barrier heights and n=1 quantized levels at the CB and VB have been determined using the method described by Marzin *et al.*[21,22,23] to perform multiple transition fits of the positions of optical absorption peaks using the structural data and state of strain in the multi-layers measured by XRD and TEM as inputs in an envelope function model for strained-layer superlattices (see appendix for details).

The fabrication of the InAsP/InP photodiodes is described in Ref. 7. The same procedure has been applied to the fabrication of the strain-compensated InAsP/InGaP samples except that the mesa wet etch was performed using a solution of $HCl:H_3PO_4:H_2O_2$ and the p-contact metallization was performed using a 20 nm Ag / 2 nm Zn / 180 nm Ag / 5 nm Au metal sandwich.[24] Room temperature measurements of the electric field-induced Stark shift of the quantum well optical transitions were performed by detecting the photocurrent response of the diodes as a function of reverse

bias voltage using a tungsten lamp source, a 0.3 m scanning monochromator and lock-in amplifier.

IV. RESULTS AND DISCUSSION

A. QCSE

We have compiled data from a representative set of p-i(MQW)-n photodiodes to illustrate the main points discussed in section II. All the MQWSs have similar well dimensions but vary significantly in CB and VB barrier heights. These samples are listed in Table I. The room-temperature spectral photocurrent responses of the photodiodes as a function of reverse bias voltage are plotted in Figure 5.5. The vertical axes of the photocurrent curves have been converted into absorption coefficient units by comparison with optical absorption spectra[25] and by using the structural data measured by XRD and TEM. A direct comparison of the photocurrent curves shows a clear enhancement of exciton oscillator strength and quench resistance with increasing barrier height. In sample mod05 (V_e ~ 73 meV, V_h ~ 25 meV), the exciton is completely quenched at 30 - 40 kV/cm whereas in sample gp24 (V_e ~ 210 meV, V_h ~ 120 meV) it remains discernible for fields larger than 150 kV/cm. The greater oscillator strength in high barrier MQWSs leads to greater absolute ($\Delta\alpha$) and relative ($\Delta\alpha/\alpha_0$) modulation

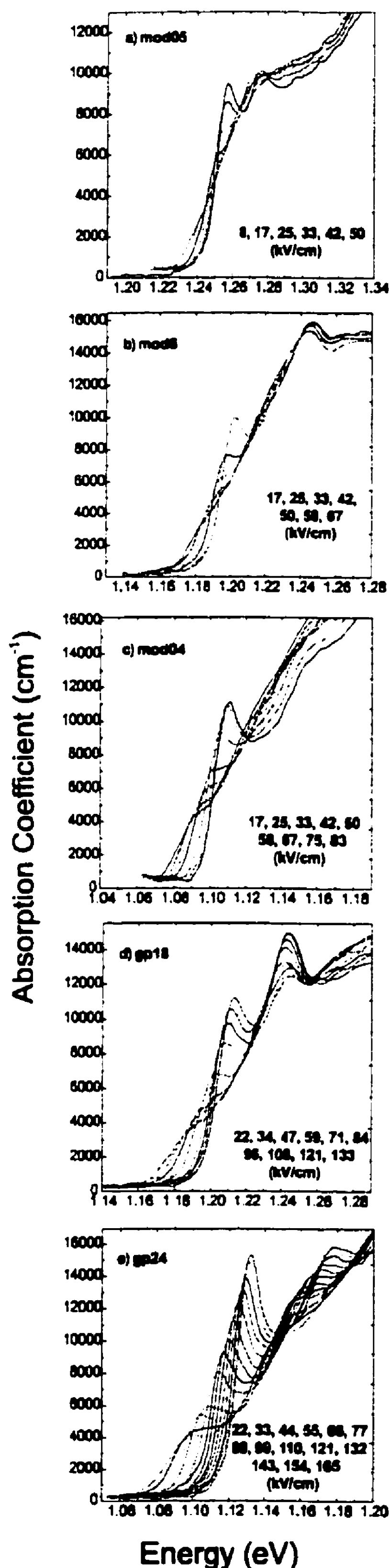

Figure 5.5. Field-dependent absorption spectra measured by photocurrent detection for: a) 25 × (9.8 nm $InAs_{0.100}P_{0.900}$ / 9.8 nm InP) (mod05), b) 25 × (10.3 nm $InAs_{0.156}P_{0.844}$ / 10.3 nm InP) (mod06), c) 25 × (9.8 nm $InAs_{0.264}P_{0.736}$ / 9.8 nm InP) (mod04), d) 20 × (7.8 nm $InAs_{0.17}P_{0.83}$ / 8.2 nm $In_{0.91}Ga_{0.09}P$) (gp18) and e) 20 × (8.4 nm $InAs_{0.26}P_{0.74}$ / 9.6 nm $In_{0.88}Ga_{0.12}P$) (gp24). For each of the five samples, the series of curves corresponds to the series of increasing electric field values indicated in the inset numbers. Pertinent data for the multi-quantum well stacks are summarized in Table 5-I.

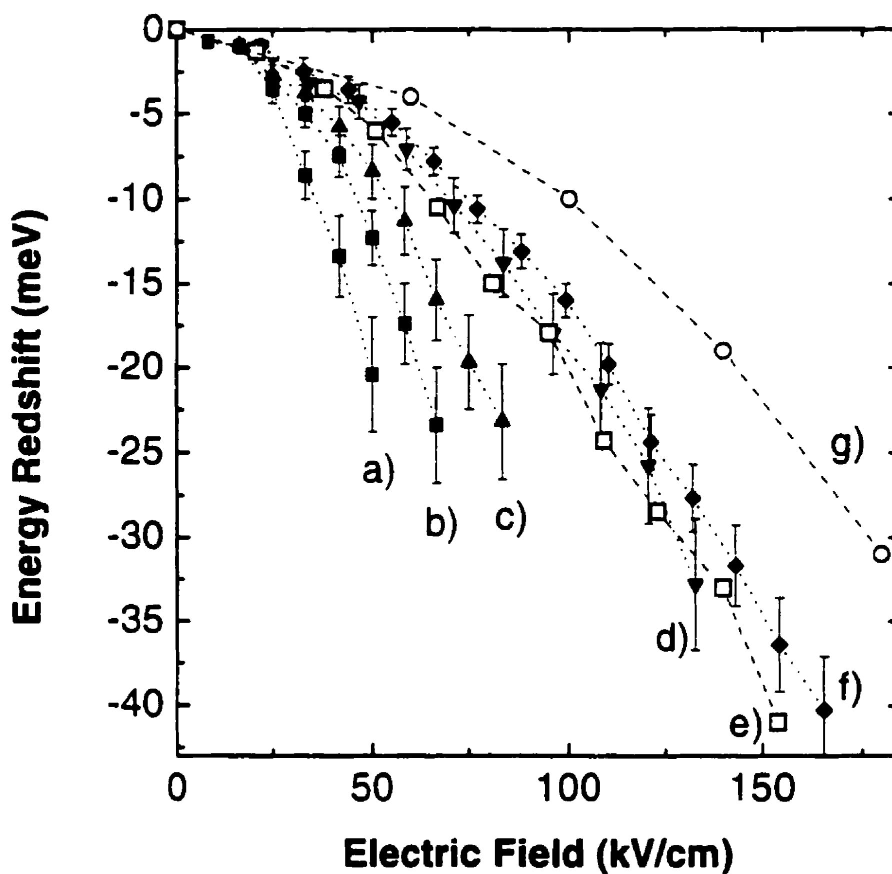

Figure 5.6. Energy redshift of the n=1 electron-heavy hole transition as a function of electric field. The curves for a) mod05, b) mod06, c) mod04, d) gp18 and e) gp24 are obtained from the spectra in Figure 5.7. Curve f) is data for a 40 × (10.5 nm $In_{0.53}Ga_{0.47}As$/6.8 nm $In_{0.52}Al_{0.48}As$ - lattice-matched to InP) MQWS operating at 1.55 μm from Ref. 27 and curve g) is data for a 21 × (10.0 nm $InAs_{0.53}P_{0.47}$/14.0 nm $In_{0.84}Ga_{0.16}P$) strain-balanced MQWS operating at 1.55 μm from Ref. 26.

depths, where α is the absorption coefficient and α_0 is the residual on-state absorption coefficient.

The redshift of the n=1 electron-heavy hole transition for each sample is plotted as a function of electric field in Figure 5.6. The redshift response for a strain-balanced $InAs_{0.53}P_{0.47}/InGa_{0.16}P_{0.84}$ MQWS[26] and for an $In_{0.53}Ga_{0.47}As/In_{0.52}Al_{0.48}As$ MQWS[27] lattice-matched to InP, both operating near 1.55 μm, have been included for comparison. The curves a, b, c, e and g, correspond to MQWSs with L ~ 10 nm and respective VB barrier heights of 25 meV, 39 meV, 52 meV, 200 meV (estimated) and 250 meV (estimated). Curves d and f correspond to InAsP/InGaP MQWSs with slightly smaller L (7.7 nm and 8.4 nm, respectively) and have been included for comparison. Although it is difficult to completely isolate the effect on the redshift due to the VB barrier height from those due the well width and effective mass, Figure 5.6 shows, in agreement with the theoretical analysis in the previous section, significant drive reductions associated with the lowering of the VB discontinuity.

The drive field reductions are balanced by losses in modulation depth, which we compare in Table II using two figures of merit. The modulation depth per unit drive field, $\Delta\alpha/F$, is commonly used to compare the performance of voltage drive optical modulators. $\Delta\alpha/F^2$ is inversely proportional to the average power per unit bandwidth required to drive the modulator (capacitive load) and is important for high frequency

Table 5-II. Comparison of the multi-quantum well stacks studied in this paper using two common figures of merit for optical modulators. The samples are listed from top down in order of increasing total barrier height. $\Delta\alpha$ is the change in absorption coefficient available at an applied electric field, F. The $\Delta\alpha$ values are measured in the region of low on-state loss (low energy tail of the exciton resonance) for which $\alpha_0 < 500$ cm^{-1}. t is the total thickness of quantum well material available for electroabsorption. This demonstrates the trade-off between modulation depth and drive field as a function of barrier height.

sample	$\Delta\alpha$ (cm^{-1})	F (kV/cm)	t (μm)	$\Delta\alpha$/F (kV^{-1})	$\Delta\alpha$/F^2 (cm/kV^2)
mod5d	1500	25 @ 1.5 V	0.245	60	2.40
mod6b	2900	40 @ 2.5 V	0.258	73	1.81
mod4c	3800	51 @ 3.0 V	0.245	75	1.46
gp18b	3200	88 @ 3.5 V	0.154	36	0.41
gp24b	6200	88 @ 4.0 V	0.168	70	0.80
Ref. 26	3800	80 @ 4.0V	0.195	48	0.91

applications.[28] The data has been obtained directly from the photocurrent curves in Figure 5.5 and from a similar curve in Ref. 26. In compiling the data for Table II, we restricted our attention to the region of low on-state loss below the band edge for which $\alpha_0 < \sim 500$ cm^{-1}. t is the total thickness of quantum well material. Despite rather wide variations in the CB and VB discontinuities (V_e and V_h), modulation depths ($\Delta\alpha$), and drive fields (F), the values for $\Delta\alpha/F$ are remarkably similar; consistent with the principle of balance between modulation depth and drive field. Since the trade-off between $\Delta\alpha$

and F is approximately proportional, the $\Delta\alpha/F^2$ values predict that low VB barrier designs will significantly outperform high VB barrier designs in high frequency applications where drive field considerations become paramount.

This indicates that the performance of MQWSs such as lattice-matched $In_{0.53}Ga_{0.47}As/In_{0.52}Al_{0.48}As$ or strain-compensated $InAs_{0.53}P_{0.47}/InGa_{0.16}P_{0.84}$ on InP for high data rate telecommunications is hampered by the high VB barriers which require large drive fields to induce significant redshifts. The power per unit bandwidth required to drive the modulator (capacitive load) scales as $P_{ac}/B \sim C\Delta V^2$, where P_{ac} is the drive power, B is the frequency bandwidth, C is the device capacitance and ΔV is the drive voltage. Total drive power, P_{ac}, is limited so that the available drive voltage becomes severely limited for high operating frequencies, B. MQWSs that require elevated drive fields to operate have device active regions (i.e. photodiode junction widths) significantly thinner than the characteristic dimension of the optical mode (typically λ/n ~ 0.45 μm, where n is the refractive index of the material). This has four notable disadvantages.

(1) A thin active modulator core is a poorly proportioned waveguide cavity for the optical mode, leading to greater propagation losses in the modulator section. It also increases the mismatch between the dimensions of the modulator waveguide and the

core of the optical fiber waveguide and decreases the acceptance angle for radiation exiting the laser facet so that coupling losses are greater.[28,29]

(2) High barriers make the removal of photocharge from the quantum wells less efficient. Charge pile-up in the wells can saturate the QCSE modulation and limit the incident optical intensities that may be tolerated by the device.[30,31,32]

(3) A thin junction increases the device capacitance, which both increases the power required to drive the load and decreases the electrical frequency response bandwidth of the load.

(4) A thin junction restricts the volume of active material available for electroabsorption. This directly decreases the final contrast (on/off) ratio of the modulator. Thus, when making direct comparisons of $\Delta\alpha$ between high and low barrier MQWSs, the larger values available in high barrier structures are somewhat misleading.

For high frequency, low drive voltage applications, we believe that low VB barrier samples are be a better choice despite the penalty in modulation depth ($\Delta\alpha$) because they allow the designer to share the advantages of a low drive field MQWS among any combination of the issues (1) - (4) plus the drive voltage. This allows for greater flexibility in the design of the optical modulator, the drive electronics and the coupling of modulator to the laser and optical fiber.

According to section II.A, significant redshift enhancements require VB barriers lower than ~ 60-100 meV. However, there must also be a lower limit for the VB barrier below which thermal effects begin to dominate. The key physical processes are thermal broadening and thermally-assisted tunneling, since thermionic emission involves photocarrier escape only after an absorption event and does not contribute to the absorption linewidth. These processes become significant as the barrier height approaches that of the thermal energy, $k_B T$ ~ 25 meV. But, it is difficult to discern a clear lower limit beyond which overall device performance will suffer enormously. For example, the operation of $GaAs/Al_{0.02}Ga_{0.98}As$ optical modulators[33] with total well depths as low as 25 meV has been demonstrated. This is an application-specific issue which depends most strongly on the minimum $\Delta\alpha$ that can be tolerated. Comparing samples mod05 and mod06, $\Delta\alpha$ drops appreciably from ~ 2900 cm^{-1} to ~ 1500 cm^{-1} when the VB barrier drops from 39 meV to 25 meV. Although it is difficult to make a firm conclusion from this limited set of data, these initial indications suggest that the modulation depths available from heterostructures with VB barriers lower than 25 meV may be too small for most applications and designs for low drive field MQWSs should target VB barriers in the 25 - 60 meV range.

B. Design of optimal structures

The design principles discussed in section II are applied to optical modulators for high bandwidth optical fiber telecommunications. Here, the drive fields are severely restricted by a combination of the low output voltages available from the drive electronics at high frequencies (>10 GHz) and the need to maintain sufficient junction widths for sensible active dimensions and low device capacitance. As modulation frequencies increase, the optimal balance between redshift enhancements and quench resistance skews towards low drive field designs. We have shown that useful drive field reductions may be achieved by choosing VB barriers in the 25 - 60 meV range. And then, to extract the full potential of the advantages afforded by low VB barriers, CB barriers should be 3 - 9 times higher according to Figure 5.4 so that premature delocalization of the CB wavefunction does not dominate the behavior. CB discontinuities up to ~ 9 times higher than the VB discontinuity can be appropriate since this gives the minimum exciton linewidth at flat-band, which reduces the intrinsic on-state loss and improves the relative modulation depth, $\Delta\alpha/\alpha_0$. Moreover, the drive field penalty due to increasing CB barrier height is very small since the CB contributes only a small fraction to the total redshift. Thus, we seek heterojunctions with VB barriers in the V_h ~ 25 - 60 meV range, CB barriers that are 3 - 9 times higher, and a fundamental optical transition energy that nearly matches 0.80 eV or 0.95 eV. This target structure

should be realizable using the system of strained III-V heterojunctions (Al, Ga, In, P, As) grown on InP(001) substrates.

Franciosi and Van de Walle[34] remarked that the band line-up at isovalent interfaces is observed to be largely independent of the interface properties and describable by linear response theories. Therefore, the band line-up between III-V quantum well and III-V barrier may be determined from a knowledge of the compositions of the alloys and the state of strain at the interface.[35] The engineering of band alignments for our case then becomes largely an exercise in mapping the phase space of the band gaps and band alignments for the (Al, Ga, In, P, As) system on InP as a function of composition and strain. Examples of such phase space maps are the linear response calculations performed by Krijn[36] and Ishikawa and Bowers[37] for InGaAsP on InP and InGaAlAs on InP.

The applicability of the linear theories relies on the existence of a common reference energy level, or energy scale, across the entire range of alloy compositions. In principle, when this hypothesis is satisfied, a mapping of the CB and VB positions for the ternary and quaternary alloys relative to a common reference energy can be obtained from a knowledge of the material parameters of the binary alloys: band gap energies and band line-ups, lattice constants, elastic moduli, strain deformation potentials and bowing constants. The procedure has been outlined by Van de Walle.[38] Obtaining a useful final

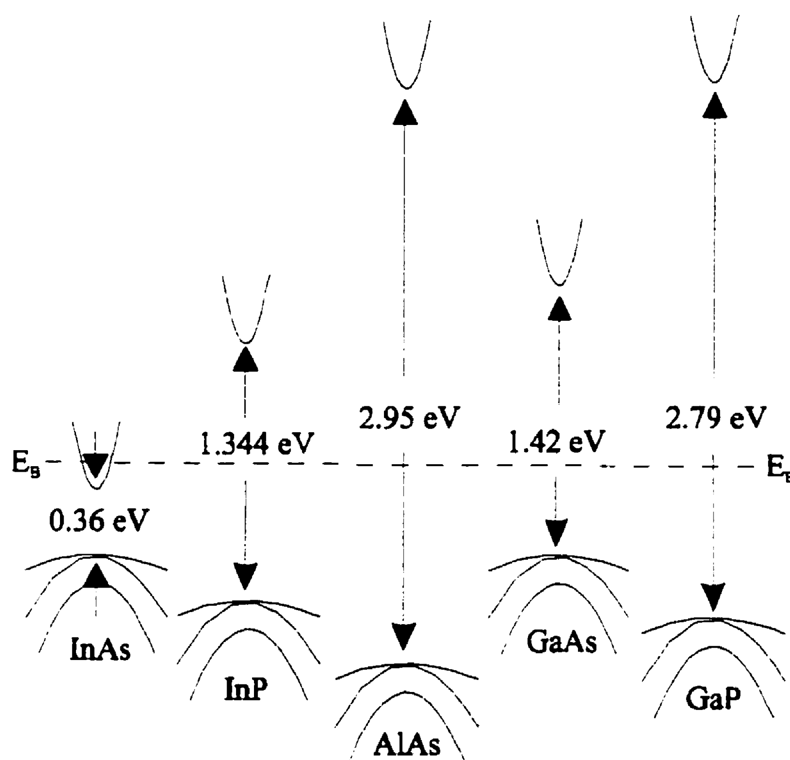

Figure 5.7. The unstrained neutral line-up of the five common III-V binary compounds according to the quantum dipole model of Tersoff (Ref. 39) and Tejedor and Flores (Ref. 40). In the theory, the position of the VB maximum relative to a reference midgap level, E_B, may be computed from the bulk properties of the material alone. It is predicted that the bands across a heterojunction interface will be aligned such that the difference between the E_B levels in adjacent materials is small (nearly zero). The positions of E_B relative to the VB maxima are 0.50 eV (InAs), 0.76 eV (InP), 1.05 eV (AlAs), 0.50 eV (GaAs) and 0.81 eV (GaP) These values are reproduced from Ref. 39. The direct gap transitions are shown for GaP and AlAs.

result begins with accurate values for the unstrained binary line-ups. The band alignments of the five (InAs, InP, AlAs, GaAs, GaP) binary compounds, whose ternary and quaternary derivatives are used to produce heterostructures operating at telecommunications wavelengths, as predicted by the quantum dipole theory due to Tersoff[39] and to Tejedor and Flores[40] are shown in Figure 5.7. This set of band line-ups

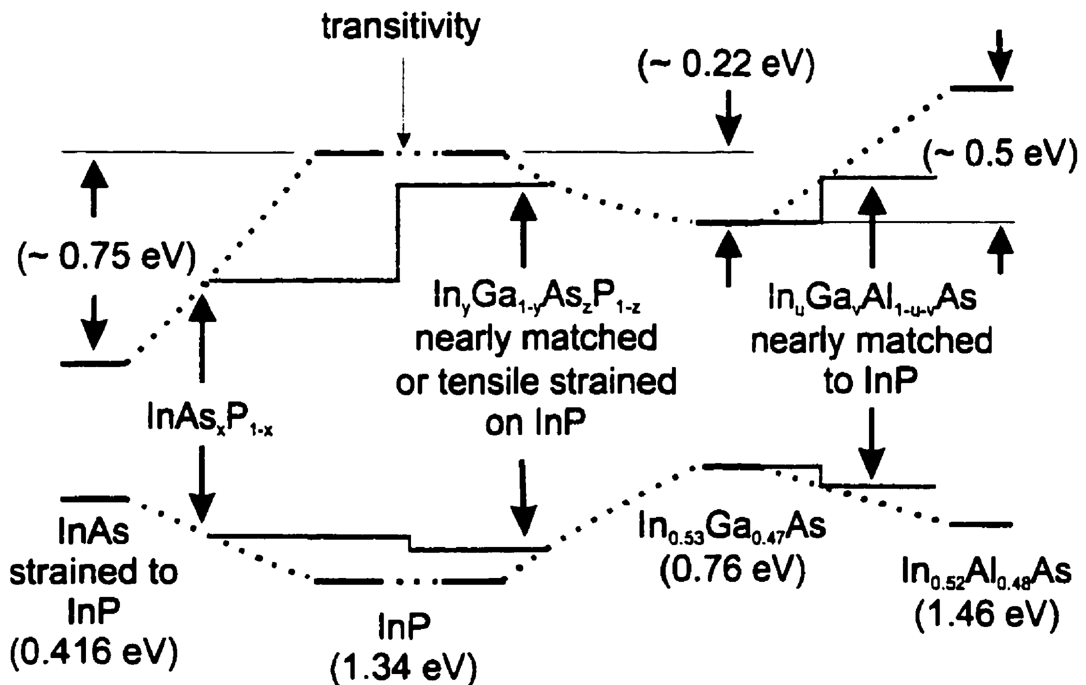

Figure 5.8. Two possible strategies for obtaining heterojunctions with large conduction band offsets, small valence band discontinuities in the 25 - 60 meV range and a fundamental optical transition energy near 0.8 eV or 0.95 eV. The band alignments shown for the $In_{0.53}Ga_{0.47}As$/InP and $In_{0.53}Ga_{0.47}As/In_{0.52}Al_{0.48}As$ heterojunctions correspond to widely accepted values (Ref. 45). The band alignment shown for the strained InAsP/InP(001) heterojunction corresponds to the experimentally determined values in Refs. 7, 23 and 43, and agrees well with the model predictions of Ref. 39.

shows good agreement with experimental results and predicts that the target band structure with the small VB offset alignment and total well depth that we seek can be achieved in the (Al, Ga, In, P, As) system on InP.

In Figure 5.8, we propose two candidates for the target band structure:

(1) The system of strained InAsP/InGaAsP alloys on InP(001): the strained line-up of $InAs_xP_{1-x}$/InP for $\{0 < x \leq 1\}$ corresponds to $V_e/V_h \sim 3 - 4$, while the lattice-matched $In_yGa_{1-y}As_xP_{1-x}$/InP line-up corresponds to $V_e/V_h \sim 0.5 - 1.0$. Therefore, using the InP CB and VB positions as common reference levels (transitivity), the band line-up of InAsP/InGaAsP grown on InP for strained wells and lattice-matched barriers should yield $V_e/V_h \geq \sim 3 - 4$. As an example, operation at 0.8 eV would require ~ 10 nm wide $InAs_{0.58}P_{0.42}$ wells with an band edge excitonic transition near 0.82 eV. A barrier made from InGaAsP nearly lattice-matched to InP in the 0.90 - 1.15 eV range should give a VB barrier in the target 25 - 60 meV range with the desired band offset asymmetry. Beyond this departure point, extensive tuning of the band alignment is possible by varying in the composition and strain of well and barrier. In fact, the use of tensile strained barriers is likely necessary to compensate the large compressive strain in the InAsP wells and allow the growth of a thick MQWS.

(2) The system of nearly lattice-matched InAlGaAs/InAlGaAs alloys on InP(001): the $In_{0.53}Ga_{0.47}As/In_{0.52}Al_{0.48}As$ system lattice-matched to InP is suitable for operation at 0.8 eV and reported to have a relatively favorable band line-up with $V_e/V_h \sim 2.5:1$. But, the barrier heights are too high, especially the ~200 meV VB barrier. Since Ga and Al may be substituted for each other without inducing large strains, the line-up of $In_{0.53}Al_xGa_{0.47-x}As/In_{0.52}Al_yGa_{0.48-y}As$ lattice-matched to InP is expected to retain a nearly constant V_e/V_h ratio for $\{0 \leq x \leq 0.47, 0 \leq y \leq 0.48 \mid x < y\}$. As in the

preceding case, extensive tuning of the alignment is possible by using strained and strain-compensated combinations of well and barrier.

There are important additional design constraints posed by the practical issues related to the epitaxial growth of such structures for operation at telecommunications wavelengths. For example, a 0.8 eV (1.55 μm) transition would require ~ 10 nm InAsP wells of 50-60% As corresponding to large (1.5 - 2%) compressive strains. The number of quantum wells and the active volume of the modulator core is limited by the critical strain for the onset of morphological instabilities during growth and/or the critical thickness for the formation of extended defects in the strained MQWS. One approach that has been used with some success is the insertion of tensile strained barrier sections to achieve a large degree of strain compensation and extend the critical thickness into a useful range. Cunningham and Goossen[41] reported successfully using this approach to produce a thick 50 × (8.5 nm $In_{0.25}Ga_{0.75}As$/ 8.5 nm $GaAs_{0.5}P_{0.5}$) MQWS on GaAs with +1.8%/-1.8% strained wells and barriers for QCSE modulators operating 1.06 μm. Carlin *et al.*[42] reported producing 17 × (10 nm $InAs_xP_{1-x}$/ 15 nm $In_yGa_{1-y}As_xP_{1-x}$) MQWSs on InP with +1.8%/-0.9% strained wells and barriers for lasers operating at 1.55 μm. This latter result is noteworthy because it raises the possibility of using a single growth sequence to produce both a high performance laser and a high performance optical modulator.

V. CONCLUSIONS

The engineering of the band alignment is a promising and logical refinement to expand the performance envelope of QCSE optical modulators. However, a complete optimization of the design of the MQWS is difficult requiring a high level of cross-disciplinary expertise across a wide range of materials and device issues. Accordingly, we have attempted to downplay the reliance on numerical treatments using figures of merit and placed the emphasis on the physical principles that they are intended to represent. This has led to novel concepts for designing the band structure of the MQWS:

(1) Balancing energy redshift enhancements versus loss of oscillator strength with an appropriate choice of the VB barrier height to suit application-dependent drive field versus optical modulation depth requirements.

(2) Balancing the wavefunction leakage at the CB and VB with an asymmetric band alignment to compensate the effective mass asymmetry between the CB and VB.

In many cases, and especially for high speed, low drive voltage applications, we believe that it is advantageous to pursue balanced designs incorporating relatively low VB barrier heights to enhance field sensitivity and lower the drive field. This can improve the overall performance by permitting a lower drive voltage and/or wider diode junction with larger active volume, lower capacitance, lower propagation losses and improved

laser-modulator and modulator-fiber coupling. A MQWS possessing the desired band alignment and VB barrier heights that is capable of operating in the 1.3-1.55 μm range for optical telecommunications should be achievable using a combination of strained III-V semiconductor alloys that are commonly grown onto InP substrates.

ACKNOWLEDGMENTS

We thank Dr. Mario Beaudoin for providing the computer program used to calculate the energy levels in a strained-layer superlattice as a function of the band discontinuities, and Gino Turcotte and Joel Bouchard for their excellent technical assistance in realizing this study. This work was supported by the Natural Sciences and Engineering Research Council (NSERC) of Canada and the Fonds pour la Formation de chercheurs et l'aide à la recherche (FCAR) du Québec.

APPENDIX - NOTES ON THE BAND ALIGNMENT DETERMINATION USING RECTANGULAR QUANTUM WELLS

The band alignments for the heterostructures listed in Table I have been determined by performing multiple transition fits of computed quantum well energies to the optical transition energies measured by optical absorption.[21] By obtaining accurate structural data by XRD and TEM and then applying the Marzin-Bastard envelope

function model for strained-layer superlattices to fit the optical transition energies measured at low and room temperature, it has been possible to determine the band alignment of InAsP/InP with good success.[7, 23, 43] It was determined that the CB discontinuity in the system of strained InAsP/InP is 7.56 ± 0.08 meV/As% giving 75.8 ± 2.7 % of the total strained band gap difference, ΔE_g.

The precision in the determination of the InAsP/InP alignment is somewhat surprising considering that the experiment has been performed with rectangular wells and not parabolic wells, for which the transitions resulting from band structure calculations are reputed to be more sensitive to the specified band alignment.[44] The analysis of the redshift in section II.A can explain the success of this determination. The total optical transition energy resulting from a model calculation is the sum of three main components: the zero-point energy in the CB well, the zero-point energy in the VB well and the energy band gap of the quantum well. Both of the calculated zero-point levels necessarily demonstrate some dependence on the specified partition of the energy gap difference between the CB and VB discontinuities. The computed transition energies between strongly-confined levels that are deep in the quantum well can be largely independent of the specification of the partition because they are nearly constant functions of the barrier height. In addition, varying the partition causes, say, the CB well to become deeper while the VB well compensates by becoming shallower. Thus, even in cases for which there are significant variations the CB and VB zero-point energies, it is

possible that their sum remains nearly constant. This point is illustrated in Table III with a sample calculation of the n=1 electron-heavy hole (e1-hh1) transitions for the sample mod06. As barrier heights decrease, the energy levels can become sensitive to variations in the quantum well barrier height and band alignment. Therefore, the accuracy of a band alignment determined by using multiple transition fits in rectangular wells is determined mostly by fitting the shallow transitions, since only the computed transition energies involving shallow levels are sensitive to variations in the partition. Unfortunately, these are often optical transitions involving higher order levels. They can exhibit broad resonances and also be generally difficult to identify (e.g. see discussion in Ref. 23). Moreover, band structure models reproduce higher order levels with less accuracy than the fundamental levels. For these reasons, the fit of absorption spectra from deep well GaAs/AlGaAs samples has been problematic.[45,46] Marzin *et al.*[21] also reported that they were unable to use this method to deduce the band alignment of moderately strained, or lattice-matched, InGaAs/InAlAs on InP with satisfactory accuracy.

The accuracy in the determination of the InAsP/InP band alignment is intimately related to the fact that the splitting of the heavy and light hole VBs due to compressive strain provides a pair of sharp and clearly identifiable fundamental resonances to fit. Referring again to the sample calculation shown in Table III, both the electronic and heavy hole levels can be considered to be deep in the quantum well. So, computed e1-

Table 5-III Variation of the quantum well transition energies of sample mod06 computed using the Marzin—Bastard model with changes in the band alignment. e1-hh1 and e1-lh1 refer respectively to the optical transitions between the n=1 conduction-heavy hole and conduction-light hole levels. ΔE_C, ΔE_V and ΔE_g are respectively the conduction band discontinuity, valence band discontinuity and total energy band gap difference between quantum well and barrier. E_l refers to the n = 1 quantum well energy levels. As the partition of the band gap energy difference between CB and VB changes, the e1-hh1 transition remains nearly constant while the e1-lh1 shifts. This shows that in the InAsP/InP system, the difference between the heavy and light hole transitions can be a sensitive key for determining the band alignment.

Partition	**Transitions**		**conduction band**		**heavy hole**		**light hole**	
$\Delta E_C/\Delta E_g$	**e1-hh1**	**e1-lh1**	ΔE_C	E_l	ΔE_V	E_l	ΔE_V	E_l
	(meV)	(meV)	(meV)	(meV)	(meV)	(meV)	(meV)	(meV)
0.67	1.296	1.331	102.5	21.9	50.8	3.9	21.3	9.0
0.69	1.296	1.330	105.9	22.1	47.4	3.8	17.9	7.9
0.71	1.297	1.329	109.3	22.4	44.0	3.8	14.5	6.8
0.74	1.297	1.328	112.7	22.6	40.6	3.7	11.1	5.5
0.76	1.297	1.327	116.1	22.8	37.2	3.6	7.7	4.0
0.78	1.297	1.325	119.5	23.0	33.8	3.6	4.3	2.3
0.80	1.297	1.324	122.9	23.2	30.4	3.5	0.9	0.5

hh1 transitions are effectively constant despite a relatively wide variation in the specified partition. The light hole level is weakly-confined due to the combination of a small effective mass and low barrier height resulting from the modifications to the VB under compressive biaxial strain. As a result, both the computed light hole level and n = 1 electron-light hole transition exhibit a nearly linear variation with VB barrier height and band alignment. The computed difference between the heavy and light hole transitions is therefore strongly-dependent on the specified partition. The value measured by optical

absorption is 34 meV for this sample (mod06). We assume that the binding energy of heavy hole excitons is 2-4 meV greater than that of light hole excitons. So, the partition which gives a computed 30-32 meV energy difference provides a good estimate for the band alignment. The confidence interval for the estimate is improved by using higher order transitions as secondary alignment keys and by performing the measurement on a set of MQWSs spanning a range of alloy compositions.[23] Schneider and Wessel[47] have also remarked that the hh-lh energy splitting is a sensitive key for determining the band alignment of $InAs_{0.67}P_{0.33}$/InP quantum wells from photoluminescence excitation spectroscopy.

Thus, the nature of a small VB offset and compressive strain in the InAsP/InP system have 'conspired' to guarantee a low light hole barrier and facilitate an accurate determination of the alignment. The result shows that it is not always necessary to resort to more exotic confinement potentials, such as graded or parabolic wells, to obtain an accurate measurement of the band alignment. The growth and characterization of exotic structures is usually more difficult which decreases confidence in the measurement of the compositions and dimensions of the quantum wells. Rectangular wells, which are the simplest to grow and characterize accurately, may be used when the experiment can be designed to yield clearly identifiable optical transitions whose computed values vary sufficiently when the partition is changed.

5.2 *Additional Remarks*

Qualitative agreement between the predictions of the linear response theories and the trends in experimental data is good. In some cases there is also good quantitative agreement but data on band alignments across a wide range of alloy compositions and with sufficient accuracy for designing devices is generally not available. Furthermore, there are some notable discrepancies between the our experimental results and band line-up for InAsP/InP that was computed by Ishikawa and Bowers[37] and by Krijn.[36] This is due mostly to the starting value for unstrained InAs/InP binary line-up that they have chosen. We can make an immediate contribution here by using the method proposed by Van de Walle[38] to re-calculate the phase space map of the (Al, Ga, In, As, P) alloys based on more accurate information (eg. the binary line-ups computed by Tersoff,[39] or the best available experimental data). Unfortunately, the unstrained band line-up for the binary alloys, which is the departure point for the calculation is, in nearly all cases, a purely theoretical construction that has no direct experimental verification.

6 CONCLUSIONS

The operating wavelength (determined essentially by the energy band gap of the material) of a QCSE device is in the range ~ 800 - 2000 nm; so that, in an absorption device, a relatively thick stack of ~ 20 - 50 quantum wells is required to have any appreciable interaction with the optical mode. In general, such thick stacks exceed the critical limit for strain relaxation via lattice dislocations. Therefore, approaches involving strain compensation or partial strain relaxation in buffer layers are required to produce defect-free device layers. Once grown, the quantum well stacks can be characterized and analyzed using complementary XRD, TEM and optical absorption methods to accurately determine the layer thicknesses, the state of strain and strain relaxation (from which it is possible to infer the alloy composition) and the heterojunction band discontinuities.

In p-i(MQW)-n optical modulators that have been fabricated using strained InAsP/InP and strain-compensated InAsP/InGaP layers grown by MOVPE, lower valence band barrier heights in the multiple quantum well stacks were found to enhance the QCSE redshift and reduce the drive field. This result showed that the overall performance of QCSE devices can be improved by using heterostructures with large conduction band offsets to compensate the effective mass asymmetry in III-V semiconductors. After considering the effects of barrier height and band alignment

variations on the device physics of the QCSE, a new strategy has been proposed for designing the band structure of the MQWS based upon two principles:

1) balancing the energy redshift versus the loss of oscillator strength with an appropriate choice of the VB barrier height, and
2) balancing the wave function leakage in the CB to that in the VB with an asymmetric band alignment. In many cases, and particularly for high speed, low drive voltage applications, it is advantageous to pursue balanced designs incorporating relatively low VB barrier heights to enhance field sensitivity and lower the drive field.

This can improve the overall performance by permitting a lower drive voltage and/or wider diode junction with larger active volume, lower capacitance, lower propagation and coupling losses. A MQWS possessing the desired band alignment and VB barrier heights that is capable of operating in the 1.3-1.55 μm range for optical telecommunications should be achievable using a combination of strained III-V semiconductor alloys that are commonly grown onto InP substrates. The most promising candidates are the systems of

1) compressively strained InAsP wells with tensile strained InGaAsP barriers on InP(001), and
2) nearly lattice-matched InGaAs wells and InAlGaAs barriers on InP(001).

The InAsP/InGaAsP system merits some additional consideration since this heterojunction has already been used to produce record performance laser structures. Therefore, a single growth may be used to produce an integrated high performance laser and high performance QCSE modulator. Examples in the literature have also demonstrated how to suppress the 2D-3D hybrid growth transitions that would normally be induced by the high lattice strains in this system (~ 1.8 % for operating wavelengths near 1.55 μm) and obtain the thick quantum well stacks required for QCSE devices.

A simple model of quantum well interaction with a single bandgap solar cell has been developed to conduct a brief critical review of the literature on the use of quantum wells to improve the energy conversion efficiency beyond the detailed balance limiting efficiency for single bandgap cells. The results of the model calculations agree with experimental observations showing that the potential practical conversion efficiency enhancements are small.

7 REFERENCES

Chapter 2 - Experimental Methods and Background

[1] http://argon.eecs.berkeley.edu:8080/~ee143/Process_Description/.
http://argon.eecs.berkeley.edu:8080/~ee143/Process_Description/#2.

[2] G. B. Stringfellow, *Organometallic vapor phase epitaxy: theory and practice* (Academic, Boston, 1989).

[3] P. Cova, Ph. D. Thesis, École Polytechnique de Montréal (1991).

[4] C. A. Tran, Ph.D. Thesis, École Polytechnique de Montréal (1992).

[5] A. Bensaada, Ph.D. Thesis, École Polytechnique de Montréal (1993).

[6] H. Marchand, M. A. Sc. Thesis, École Polytechnique de Montréal (1996).

[7] T. P. Pearsall, "Strained-Layer Superlattices" in *Semiconductors and Semimetals* **32** (Academic, San Diego, 1990), 1.

[8] R. Hull and J. C. Bean, "Principles and Concepts of Strained-Layer Epitaxy" in *Semiconductors and Semimetals* **33** (Academic, San Diego, 1991), 1.

[9] J. N. Stranski and L. Krastanov, Ber. Akad. Wiss. Wein **146**, 797 (1938).

[10] P. Desjardins, Ph.D. Thesis, École Polytechnique de Montréal (1996).

[11] By this, we mean the undeformed lattice constant of the material in the absence of any external stresses.

[12] Although minute, substrate deformation due to the presence of the strained epitaxial layer is detectable. Researchers at Sandia National Laboratories have recently commercialized a real-time measurement of wafer curvature, applicable for in-situ monitoring of the growth process. The measurement can resolve a radius of wafer curvature up to 4 km, making is sufficiently sensitive to detect the onset of strain relaxation. J. A. Floro and E. Chason, "Measuring Ge segregation by real-time stress monitoring during $Si_{1-x}Ge_x$ molecular beam epitaxy," Appl. Phys. Lett. **69**, 3830 (1996);

J. A. Floro, E. Chason and S. R. Lee, "Measurement of Stress Evolution During Thin Film Deposition," MRS Symposium Proceedings **406**, 491 (1996); E. Chason and J. A. Floro, "Real Time Measurement of Epilayer Strain Using a Simplified Wafer Curvature Technique," MRS Symposium Proceedings **428**, 499 (1996).

[13] R. Beanland, D.J. Dunstan and P.J. Goodhew, Adv. Phys. **45**, 87 (1996).

[14] E. T. Yu, J. O. McCaldin and T. C. McGill, "Band Offsets in Semiconductor Heterojunctions" in *Solid State Physics* **46** (Academic, Boston, 1992), 2.

[15] J.W. Matthews and A.E. Blakeslee, J. Cryst. Growth **27**, 118 (1974), J. Cryst. Growth **29**, 273 (1975).

[16] K. M. Chen, D. E. Jesson, S. J. Pennycook, M. Mostoller and T. Kaplan, "Step Instabilities: A New Kinietic Route to 3D Growth," Phys. Rev. Lett. **75**, 1582 (1995).

[17] J. E. Cunningham and K. W. Goosen, "Strain Balanced InGaAs/GaAsP Multiple Quantum Well Modulators at 1.06 μm," Proceedings of the 26th State-of-the-Art Program on Compound Semiconductors, Electrochemical Society Proceedings **97-1**, 41 (1997).

[18] J. Tersoff and F. K. Legoues, "Competing Relaxation Mechanisms in Strained Layers," Phys. Rev. Lett. **72**, 3570 (1994).

[19] MBE growth is limited by the surface kinetics whereas MOVPE growth may be limited by surface kinetics or by diffusion of precursors species through the boundary layer created by the viscous gas flow. The diffusion limited regime requires elevated thermal energies at the growth surface for efficient breakdown and incorporation of the precursor species onto the epitaxial layer.

[20] Since November 1997, we have been investigating the insertion of ternary InAsP and binary InAs strained layers in an InGaAsP index guiding layer for the realization of both coherent and incoherent emitters in the 0.8 - 0.95 eV range for optical telecommunications. Most of the initial work has been performed with InGaAsP/InP and InAs(P)/InP structures in order to perform separate investigations of the growth issues related to the production of high quality quaternary compounds and high quality

strained layers. Work on the strained layers confirms that for sufficiently high strains ($> \sim 1.8\ \%$), the layer structure becomes highly unstable to lateral thickness modulations and islanding. Nonetheless, the emission spectra from defect-free non-planar layers can be quite acceptable. This suggests interesting possibilities for devices using optical emission from a wide range of non-planar structures. The ongoing work is directed towards the production of InAs(P)/InGaAsP device layers and an investigation of the use of a wide range of growth conditions to exert some degree of control over the morphology of the highly-strained layers.

[21] O. Gurdal, M.-A. Hasan, M. R. Sardela, Jr., and J. E. Greene, "Growth of metastable $Ge_{1-x}Sn_x$/Ge strained layer superlattices on Ge(001)2×1 by temperature-modulated molecular beam epitaxy," Appl. Phys. Lett. **67**, 956 (1995).

[22] M. J. Antonell and C. R. Abernathy, "Growth of Tl-containing III-V Materials by Gas-Source Molecular Beam Epitaxy," Proceedings of the 26th State-of-the-Art Program on Compound Semiconductors, Electrochemical Society Proceedings **97-1**, 1 (1997).

[23] T. Uchida, H. Kurakake, H. Soda and S. Yamazaki, "A 1.3 μm Strained Quantum Well Laser on a Graded InGaAs Buffer with a GaAs Substrate," J. Electron. Mater. **25**, 581 (1996).

[24] E. A. Fitzgerald, D. G. Ast, Y. Ashizawa. S. Akbar and L. F. Eastman, "Dislocation structure, formation, and minority-carrier recombination in AlGaAs/InGaAs/GaAs heterojunction bipolar transistors," J. Appl. Phys. **64**, 2473 (1988).

[25] E. A. Fitzgerald, G. P. Watson, R. E. Proano, D. G. Ast, P. D. Kirchner, G. D. Pettit and J. M. Woodall, "Nucleation mechanisms and the elimination of misfit dislocations at mismatched interfaces by reduction in growth area," J. Appl. Phys. **65**, 2220 (1989).

[26] Paul F. Fewster, "X-ray analysis of thin films and multilayers," Rep. Prog. Phys. **59**, 1339 (1996).

[27] J. Hornstra and W.J. Bartels, J. Cryst. Growth **44,** 513 (1978).

[28] M.A.G. Halliwell, M.H. Lyons, S.T. Davey, M. Hockly, C.G. Tuppen and C.J. Gibbings, Semicond. Sci. Technol. **4**, 10 (1989).

[29] P.F. Fewster, Semicond. Sci. Technol. **8**, 1915 (1993).

[30] M.A.G. Halliwell, Appl. Phys. A**58**, 135 (1994).

[31] P. F. Fewster and C. J. Curling, "Composition and lattice-mismatch measurement of thin semiconductor layers by x-ray diffraction," J. Appl. Phys. **62**, 4154 (1987).

[32] S. R. Sloane, "Processing and Passivation Techniques for Fabrication of High-Speed InP/InGaAs/InP Mesa Photodetectors," Hewlett Packard Journal, 69 (October 1989).

[33] T. Kambayashi, C. Kitahara and K. Iga, "Chemical Etching of InP and GaInAsP for Fabricating Laser Diodes and Integrated Circuits," Japanese J. Appl. Phys. **19**, 79 (1985).

[34] S. Adachi, Y. Naguchi and H. Kawaguchi, "Chemical Etching of InGaAsP/InP DH Wafer," J. Electrochem. Soc. **129**, 1053 (1982).

[35] J. R. Flemish and K. A. Jones, "Selective Wet Etching of GaInP, GaAs and InP in Solutions of HCl, CH_3COOH, and H_2O_2," J. Electrochem. Soc. **140**, 844 (1993).

[36] P. H. L. Notten, "The Etching of InP in HCl Solutions: A Chemical Mechanism," J. Eletrochem. Soc. **131**, 2641 (1984).

[37] B. L. Sharma, "Ohmic Contacts to III-V Compound Semiconductors" in *Semiconductors and Semimetals* **15**, 1 (1981).

[38] V. Malina, U. Schade and K. Vogel, "Technological aspects of the preparation of Au-Zn ohmic contacts to p-type InP," Semicond. Sci. Technol. **9**, 49 (1994).

[39] J. B. Boos and W. Kruppa, "Low-resistance AuZn Gate Ohmic Contacts for InP JFETs," Solid-State Electron. **31**, 127 (1988).

[40] T. Clausen and O. Leistiko, "Metallurgical optimization for ohmic contacts to InP using conventional metallization schemes," Microelectronic Engineering **18**, 305 (1992).

[41] W. Tseng, A. Christou, H. Day, J. Davey and B. Wilkins, "Ohmic contacts to lightly doped n and p indium phosphide surfaces," J. Vac. Sci. Technol. **19**, 623 (1981).

[42] H. B. Harrison and G. K. Reeves, "Assessing Ohmic Contacts," Materials Research Society Symposium Proceedings **260**, 31 (1992).

[43] E. Kuphal, "Low Resistance Ohmic Contacts to n- and p-InP," Solid-State Electron. **24**, 69 (1981).

[44] R. F. Leonard and W. F. Cordes, III, "New High Speed Positive Resist for Wafer Steppers," SPIE Optical Microlithography Technology for the Mid-1980's Seminar, Santa Clara CA, March 31 and April 1 (1982).

[45] N. S. Fatemi and V. G. Weizer, "The Achievement of Low Contact Resistance to Indium Phosphide: the Roles of Ni, Au, Ge and Combinations Thereof," Materials Research Society Symposium Proceedings **260**, 537 (1992).

[46] O. Wada and O. Ueda, "Reliable Metallization for InP-Based Devices and OEIC's," MRS Symposium Proceedings **184**: *Degradation Mechanisms in III-V Compound Semiconductor Devices and Structures*, 209 (1990).

[47] A. Katz, B. E. Weir and W. C. Dautremont-Smith, "Au/Pt/Ti contacts to p-$In_{0.53}Ga_{0.47}As$ and n-InP layers formed by a single metallization common step and rapid thermal processing," J. Appl. Phys. **68**, 1123 (1990).

[48] G. Stareev and H. Kunzel, "Tunneling behavior of extremely low resistance nonalloyed Ti/Pt/Au contacts to n(p)-InGaAs and n-InAs/InGaAs," J. Appl. Phys. **74**, 7562 (1993).

[49] Y. Ashizawa, C. Nozaki, T. Noda and A. Sasaki, "Thermal Stability of Interfaces Between Metals and InP-Based Materials," J. Electron. Mater. **25**, 715 (1996).

[50] V. G. Weizer and N. S. Fatemi, J. Electron. Mater. **25**, 755 (1996).

[51] E. F. Schubert, S. W. Downey, C. Pinzone and A. B. Emerson, "Evidence of very strong inter-epitaxial-layer diffusion in Zn-doped GaInPAs/InP structures," Appl. Phys. **A60**, 525 (1995).

[52] V. Swaminathan, C. L. Reynolds, Jr., and M. Geva, "Zn diffusion behavior in InGaAsP/InP capped buried heterostructures," Appl. Phys. Lett. **66**, 2685 (1995).

Chapter 3 - Detailed balance efficiency limit in quantum well solar cells

[1] K. W. J. Barnham and G. Duggan, "A new approach to high-efficiency multi-band-gap solar cells," J. Appl. Phys. **67**, 3490 (1990).

[2] K. W. J. Barnham, B. Braun, J. Nelson, M. Paxman, C. Button and J. S. Roberts, "Short-circuit and energy efficiency enhancement in a low-dimensional structure photovoltaic device," Appl. Phys. Lett. **59**, 135 (1991).

[3] K. W. J. Barnham, J. Barnes, G. Haarpaintner, J. Nelson, M. Paxman., T. Foxon and J. Roberts, "Quantum-Well Solar Cells," MRS Bull., 51 (October 1993).

[4] R. Corkish and M. A. Green, "Recombination of Carriers in Quantum Well Solar Cells," IEEE Proceedings of the Photovoltaic Specialists Conference, 675 (1993).

[5] W. Shockley and H. J. Queisser, "Detailed Balance Limit of Efficiency of p-n Junction Solar Cells", J. Appl. Phys. **32**, 510 (1961).

[6] C. H. Henry, "Limiting efficiencies of ideal single and multiple energy gap terrestrial solar cells," J. Appl. Phys. **51**, 4494 (1980).

[7] G. L. Araujo and A. Marti, Appl. Phys. Lett. **66**, 894 (1995)

[8] M. Paxman, J. Nelson, B. Braun, J. Connolly, K. W. J. Barnham, C. T. Foxon, and J. S. Roberts, "Modelling the spectral response of the quantum well solar cell," J. Appl. Phys. **74**, 614 (1993).

Chapter 4 - Strain and relaxation in multiple quantum well stacks

[1] A.R. Adams, Electron. Lett. **22**, 249 (1986).

[2] E. Yablonovitch and E.O. Kane, J. Lightwave Technol. **6**, 1292 (1988).

[3] A. Kasukawa, T. Namegaya, T. Fukushima, N. Iwai and T. Kikuta, IEEE J. Quantum Electron. **29**, 1528 (1993).

[4] M. Yamamoto, N. Yamamoto and J. Nakano, IEEE J. Quantum Electron. **30**, 554 (1994).

[5] C.A. Tran, R.A. Masut, P. Cova, J.L. Brebner and R. Leonelli, J. Cryst. Growth **121**, 365 (1992).

[6] R. Hull and J.C. Bean, in *Semiconductors and Semimetals* **33** (Academic, San Diego, 1991), p. 1.

[7] R. Beanland, D.J. Dunstan and P.J. Goodhew, Adv. Phys. **45**, 87 (1996).

[8] K.R. Linga, G.H. Olsen, V.S. Ban, A.M. Joshi and W.F. Kosonocky, J. Lightwave Technol. **10**, 1050 (1992).

[9] D.S. Kim, S.R. Forrest, G.H. Olsen, M.J. Lange, R.U. Martinelli and N.J. Di Giuseppe, IEEE Photonics Technol. Lett. **7**, 911 (1995).

[10] S.N.G. Chu, S. Nakahara, M.E. Twigg, L.A. Koszi, E.J. Flynn, A.K. Chin, B.P. Segner and W.D. Johnston, Jr., J. Appl. Phys. **63**, 611 (1988).

[11] B.C. de Cooman, C.W.T. Bulle-Lieuwma, J.A. de Poorter and W. Nijman, J. Appl. Phys. **67**, 3919 (1990).

[12] P.G. Eliseev, *Reliability Problems of Semiconductor Lasers* (Nova Science, New York, 1991).

[13] S.N.G. Chu, MRS Bull., 43 (December 1993).

[14] Y. Ashizawa, S. Akbar, W.J. Schaff, L.F. Eastman, E.A. Fitzgerald and D.G. Ast, J..Appl. Phys. **64**, 4065 (1988).

[15] Y. Uchida, H. Kakibayashi and S. Goto, J. Appl. Phys. **74**, 6720 (1993).

[16] R. Hull, J.C. Bean, F. Cerdeira, A.T. Fiory and J.M. Gibson, Appl. Phys. Lett. **48**, 56 (1986).

[17] T.K. Woodward, T. Sizer II and and T.H. Chiu, App. Phys. Lett. **58**, 1366 (1991).

[18] T.K. Woodward, T.H. Chiu and T. Sizer II, App. Phys. Lett. **60**, 2846 (1992).

[19] D.A.B. Miller, D.S. Chemla, T.C. Damen, A.C. Gossard, W. Wiegmann, T.H. Wood and C.A. Burrus, Phys. Rev. B **32**, 1043 (1985).

[20] M. Beaudoin, A. Bensaada, R. Leonelli, P. Desjardins, R.A. Masut, L. Isnard, A. Chennouf and G. L'Espérance, Phys. Rev. B **53**, 1990 (1996).

[21] P. Desjardins, M. Beaudoin, R. Leonelli, G. L'Espérance and R.A. Masut, J. Appl. Phys. **80**, 846 (1996).

[22] J.Y. Marzin, J.M. Gérard, P. Voisin and J.A. Brum, in *Semiconductors and Semimetals* **32** (Academic, San Diego, 1990), p. 55.

[23] C.A. Tran, J.T. Graham, J.L. Brebner and R.A. Masut, J. Electron. Mater. **23**, 1291 (1994).

[24] The epitaxial layers for mod02 consist of: 1200 nm p-doped cap, 360 nm undoped spacer, 50 periods of 11.9 nm InAsP / 11.9 nm InP, 360 nm undoped spacer, and 1200 nm n-doped buffer layer grown on a S-doped ($\sim 2\times10^{18}$ cm^{-3}) InP(001) substrate.

[25] J.R. Flemish and K.A. Jones, J. Electrochem. Soc. **140**, 844 (1993).

[26] P.F. Fewster, Phillips J. Research **45**, 620 (1984).

[27] J. Hornstra and W.J. Bartels, J. Cryst. Growth **44**, 513 (1978).

[28] M.A.G. Halliwell, M.H. Lyons, S.T. Davey, M. Hockly, C.G. Tuppen and C.J. Gibbings, Semicond. Sci. Technol. **4**, 10 (1989).

[29] P.F. Fewster, Semicond. Sci. Technol. **8**, 1915 (1993).

[30] M.A.G. Halliwell, Appl. Phys. A **58**, 135 (1994).

[31] The calculation has been performed assuming misfit dislocations of the 60° type and using the Fitzgerald formulation of the Matthews and Blakeslee model. See Refs. 7 and 32. The critical thicknesses obtained here differ from those in Ref. 21, where a smaller value of in-plane component of the Burgers vector was used.

[32] J.W. Matthews and A.E. Blakeslee, J. Cryst. Growth **27**, 118 (1974), J. Cryst. Growth **29**, 273 (1975).

[33] K.L. Kavanagh, M.A. Capano, L.W. Hobbs, J.C. Barbour, P.M.J. Marée, W. Schaff, J.W. Mayer, D. Pettit, J.M. Woodall, J.A. Stroscio and R.M. Feenstra, J. Appl. Phys. **64**, 4843 (1988).

[34] R.Y.-F. Yip *et al.*, (unpublished).

[35] K.W. Goossen, J.E. Cunningham and W.Y. Jan, Appl. Phys. Lett. **57**, 2582 (1990).

[36] J. Lee, E.S. Koteles and M.O. Vassell, Phys. Rev. B **33**, 5512 (1986).

[37] M. Sugawara, T. Fujii, S. Yamazaki and K. Nakajima, Phys. Rev. B **42**, 9587 (1990).

[38] G. Bastard, *Wave Mechanics Applied to Semiconductor Heterostructures* (les Éditions de Physique, Les Ulis Cedex, France, 1988).

[39] J. Tersoff, Phys. Rev. B **30**, 4874 (1984).

[40] G.E. Pikus and G.L. Bir, Sov. Phys. Solid State **1**, 136 (1959); **1**, 1502 (1960).

[41] A. Bensaada, A. Chennouf, R.W. Cochrane, J.T. Graham, R. Leonelli and R.A. Masut, J. Appl. Phys. **75**, 3024 (1994).

[42] F.H. Pollak, in *Semiconductors and Semimetals* **32** (Academic, San Diego, 1990), p. 17.

[43] A. M. Fox, D.A.B. Miller, G. Livescu, J.E. Cunningham and W.Y. Jan, IEEE J. Quantum Electron. **27**, 2281 (1991).

[44] G. Bastard, E.E. Mendez, L.L. Chang, and L. Esaki, Phys. Rev. B **28**, 3241 (1983).

[45] T. Yamanaka, K, Wakita, K. Yokoyama, Appl. Phys. Lett. **65**, 1540 (1994).

[46] T. Ikeda and H. Ishikawa, IEEE J. Quantum Electron. **32**, 284 (1996).

[47] I. Kotaka, K. Wakita, K. Kawano, M. Asai and M. Naganuma, Electron. Lett. **27**, 2163 (1991).

[48] W.L. Bloss, J. Appl. Phys. **65**, 4789 (1989).

[49] H. Yamazaki, Y. Sakata, M. Yamaguchi, Y. Inomoto and K. Komatsu, Electron. Lett. **32**, 109 (1996).

[50] M. Aoki, M. Suzuki, M. Takahashi, H. Sano, T. Ido, T. Kawano and A. Takai, Electron. Lett. **28**, 1157 (1992).

[51] U. Koren, B.I. Miller, T.L. Koch, G. Eisenstein, R.S. Tucker, I. Bar-Joseph and D.S. Chemla, Appl. Phys. Lett. **51**, 1132 (1987).

[52] E.J. Austin and M. Jaros, Phys. Rev. B **31**, 5569 (1985).

[53] J. Singh, Appl. Phys. Lett. **48**, 434 (1985).

[54] M.-E. Pistol and D. Gershoni, Phys. Rev. B **50**, 11738 (1994).

Chapter 5 - Band alignment engineering for the quantum-confined Stark effect

[1] D. A. B. Miller, D. S. Chemla, T. C. Damen, A. C. Gossard, W. Wiegmann, T. H. Wood, and C. A. Burrus, Phys. Rev. B **32**, 1043 (1985).

[2] D. M. Adams, C. Rolland, N. Puetz, R. S. Moore, F. R. Shepherd, H. B. Kim and S. Bradshaw, Electron. Lett. **32**, 485 (1996).

[3] M. Aoki, M. Suzuki, M Takahashi, H. Sano, T. Ido, T. Kawano and A. Takai, Electron. Lett. **28**, 1157 (1992).

[4] A. V. Krishnamoorthy, A. L. Lentine, K. W. Goosen, J. A. Walker, T. K. Woodward, J. E. Ford, G. F. Aplin, L. A. D'Asaro, S. P. Hui, B. Tseng, R. Leibenguth, D. Kossives, D. Dahringer, L. M. F. Chirovsky and D. A. B. Miller, IEEE Photon. Technol. Lett. **7**, 1288 (1995).

[5] Anthony L. Lentine and David A. B. Miller, IEEE J. Quant. Electron. **29**, 655 (1993).

[6] E. E. Mendez, G. Bastard, L. L. Chang, L. Esaki, H. Morkoc and R. Fischer, Phys. Rev. B **26**, 7101 (1982).

[7] R. Y.-F. Yip, A. Aït-Ouali, A. Bensaada, P. Desjardins, M. Beaudoin, L. Isnard, J. L. Brebner, J. F. Currie and R. A. Masut, J. Appl. Phys. **81**, 1905 (1997).

[8] W. L. Bloss, J. Appl. Phys. **65**, 4789 (1989).

[9] T. Yamanaka, K. Wakita and K. Yokoyama, Appl. Phys. Lett. **65**, 1540 (1994).

[10] T. Ikeda and H. Ishikawa, IEEE J. Quant. Electron. **32**, 284 (1996).

[11] R. Y.-F. Yip and R. A. Masut, J. Appl. Phys. **82**, 1976 (1997).

[12] Typographic correction: L_0 in equations (A4) and (A5) of Ref. 7 should be replaced by $L_0/2$.

[13] G. Bastard, E. E. Mendez, L. L. Chang and L. Esaki, Phys. Rev. B **28**, 3241 (1983).

[14] This requires some qualification as there are efforts to achieve a large degree of polarization insensitivity in external optical modulators based on the QCSE (e.g. A. Ougazzaden and F. Devaux, Appl. Phys. Lett. **69**, 4131 (1996)). Such a modulator is

appropriate when the polarization of the input radiation, which may have traveled some distance via an optical fiber, is unknown. In our case, the discussion is restricted to the case of TE polarization which is appropriate for optical modulators that are integrated on-chip with the semiconductor laser. As such, we are primarily interested in the n = 1 electron-heavy hole transition which is dominant when compressive biaxial strain in the (001) plane shifts the light hole band to higher energies.

[15] An exact treatment of the tunneling and barrier penetration in quantum well structures within the effective mass approximation requires accounting for the different well and barrier effective mass terms. However, the well and barrier effective masses are similar in all the practical cases that we consider. For leading order behavior, we may neglect the difference between well and barrier effective mass terms.

[16] S. Adachi, *Physical Properties of III-V Semiconductor Compounds* (Wiley, New York, 1992).

[17] R. H. Fowler and L. Nordheim, Proc. Roy. Soc. (London) A **119**, 173 (1928).

[18] C. B. Duke, *Solid State Phys. Suppl.* **10** (Academic, New York, 1969).

[19] K. H. Grundlach, Solid-State Electron. **9**, 949 (1966).

[20] A. T. Fromhold, Jr., *Quantum Mechanics for Applied Physics and Engineering* (Academic, New York, 1981), 237.

[21] J. Y. Marzin, J. M. Gérard, P. Voisin, and J.A. Brum, in *Semiconductors and Semimetals* **32** (Academic, San Diego, 1990), 55.

[22] G. Bastard, *Wave Mechanics Applied to Semiconductor Heterostructures* (les Éditions de Physique, Les Ulis Cedex, France, 1988).

[23] M. Beaudoin, A. Bensaada, R. Leonelli, P. Desjardins, R. A. Masut, L. Isnard, A. Chennouf and G. L'Espérance, Phys. Rev. B **53,** 1990 (1996).

[24] V. G. Weizer and N. S. Fatemi, J. Electron. Mater. **25**, 755 (1996).

[25] The vertical scales in each of the photocurrent spectra of Figure 5.5 have been obtained by linearly normalizing the heights of the main e1-hh1 peaks in the 0V applied reverse bias curves to the heights of the same peaks in the optical absorption spectra measured

by detecting the true transmission signal with the BOMEM DA3 interferometer (for an example of these absorption spectra, see Ref. 7). This procedure is appropriate when $\alpha d \ll 1$, where $e^{-\alpha d}$ is the attenuation factor due to photo-absorption in the material and d is the total path length of the radiation through the quantum well material. In our characterization of the material, the incident radiation was surface normal and d is simply the total thickness of quantum well material. The linewidths of the optical transitions measured by photocurrent and by optical absorption are similar in most cases. But, writing the Taylor expansion for $e^{-\alpha d}$ shows that the photocurrent measurement always overestimates the true absorption linewidth. We have noticed that this 'error' becomes larger as barrier heights decrease, likely due to the enhanced sensitivity of the photo-absorption response and photo-charge collection in low barrier MQWSs to both built-in and applied fields.

[26] X. B. Mei, W. G. Bi, C. W. Tu, L. J. Chou and K. C. Hsieh, J. Vac. Sci. Technol. B **14**, 2327 (1996).

[27] S. Nojima, Y. Kawamura, K. Wakita and O. Mikami, J. Appl. Phys. **64**, 2795 (1988).

[28] M. K. Chin, IEEE Photon. Technol. Lett. **4**, 726 (1992).

[29] O. Mitomi, I. Kotaka, K. Wakita, S. Nojima, K. Kawano, Y. Kawamura and H. Asai, Appl. Optics **31**, 2030 (1992).

[30] T. H. Wood, J. Z. Pastalan, C. A. Burrus, Jr., B. C. Johnson, B. I. Miller, J. L. deMiguel, U. Koren, M. G. Young, Appl. Phys. Lett. **57**, 1081 (1990).

[31] A. M. Fox, D. A. B. Miller, G. Livescu, J. E. Cunningham, and W. Y. Jan, IEEE J. Quantum Electron. **27**, 2281 (1991).

[32] F. Devaux, S. Chelles, A. Ougazzaden, A. Mircea and J. C. Harmand, Semicond. Sci. Technol. **10**, 887 (1995).

[33] K. W. Goossen, J. E. Cunningham and W. Y. Jan, Appl. Phys. Lett. **57**, 2582 (1990).

[34] A. Franciosi and C. G. Van de Walle, Surf. Sci. Rep. **25**, 1 (1996).

[35] J. Tersoff and C. G. Van de Walle, Phys. Rev. Lett. **59**, 946 (1987).

[36] M. P. C. M. Krijn, Semicond. Sci. Technol. **6**, 27 (1991).

[37] T. Ishikawa and J. E. Bowers, IEEE J. Quant. Electron. **30**, 562 (1994).

[38] C. G. Van de Walle, Phys. Rev. B **39**, 1871 (1989).

[39] J. Tersoff, Phys. Rev. B **30**, 4874 (1984); J. Tersoff, in *Heterojunction Band Discontinuities, Physics and Device Applications*, (F. Capasso and G. Margaritondo, eds., Elsevier, Amsterdam, 1987), 3.

[40] C. Tejedor and F. Flores, J. Phys. C **11**, L19 (1978).

[41] J. E. Cunningham and K. W. Goossen, Electrochem. Soc. Proc. **97-1** (SOTAPOCS-26), 41 (1997).

[42] J. F. Carlin, A. V. Syrbu, C. A. Berseth, J. Behrend, A. Rudra and E. Kapon, Appl. Phys. Lett. **71**, 13 (1997).

[43] P. Desjardins, M. Beaudoin, R. Leonelli, G. L'Espérance, and R. A. Masut, J. Appl. Phys. **80**, 846 (1996).

[44] R. C. Miller, A. C. Gossard, D. A. Kleinman and O. Munteanu, Phys. Rev. B **29**, 3740 (1984).

[45] E. T. Yu, J. O. McCaldin and T. C. McGill, in *Solid State Physics* **46** (Academic, San Diego, 1994), 33.

[46] G. Duggan, in *Heterojunction Band Discontinuities, Physics and Device Applications*, (F. Capasso and G. Margaritondo, eds., Elsevier, Amsterdam, 1987), 207.

[47] R. P. Schneider, Jr. and B. W. Wessels, J. Electron. Mater. **20**, 1117 (1991): $\Delta E_V \sim 0.25\Delta E_G$.

8 BIBLIOGRAPHY

S. ADACHI, Y. NAGUCHI and H. KAWAGUCHI, "Chemical Etching of InGaAsP/InP DH Wafer," *J. Electrochem. Soc.* **129**, 1053 (1982).

S. ADACHI, *Physical Properties of III-V Semiconductor Compounds* (Wiley, New York, 1992).

A. R. ADAMS, "Band Structure Engineering for Low-Threshold High-Efficiency Semiconductor Lasers," *Electron. Lett.* **22**, 249 (1986).

D. M. ADAMS, C. ROLLAND, N. PUETZ, R. S. MOORE, F. R. SHEPHERD, H. B. KIM and S. BRADSHAW, "Mach-Zender modulator integrated with a gain-coupled DFB laser for 10 Gbit/s, 100km NDSF transmission at 1.55 μm," *Electron. Lett.* **32**, 485 (1996).

M. J. ANTONELL and C. R. ABERNATHY, "Growth of Tl-containing III-V Materials by Gas-Source Molecular Beam Epitaxy," Proceedings of the 26th State-of-the-Art Program on Compound Semiconductors, *Proc. Electrochem. Soc.* **97-1**, 1 (1997).

M. AOKI, M. SUZUKI, M. TAKAHASHI, H. SANO, T. IDO, T. KAWANO and A. TAKAI, "High-Speed (10 Gbit/s) and Low-Drive-Voltage (1 V Peak to Peak) InGaAs/InGaAsP MQW Electroabsorption-Modulator Integrated DFB Laser with Buried Heterostructure," *Electron. Lett.* **28**, 1157 (1992).

G. L. ARAUJO and A. MARTI, "Electroluminescence coupling in multiple quantum well diodes and solar cells," *Appl. Phys. Lett.* **66**, 894 (1995).

Y. ASHIZAWA, S. AKBAR, W. J. SCHAFF, L. F. EASTMAN, E. A. FITZGERALD and D. G. AST, "Influence of lattice misfit on heterojunction bipolar transistors with lattice-mismatched InGaAs bases," *J. Appl. Phys.* **64**, 4065 (1988).

Y. ASHIZAWA, C. NOZAKI, T. NODA and A. SASAKI, "Thermal Stability of Interfaces Between Metals and InP-Based Materials," *J. Electron. Mater.* **25**, 715 (1996).

E. J. AUSTIN and M. JAROS, "Electronic structure of an isolated GaAs-GaAlAs quantum well in a strong electric field," *Phys. Rev. B* **31**, 5569 (1985).

K. W. J. BARNHAM and G. DUGGAN, "A new approach to high-efficiency multi-band-gap solar cells, "*J. Appl. Phys.* **67**, 3490 (1990).

K. W. J. BARNHAM, B. BRAUN, J. NELSON, M. PAXMAN, C. BUTTON and J. S. ROBERTS, "Short-circuit and energy efficiency enhancement in a low-dimensional structure photovoltaic device," *Appl. Phys. Lett.* **59**, 135 (1991).

K. W. J. BARNHAM, J. BARNES, G. HAARPAINTNER, J. NELSON, M. PAXMAN., T. FOXON and J. ROBERTS, "Quantum-Well Solar Cells," *MRS Bull.*, 51 (October 1993).

G. BASTARD, E. E. MENDEZ, L. L. CHANG, and L. ESAKI, "Variational calculations on a quantum well in an electric field, "*Phys. Rev. B* **28**, 3241 (1983).

G. BASTARD, *Wave Mechanics Applied to Semiconductor Heterostructures* (les Éditions de Physique, Les Ulis Cedex, France, 1988).

R. BEANLAND, D. J. DUNSTAN and P. J. GOODHEW, "Plastic relaxation and relaxed buffer layers for semiconductor epitaxy, "*Adv. Phys.* **45**, 87 (1996).

M. BEAUDOIN, A. BENSAADA, R. LEONELLI, P. DESJARDINS, R.A. MASUT, L. ISNARD, A. CHENNOUF and G. L'ESPÉRANCE, "Self-consistent determination of the band offsets in $InAs_xP_{1-x}$/InP strained-layer quantum wells and the bowing parameter of bulk $InAs_xP_{1-x}$," *Phys. Rev. B* **53,** 1990 (1996).

A. BENSAADA, "Cristallogénèse et caractérisation des hétérostructures contraintes $Ga_xIn_{1-x}P$/InP ($0 \leq x < 0.25$)," *Ph.D. Thesis*, École Polytechnique de Montréal (1993).

A. BENSAADA, A. CHENNOUF, R. W. COCHRANE, J. T. GRAHAM, R. LEONELLI and R. A. MASUT, "Misfit strain, relaxation, and band-gap shift in $Ga_xIn_{1-x}P$/InP epitaxial layers," *J. Appl. Phys.* **75**, 3024 (1994).

WALTER L. BLOSS, "Electric field dependence of quantum-well eigenstates," *J. Appl. Phys.* **65**, 4789 (1989).

J. B. BOOS and W. KRUPPA, "Low-resistance AuZn Gate Ohmic Contacts for InP JFETs," *Solid-State Electron.* **31**, 127 (1988).

F. CAPASSO and G. MARGARITONDO, eds., *Heterojunction Band Discontinuities, Physics and Device Applications*, (Elsevier, Amsterdam, 1987).

J. F. CARLIN, A. V. SYRBU, C. A. BERSETH, J. BEHREND, A. RUDRA and E. KAPON, "Low threshold 1.55 μm wavelength InAsP/InGaAsP strained multiquantum well laser diode grown by chemical beam epitaxy," *Appl. Phys. Lett.* **71**, 13 (1997).

E. CHASON and J. A. FLORO, "Real Time Measurement of Epilayer Strain Using a Simplified Wafer Curvature Technique," *MRS Symposium Proceedings* **428**, 499 (1996).

K. M. CHEN, D. E. JESSON, S. J. PENNYCOOK, M. MOSTOLLER and T. KAPLAN, "Step Instabilities: A New Kinietic Route to 3D Growth," *Phys. Rev. Lett.* **75**, 1582 (1995).

M. K. CHIN, "On the Figures of Merit for Electroabsorption Waveguide Modulators," *IEEE Photon. Technol. Lett.* **4**, 726 (1992).

S. N. G. CHU, S. NAKAHARA, M. E. TWIGG, L. A. KOSZI, E. J. FLYNN, A. K. CHIN, B. P. SEGNER and W. D. JOHNSTON, Jr., "Defect mechanisms in degradation of 1.3-μm wavelength channeled-substrate buried heterstructure lasers," *J. Appl. Phys.* **63**, 611 (1988).

S. N. G. CHU, *MRS Bull.*, 43 (December 1993).

T. CLAUSEN and O. LEISTIKO, "Metallurgical optimization for ohmic contacts to InP using conventional metallization schemes," *Microelectronic Engineering* **18**, 305 (1992).

R. CORKISH and M. A. GREEN, "Recombination of Carriers in Quantum Well Solar Cells," *IEEE Proc. Photovoltaic Spec. Conf.*, 675 (1993).

P. COVA, "Croissance et caractérisation de InP fabriqué par LP-MOVPE," Ph. D. Thesis, École Polytechnique de Montréal (1991).

J. E. CUNNINGHAM and K. W. GOOSEN, "Strain Balanced InGaAs/GaAsP Multiple Quantum Well Modulators at 1.06 μm,"Proceedings of the 26th State-of-the-Art Program on Compound Semiconductors, *Proc. Electrochem. Soc.* **97-1**, 41 (1997).

B. C. DE COOMAN, C. W. T. BULLE-LIEUWMA, J. A. DE POORTER and W. NIJMAN, "The effect of interstitial Frank partial dislocations on the gradual degradation of 1.3-μm double-channel planar buried heterostructure laser diodes," *J. Appl. Phys.* **67**, 3919 (1990).

P. DESJARDINS, M. BEAUDOIN, R. LEONELLI, G. L'ESPÉRANCE and R.A. MASUT, "Structural and optical properties of strain-relaxed InAsP/InP heterostructures grown by metalorganic vapor phase epitaxy on InP(001) using tertiarybutylarsine," *J. Appl. Phys.* **80**, 846 (1996).

P. DESJARDINS, "Caractérisation et modélisation de la croissance épitaxiale et de la relaxation des contraintes dans les hétérostructures semi-conductrices," Ph.D. Thesis, École Polytechnique de Montréal (1996).

F. DEVAUX, S. CHELLES, A. OUGAZZADEN, A. MIRCEA and J. C. HARMAND, "Electroabsorption modulators for high-bit-rate optical communications: a comparison of strained InGaAs/InAlAs and InGaAsP/InGaAsP MQW," *Semicond. Sci. Technol.* **10**, 887 (1995).

C. B. DUKE, "Tunneling in Solids," *Solid State Phys. Suppl.* **10** (Academic, New York, 1969).

P. G. ELISEEV, *Reliability Problems of Semiconductor Lasers* (Nova Science, New York, 1991).

N. S. FATEMI and V. G. WEIZER, "The Achievement of Low Contact Resistance to Indium Phosphide: the Roles of Ni, Au, Ge and Combinations Thereof," *Proc. Materials Research Society Symp.* **260**, 537 (1992).

E. A. FITZGERALD, D. G. AST, Y. ASHIZAWA. S. AKBAR and L. F. EASTMAN, "Dislocation structure, formation, and minority-carrier recombination in AlGaAs/InGaAs/GaAs heterojunction bipolar transistors," *J. Appl. Phys.* **64**, 2473 (1988).

E. A. FITZGERALD, G. P. WATSON, R. E. PROANO, D. G. AST, P. D. KIRCHNER, G. D. PETTIT and J. M. WOODALL, "Nucleation mechanisms and the elimination of misfit dislocations at mismatched interfaces by reduction in growth area,"*J. Appl. Phys.* **65**, 2220 (1989).

J. A. FLORO and E. CHASON, "Measuring Ge segregation by real-time stress monitoring during $Si_{1-x}Ge_x$ molecular beam epitaxy," *Appl. Phys. Lett.* **69**, 3830 (1996).

J. A. FLORO, E. CHASON and S. R. LEE, "Measurement of Stress Evolution During Thin Film Deposition," *MRS Symposium Proceedings* **406**, 491 (1996).

P. F. FEWSTER, *Phillips J. Research* **45**, 620 (1984).

P. F. FEWSTER and C. J. CURLING, "Composition and lattice-mismatch measurement of thin semiconductor layers by x-ray diffraction," *J. Appl. Phys.* **62**, 4154 (1987).

P. F. FEWSTER, "X-ray diffraction from low-dimensional structures," *Semicond. Sci. Technol.* **8**, 1915 (1993).

PAUL F. FEWSTER, "X-ray analysis of thin films and multilayers," *Rep. Prog. Phys.* **59**, 1339 (1996).

J. R. FLEMISH and K. A. JONES, "Selective Wet Etching of GaInP, GaAs and InP in Solutions of HCl, CH_3COOH, and H_2O_2," *J. Electrochem. Soc.* **140**, 844 (1993).

R. H. FOWLER and L. NORDHEIM, *Proc. Roy. Soc. (London) A* **119**, 173 (1928).

A. M. FOX, D. A. B. MILLER, G. LIVESCU, J. E. CUNNINGHAM and W. Y. JAN, "Quantum Well Carrier Sweep Out: Relation to Electroabsorption and Exciton Saturation," *IEEE J. Quant. Electron.* **27**, 2281 (1991).

A. FRANCIOSI and C. G. VAN DE WALLE, "Heterojunction band offset engineering," *Surf. Sci. Rep.* **25**, 1 (1996).

A. T. FROMHOLD, Jr., *Quantum Mechanics for Applied Physics and Engineering* (Academic, New York, 1981), 237.

K. W. GOOSSEN, J. E. CUNNINGHAM and W. Y. JAN, "Excitonic electroabsorption in extremely shallow quantum wells," *Appl. Phys. Lett.* **57**, 2582 (1990).

K. H. GRUNDLACH, "Zur Berechnung des Tunnelstroms durch eine Trapezförmige Potentialstufe," *Solid-State Electron.* **9**, 949 (1966).

O. GURDAL, M.-A. HASAN, M. R. SARDELA, Jr., and J. E. GREENE, "Growth of metastable $Ge_{1-x}Sn_x/Ge$ strained layer superlattices on Ge(001)2×1 by temperature-modulated molecular beam epitaxy," *Appl. Phys. Lett.* **67**, 956 (1995).

M. A.G. HALLIWELL, M.H. LYONS, S.T. DAVEY, M. HOCKLY, C.G. TUPPEN and C.J. GIBBINGS, "Estimation of percentage relaxation in $Si/Si_{1-x}Ge_x$ strained-layer superlattices," *Semicond. Sci. Technol.* **4**, 10 (1989).

M. A.G. HALLIWELL, "Practical interpretation of x-ray rocking curves from semiconductor heteroepitaxial layers," *Appl. Phys. A* **58**, 135 (1994).

H. B. HARRISON and G. K. REEVES, "Assessing Ohmic Contacts," *Proc. Materials Research Society Symp.* **260**, 31 (1992).

C. H. HENRY, "Limiting efficiencies of ideal single and multiple energy gap terrestrial solar cells," *J. Appl. Phys.* **51**, 4494 (1980).

J. HORNSTRA and W.J. BARTELS, *J. Cryst. Growth* **44,** 513 (1978).

R. HULL, J.C. BEAN, F. CERDEIRA, A.T. FIORY and J.M. GIBSON, "Stability of semiconductor strained-layer superlattices," *Appl. Phys. Lett.* **48,** 56 (1986).

R. HULL and J. C. BEAN, "Principles and Concepts of Strained-Layer Epitaxy" in *Semiconductors and Semimetals* **33** (Academic, San Diego, 1991), 1.

T. IKEDA and H. ISHIKAWA, "Analysis of the Attenuation Ratio of MQW Optical Intensity Modulator for 1.55 μm Wavelength Taking Account of Electron Wave Function Leakage," *IEEE J. Quant. Electron* **32,** 284 (1996).

T. ISHIKAWA and J. E. BOWERS, "Band Lineup and In-Plane Effective Mass of InGaAsP or InGaAlAs on InP Strained-Layer Quantum Well," *IEEE J. Quant. Electron.* **30**, 562 (1994).

T. KAMBAYASHI, C. KITAHARA and K. IGA, "Chemical Etching of InP and GaInAsP for Fabricating Laser Diodes and Integrated Circuits," *Jap. J. Appl. Phys.* **19**, 79 (1985).

A. KASUKAWA, T. NAMEGAYA, T. FUKUSHIMA, N. IWAI and T. KIKUTA, "1.3 μm $InAs_yP_{1-y}$ - InP Strained-Layer Quantum-Well Laser Diodes Grown by Metalorganic Chemical Vapor Deposition," *IEEE J. Quant. Electron.* **29**, 1528 (1993).

A. KATZ, B. E. WEIR and W. C. DAUTREMONT-SMITH, "Au/Pt/Ti contacts to p-$In_{0.53}Ga_{0.47}As$ and n-InP layers formed by a single metallization common step and rapid thermal processing," *J. Appl. Phys.* **68**, 1123 (1990).

K. L. KAVANAGH, M. A. CAPANO, L. W. HOBBS, J. C. BARBOUR, P. M. J. MARÉE, W. SCHAFF, J. W. MAYER, D. PETTIT, J. M. WOODALL, J. A. STROSCIO and R. M. FEENSTRA, "Asymmetries in dislocation densities, surface morphology, and strain of GaInAs/GaAs single heterolayers," *J. Appl. Phys.* **64**, 4843 (1988).

D. S. KIM, S. R. FORREST, G. H. OLSEN, M. J. LANGE, R. U. MARTINELLI and N. J. DI GIUSEPPE, "Avalanche Gain in $InAs_yP_{1-y}$ $(0.1 < y < 0.3)$ Photodetectors," *IEEE Photonics Technol. Lett.* **7**, 911 (1995).

U. KOREN, B. I. MILLER, T. L. KOCH, G. EISENSTEIN, R. S. TUCKER, I. BAR-JOSEPH and D. S. CHEMLA, "Low-loss InGaAs/InP multiple quantum well optical electroabsorption waveguide modulator, "*Appl. Phys. Lett.* **51**, 1132 (1987).

I. KOTAKA, K. WAKITA, K. KAWANO, M. ASAI and M. NAGANUMA, "High-Speed and Low-Drive-Voltage InGaAs/InAlAs Multiquantum Well Optical Modulators," *Electron. Lett.* **27**, 2162 (1991).

M. P. C. M. KRIJN, "Heterojunction band offsets and effective masses in III-V quaternary alloys," *Semicond. Sci. Technol.* **6**, 27 (1991).

A. V. KRISHNAMOORTHY, A. L. LENTINE, K. W. GOOSEN, J. A. WALKER, T. K. WOODWARD, J. E. FORD, G. F. APLIN, L. A. D'ASARO, S. P. HUI, B. TSENG, R. LEIBENGUTH, D. KOSSIVES, D. DAHRINGER, L. M. F. CHIROVSKY and D. A. B. MILLER, *IEEE Photon. Technol. Lett.* **7**, 1288 (1995).

E. KUPHAL, "Low Resistance Ohmic Contacts to n- and p-InP," *Solid-State Electron.* **24**, 69 (1981).

J. LEE, E. S. KOTELES and M. O. VASSELL, "Luminescence linewidths of excitons in GaAs quantum wells below 150 K," *Phys. Rev. B* **33**, 5512 (1986).

ANTHONY L. LENTINE and DAVID A. B. MILLER, "Evolution of the SEED Technology: Bistable Logic Gates to Optoelectronic Smart Pixels," *IEEE J. Quant. Electron.* **29**, 655 (1993).

R. F. LEONARD and W. F. CORDES, III, "New High Speed Positive Resist for Wafer Steppers," *SPIE Optical Microlithography Technology for the Mid-1980's Seminar*, Santa Clara CA, March 31 and April 1 (1982).

K. R. LINGA, G. H. OLSEN, V. S. BAN, A. M. JOSHI and W. F. KOSONOCKY, "Dark Current Analysis and Characterization of $In_xGa_{1-x}As/InAs_yP_{1-y}$ Graded Photodiodes with $x > 0.53$ for Response to Longer Wavelengths (> 1.7 μm)," *J. Lightwave Technol.* **10**, 1050 (1992).

V. MALINA, U. SCHADE and K. VOGEL, "Technological aspects of the preparation of Au-Zn ohmic contacts to p-type InP," *Semicond. Sci. Technol.* **9**, 49 (1994).

H. MARCHAND, "Épitaxie en phase vapeur aux organometalliques et caractérisation de nanostructures auto-organisées à base de InAs/InP," M. A. Sc. Thesis, École Polytechnique de Montréal (1996).

J. Y. MARZIN, J. M. GÉRARD, P. VOISIN and J. A. BRUM, "Optical studies of strained III-V heterolayers," *Semiconductors and Semimetals* **32** (Academic, San Diego, 1990), 55.

J. W. MATTHEWS and A. E. BLAKESLEE, "Defects in epitaxial multilayers I: Misfit dislocations," *J. Cryst. Growth* **27**, 118 (1974); "Defects in epitaxial multilayers II: Preparation of almost perfect multilayers," *J. Cryst. Growth* **29**, 273 (1975).

X. B. MEI, W. G. BI, C. W. TU, L. J. CHOU and K. C. HSIEH, "Quantum-confined Stark effect at 1.5 μm wavelength in $InAs_{0.53}P_{0.47}/Ga_yIn_{1-y}P$ strain-balanced quantum wells," *J. Vac. Sci. Technol. B* **14**, 2327 (1996).

E. E. MENDEZ, G. BASTARD, L. L. CHANG, L. ESAKI, H. MORKOC and R. FISCHER, "Effect of an electric field on the luminescence of GaAs quantum wells," *Phys. Rev. B* **26**, 7101 (1982).

D. A. B. MILLER, D. S. CHEMLA, T. C. DAMEN, A. C. GOSSARD, W. WIEGMANN, T. H. WOOD and C. A. BURRUS, "Electric field dependence of optical absorption near the band gap of quantum-well structures," *Phys. Rev. B* **32**, 1043 (1985).

R. C. MILLER, A. C. GOSSARD, D. A. KLEINMAN and O. MUNTEANU, "Parabolic quamtum wells with the $GaAs\text{-}Al_xGa_{1-x}As$ system," *Phys. Rev. B* **29**, 3740 (1984).

O. MITOMI, I. KOTAKA, K. WAKITA, S. NOJIMA, K. KAWANO, Y. KAWAMURA and H. ASAI, "40-Ghz bandwidth InGaAs/InAlAs multiple quantum well optical intensity modulator," *Appl. Optics* **31**, 2030 (1992).

S. NOJIMA, Y. KAWAMURA, K. WAKITA and O. MIKAMI, "Electric field effects in excitonic absorption for high-quality InGaAs/InAlAs multiple-quantum-well structures," *J. Appl. Phys.* **64**, 2795 (1988).

P. H. L. Notten, "The Etching of InP in HCl Solutions: A Chemical Mechanism," *J. Electrochem. Soc.* **131**, 2641 (1984).

A. OUGAZZADEN and F. DEVAUX, "Strained InGaAsP/InGaAsP/InAsP multi-quantum well structure for polarization insensitive electroabsorption modulator with high power saturation," *Appl. Phys. Lett.* **69**, 4131 (1996).

M. PAXMAN, J. NELSON, B. BRAUN, J. CONNOLLY, K. W. J. BARNHAM, C. T. FOXON, and J. S. ROBERTS, "Modelling the spectral response of the quantum well solar cell," *J. Appl. Phys.* **74**, 614 (1993).

T. P. PEARSALL, "Strained-Layer Superlattices," *Semiconductors and Semimetals* **32** (Academic, San Diego, 1990), 1.

G. E. PIKUS and G. L. BIR, *Sov. Phys. Solid State* **1**, 136 (1959); 1502 (1960).

M.-E. PISTOL and D. GERSHONI, "Modeling of electroabsorption in semiconductor quantum structures wintin the eight-band **k•p** theory," *Phys. Rev. B* **50**, 11738 (1994).

F. H. POLLAK, "Effects of Homogeneous Strain on the Electronic and Vibrational Levels in Semiconductors," *Semiconductors and Semimetals* **32** (Academic, San Diego, 1990), 17.

R. P. SCHNEIDER, Jr. and B. W. WESSELS, "Photoluminescence Excitation Spectroscopy of $InAs_{0.67}P_{0.33}$/InP Strained Single Quantum Wells," *J. Electron. Mater.* **20**, 1117 (1991).

E. F. SCHUBERT, S. W. DOWNEY, C. PINZONE and A. B. EMERSON, "Evidence of very strong inter-epitaxial-layer diffusion in Zn-doped GaInPAs/InP structures," *Appl. Phys. A* **60**, 525 (1995).

B. L. SHARMA, "Ohmic Contacts to III-V Compound Semiconductors" in *Semiconductors and Semimetals* **15**, 1 (1981).

W. SHOCKLEY and H. J. QUEISSER, "Detailed Balance Limit of Efficiency of p-n Junction Solar Cells", *J. Appl. Phys.* **32**, 510 (1961).

JASPRIT SINGH, "A new method for solving the ground-state problem in arbitrary quantum wells: Application to electron-hole quasi-bound levels in quantum wells under high electric field," *Appl. Phys. Lett.* **48**, 434 (1986).

S. R. SLOANE, "Processing and Passivation Techniques for Fabrication of High-Speed InP/InGaAs/InP Mesa Photodetectors," *Hewlett Packard Journal*, 69 (October 1989).

G. STAREEV and H. KUNZEL, "Tunneling behavior of extremely low resistance nonalloyed Ti/Pt/Au contacts to n(p)-InGaAs and n-InAs/InGaAs," *J. Appl. Phys.* **74**, 7562 (1993).

J. N. STRANSKI and L. KRASTANOV, Ber. Akad. Wiss. Wein **146**, 797 (1938).

G. B. Stringfellow, *Organometallic vapor phase epitaxy: theory and practice* (Academic, Boston, 1989).

M. SUGAWARA, T. FUJII, S. YAMAZAKI and K. NAKAJIMA, "Theoretical and experimental study of the optical-absorption spectrum of exciton resonance in $In_{0.53}Ga_{0.47}As$/InP quantum wells," *Phys. Rev. B* **42**, 9587 (1990).

V. SWAMINATHAN, C. L. REYNOLDS, Jr., and M. GEVA, "Zn diffusion behavior in InGaAsP/InP capped buried heterostructures," *Appl. Phys. Lett.* **66**, 2685 (1995).

C. TEJEDOR and F. FLORES, "A simple approach to heterojunctions," *J. Phys. C* **11**, L19 (1978).

J. TERSOFF, "Theory of semiconductor heterojunctions: The role of quantum dipoles," *Phys. Rev. B* **30**, 4874 (1984).

J. TERSOFF and C. G. VAN DE WALLE, "Strain and the Interpretation of Band-Lineup Measurements," *Phys. Rev. Lett.* **59**, 946 (1987).

J. TERSOFF and F. K. LEGOUES, "Competing Relaxation Mechanisms in Strained Layers," *Phys. Rev. Lett.* **72**, 3570 (1994).

C. A. TRAN, "Croissance par épitaxie en phase vapeur aux organo-métalliques et caractérisation des hétérostructures contraintes à base de InP," Ph.D. Thesis, École Polytechnique de Montréal (1992).

C. A. TRAN, R.A. MASUT, P. COVA, J. L. BREBNER and R. LEONELLI, "Growth and characterization of InP on silicon by MOCVD," *J. Cryst. Growth* **121**, 365 (1992).

C. A. TRAN, J. T. GRAHAM, J. L. BREBNER and R. A. MASUT, "Interfaces of InAsP/InP multiple quantum wells grown by metalorganic vapor phase epitaxy," *J. Electron. Mater.* **23**, 1291 (1994).

W. TSENG, A. CHRISTOU, H. DAY, J. DAVEY and B. WILKINS, "Ohmic contacts to lightly doped n and p indium phosphide surfaces," *J. Vac. Sci. Technol.* **19**, 623 (1981).

T. UCHIDA, H. KURAKAKE, H. SODA and S. YAMAZAKI, "A 1.3 μm Strained Quantum Well Laser on a Graded InGaAs Buffer with a GaAs Substrate," *J. Electron. Mater.* **25**, 581 (1996).

Y. UCHIDA, H. KAKIBAYASHI and S. GOTO, "Electrical and structural properties of dislocations confined in a InGaAs/GaAs heterostructure," *J. Appl. Phys.* **74**, 6720 (1993).

C. G. VAN DE WALLE, "Band lineups and deformation potentials in the model-solid theory," *Phys. Rev. B* **39**, 1871 (1989).

O. WADA and O. UEDA, "Reliable Metallization for InP-Based Devices and OEIC's," MRS Symposium Proceedings **184**: *Degradation Mechanisms in III-V Compound Semiconductor Devices and Structures*, 209 (1990).

V. G. WEIZER and N. S. FATEMI, "A Unique, Device-Friendly Contact Systemfor Shallow Junction p/n Indium Phosphide Devices," *J. Electron. Mater.* **25**, 755 (1996).

T. H. WOOD, J. Z. PASTALAN, C. A. BURRUS, JR., B. C. JOHNSON, B. I. MILLER, J. L. DEMIGUEL, U. KOREN, and M. G. YOUNG, "Electric field screening by photogenerated holes in multiple quantum wells: A new mechanism for absorption saturation," *Appl. Phys. Lett.* **57**, 1081 (1990).

T. K. WOODWARD, T. SIZER II and T. H. CHIU, "$InAs_yP_{1-y}$ multiple quantum well optical modulators for solid-state laser," *Appl. Phys. Lett.* **58**, 1366 (1991).

T. K. WOODWARD, T. H. CHIU and T. SIZER II, "Multiple quantum well light modulators for the 1.06 μm range on InP substrates: $In_xGa_{1-x}As_yP_{1-y}$/InP, $InAs_yP_{1-y}$/InP, and coherently strained $InAs_yP_{1-y}/In_xGa_{1-x}P$," *Appl. Phys. Lett.* **60**, 2846 (1992).

E. YABLONOVITCH and E. O. KANE, "Band Structure Engineering of Semiconductor Lasers for Optical Communications," *J. Lightwave Technol.* **6**, 1292 (1988).

M. YAMAMOTO, N. YAMAMOTO and J. NAKANO, "MOVPE Growth of Strained InAsP/InGaAsP Quantum-Well Structures for Low-Threshold 1.3 μm Lasers," *IEEE J. Quant. Electron.* **30**, 554 (1994).

T. YAMANAKA, K. WAKITA and K. YOKOYAMA, "Field-induced broadening of optical absorption in InP-based quantum wells with strong and weak quantum confinement," *Appl. Phys. Lett.* **65**, 1540 (1994).

H. YAMAZAKI, Y. SAKATA, M. YAMAGUCHI, Y. INOMOTO and K. KOMATSU, "Low drive voltage (1.5 V p.p.) and high power DFB-LD/modulator integrated light sources using bandgap energy controlled selective MOVPE," *Electron. Lett.* **32**, 109 (1996).

E. T. YU, J. O. MCCALDIN and T. C. MCGILL, "Band Offsets in Semiconductor Heterojunctions" *Solid State Physics* **46** (Academic, Boston, 1992), 2.

APPENDIX - Band alignment strategy for efficient optical modulation in quantum-confined Stark effect devices

by R. Y.-F. Yip and R. A. Masut.

Groupe de recherche en physique et technologie des couches minces (GCM),
Département de génie physique, École Polytechnique de Montréal,
C.P. 6079, succ. "Centre-Ville", Montréal QC, Canada H3C 3A7

Submitted to the Journal of Applied Physics on March 11, 1997

Accepted for publication on May 15, 1997.

J. Appl. Phys. **82**, 1976 (1997)

ABSTRACT

Strategies designed to optimize the performance of the multi-quantum well stack in optical modulator devices based on the quantum-confined Stark effect can be derived from an observation that the effective mass of the active quantum well material is significantly smaller in the conduction band than that in the valence band. This suggests that significant improvements in the overall performance of the devices may be achieved by engineering the band alignment of quantum well and barrier to accommodate the difference in the effective masses.

COMMUNICATION

A characteristic common to all of the current, technologically significant III-V semiconductor thin film materials is an electronic band structure effective mass that is much smaller in the conduction band (CB) than in the valence band (VB). This can have important consequences for both the design of the materials and of the devices that employ these materials. For example, the turn-on threshold of semiconductor lasers is affected by this difference between the CB and VB effective mass density of states. The VB density, being larger, requires more intense pumping to reach the transparency condition required for lasing. In an ideal structure with minimal threshold, both CB and VB densities would be equal and small. Thus, the band structure engineering of quantum well semiconductor lasers is based on a strategy to reduce the VB density by choosing materials with an intrinsically small effective mass difference and by using biaxial strain to modify the valence band structure and further reduce this difference[1,2]. The optical modulators that are commonly integrated with low-threshold semiconductor lasers to form high-speed transmitter units for long haul fiber optic communications are yet another example where improvements in device performance may be obtained by engineering the band structure to accommodate and/or exploit this difference in the effective masses.

A multiple quantum well stack can be designed so that its band edge absorption may be significantly tuned by an electric field. The confinement potential of a quantum well permits weakly bound electron-hole pair systems, or excitons, associated to the discrete quantum well levels to persist at room temperature. These excitonic systems are formally similar to the hydrogen atom but with a much smaller binding energy for the fundamental level (~ 5-10 meV). They set up atomic-like absorption resonances with enhanced oscillator strength just below the main quantum well optical transitions. An electric field applied in the direction normal to the quantum well has two effects:

(1) It causes the discrete levels of the well at the CB and VB to shift with a resultant redshift of the optical transition energies;

(2) It polarizes the CB and VB quantum well eigenstates, broadens and quenches the absorption resonances.

However, the confinement potential of the quantum well can delay this quenching and allow the exciton resonance associated with the fundamental optical transition at the band edge to red-shift appreciably before field broadening becomes excessive. This allows the possibility of large field-dependent changes in the optical absorption at the band edge and the physical mechanism has been named the quantum-confined Stark effect[3]. The result makes it possible to operate simple, reverse-biased p-i-n photodiode

structures containing multi-quantum well stacks in the undoped core as efficient voltage-dependent optical modulators.

The quantum-confined Stark effect represents an interesting balance between field red-shifting and field polarization of the quantum well eigenstates. The band edge absorption is determined by how the applied field influences the fundamental quantum well energy levels at the CB and VB. Energy levels lying nearest to the bottom of the well follow more closely the contours of the field distorted well and demonstrate the largest red-shifts.[4] In all practical configurations, the larger hole effective mass results in a fundamental hole level that is much lower in the VB well than the corresponding electronic level is in the CB well. Hence, the VB component makes the dominant contribution to the red-shift of the total optical transition energy. Quenching due to de-localization of the electron and hole under field is characterized by field-assisted tunneling of the particles through the field-distorted barriers at the edges of the quantum well. This is determined by the penetrability of the electron and hole wavefunctions into the barrier, or equivalently by the magnitude of their respective wave vectors inside the barrier regions. The electronic wavefunction tends to leak out first because of the smaller effective mass.[5,6] Resistance to field quenching is therefore limited by the electronic component. Ideally, we could attempt to create a more balanced situation, as in the case with lasers, by finding ways to increase the CB effective mass so that it matches that of the VB.[7] However, methods for significantly increasing the effective

mass in the direction of the confinement potential while maintaining a constant band gap appear not to be available. A viable alternative for achieving more efficient optical modulation is to engineer the band alignment to reflect the disproportion in the effective masses.

As long as the CB wavefunction leaks out from the quantum well before the the VB wavefunction, the band alignment is sub-optimal because the hole barrier height will be higher than required. A better structure could conserve the energy of the fundamental optical transition while incorporating a lower hole barrier and higher electronic barrier. The lower hole barrier would give a lower fundamental level (smaller $E1$, Ref. 4) with larger red-shift per unit field while also allowing more efficient charge removal from the well to permit the use of greater incident optical intensities without saturation effects. Quench resistance is improved simultaneously with the higher electronic barrier. For a given total well depth, the quench resistance becomes optimal when the band alignment is such that the wavefunction leakage from the CB well is balanced equally with that from the VB well. We obtain estimates for the degree of asymmetry in the band alignment required for optimal quench resistance by posing conditions which equate the probability tunnel currents through the barrier sections in the CB to those in the VB as a function of electric field. At flat band (zero field), solving for the tunnel currents through rectangular barriers shows that this alignment occurs when $m_e V_e = m_h V_h$, giving $V_e/V_h \sim 9$ for conditions in a typical InGaAsP quantum well[8]. m_e, m_h, V_e and V_h are

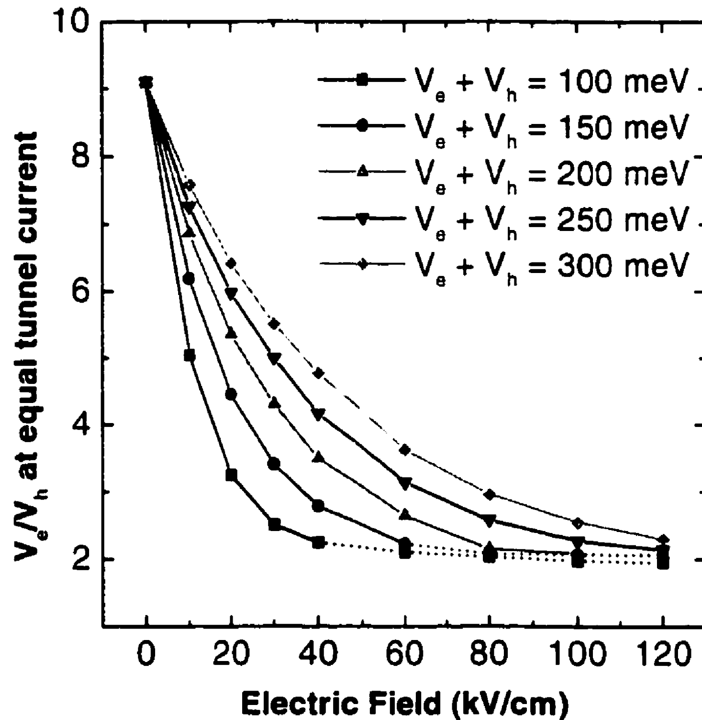

Figure A.1 The ratio of electronic (V_e) to hole (V_h) barrier heights giving equivalent field-assisted tunneling escape probabilities, as a function of electric field and total well depth ($V_e + V_h$). The data points have been obtained by writing the expressions for the tunneling probabilities at the conduction and valence bands and then solving iteratively for the barrier heights. The relationship plotted here corresponds to $m_e = 0.055m_0$, $m_h = 0.5m_0$ and 10 nm thick barriers.

respectively the CB and heavy hole VB effective masses and barrier heights. The situation under field corresponds to solving for the tunnel currents through field-distorted trapezoidal and triangular barriers [9]. The ratio of CB to VB barrier heights, V_e/V_h, giving this equivalent tunnel current condition is plotted in Figure A.1 as a function of the electric field and for a range of total quantum well depths. The V_e/V_h

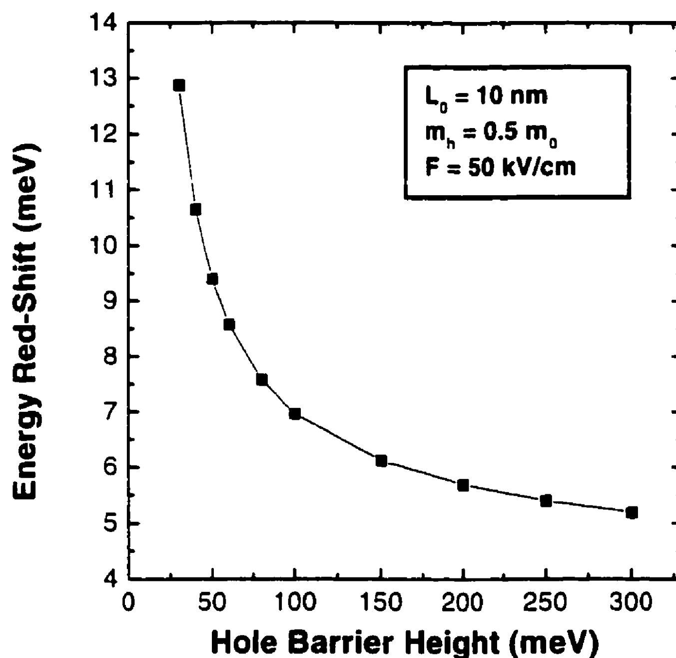

Figure A.2 The influence of the finite barrier height on the red-shift of the fundamental hole level in a single 10 nm wide quantum well at 50 kV/cm. The computation has been performed using the variational description of the quantum-confined Stark effect developed by Bastard *et al.* (see Ref. 10).

ratio at the balance condition decreases with applied field since the lower VB barrier is always first to distort into a triangle while the electronic barrier is still a trapezoid. For a triangular barrier, both the barrier width and average barrier height decrease with the field resulting in a rapid rise in the transmission probability. In the region above each curve, the field broadening is VB limited so that losses in quench resistance may be balanced by improvements in red-shift per unit field. In the region below, however, it is CB limited so that both quench resistance and red-shifting performances are

compromised. Therefore, optimal band alignments can occur only on a curve or in the region above it.

This optimal configuration balancing red-shift versus quench resistance must be determined for each specific application. For example, optical modulators for fiber optic telecommunications are required to operate at very high frequencies (≥ 10 GHz). This places severe restrictions on the available drive voltage and consequently on the drive field. The redshift per unit drive field can be enhanced by appealing to low VB barrier heights. As operation frequencies increase, the optimal balance for this application may be expected to favor enhancements to the red-shift afforded by low VB barriers. In Figure A.2, an analysis based on the variational description of the red-shift in a finite well developed by Bastard *et al.*[10] demonstrates that the red-shift per unit field begins to increase sharply for VB barriers lower than ~ 60 meV.[11] After having chosen the VB barrier to satisfy the drive field criterion, Figure A.1 then shows that the electronic barrier must be at least ~ 3 times higher than the hole barrier to ensure that premature de-localization of the electronic wavefunction with increasing field does not dominate the behavior. Otherwise, it will not be possible to extract the full potential of using the low VB barrier. It is worth noting that nearly all of the multi-quantum well stacks currently designed for use as high data rate optical modulators incorporate hole barriers that are far too high and/or have band alignments with V_e/V_h ~ 0.6 - 2.0. The InGaAs/InAlAs system of lattice-matched alloys on InP is reported to have a relatively favorable band

alignment (V_e/V_h ~ 2.5) but the very high (~ 200 meV) hole barrier requires high drive fields to induce significant red-shifts. Systems of InGaAs(P)/InGaAsP alloys that are nearly lattice-matched to InP can have lower hole barriers but the electronic barriers are too low, giving only V_e/V_h ~ 1. Such structures are clearly sub-optimal. The available data on band alignments suggests that the strained InAsP/InGaAsP and InGaAs/InAlGaAs systems on InP are more promising candidates for investigation. In conclusion, by making a judicious choice of the material compositions to give a favorable starting point and then fine-tuning the band alignment, it should be possible to achieve more efficient devices capable of operating at higher frequencies and with greater input optical intensities.

This work was supported by the Natural Sciences and Engineering Research Council (NSERC) of Canada and les Fonds pour la Formation de chercheurs et l'aide à la recherche (FCAR) du Québec. R. Y.-F. Yip wishes to thank Pat Desjardins for his steady encouragement.

---

[1] A.R. Adams, Electron. Lett. **22**, 249 (1986).

[2] E. Yablonovitch and E.O. Kane, J. Lightwave Technol. **6**, 1292 (1988).

[3] D.A.B. Miller, D.S. Chemla, T.C. Damen, A.C. Gossard, W. Wiegmann, T.H. Wood, and C.A. Burrus, Phys. Rev. B **32**, 1043 (1985).

[4] R. Y.-F. Yip, A. Aït-Ouali, A. Bensaada, P. Desjardins, M. Beaudoin, L. Isnard, J.L. Brebner, J.F. Currie and R.A. Masut, J. Appl. Phys. **81**, 1905 (1997): $\Delta E1 \sim 1/E1$ where

$\Delta E1$ is the field-induced red-shift and $E1$ is the energy of the fundamental level measured with respect to the bottom of the quantum well.

[5] W.L. Bloss, J. Appl. Phys. **65**, 4789 (1989).

[6] T. Yamanaka, K, Wakita, and K. Yokoyama, Appl. Phys. Lett. **65**, 1540 (1994).

[7] Unlike in the case for lasers, heavier effective masses are advantageous here.

[8] The electronic ($m_e = 0.055m_0$) and heavy hole ($m_h = 0.5m_0$) effective masses have been chosen to be representative of an InGaAsP alloy with a band gap energy in the 0.80 - 0.95 eV range and a lattice parameter near that of InP. The energy band curvature near zone center in the direction of the confinement potential (the growth axis) depends principally upon the band gap energy. Biaxial strain in the plane may significantly modify the band curvature normal to the growth axis but the effective masses in the direction of the confinement potential are expected to be fairly constant (± 10%) over a range of alloy compositions, provided that the band gap energy remains in the desired range.

[9] R. Y.-F. Yip, P. Desjardins, L. Isnard, A. Aït-Ouali, H. Marchand, J.L. Brebner, J.F. Currie and R.A. Masut, (in preparation). The expressions for these currents may be found in K. H. Grundlach, Solid-State Electron. **9**, 949 (1966).

[10] G. Bastard, E.E. Mendez, L.L. Chang, and L. Esaki, Phys. Rev. B **28**, 3241 (1983).

[11] The enhancement of the red-shift per unit field with decreasing barrier height is due to two mechanisms. (1) Lowering the barrier height lowers the zero-point energy of the quantum well eigenstate and enhances its sensitivity to the energy gradient. (2) The wavefunction penetration into the barrier under field is greater for lower barriers which decreases the degree of spatial localization of the eigenstate in the field distorted corner of the quantum well. By virtue of the uncertainty principle, such a state necessarily attains a lower zero-point energy than its counterpart in a quantum well with a higher barrier.